U.S. Department of Energy
Office of FreedomCAR and Vehicle Technologies
1000 Independence Avenue S.W.
Washington, DC 20585-0121

FY 2006

Progress Report for Automotive Propulsion Materials Program

Energy Efficiency and Renewable Energy
Office of FreedomCAR and Vehicle Technologies

Edward Wall **Program Manager**

January 2007

CONTENTS

ACRONYMS, ABBREVIATIONS, AND INITIALISMS

ANL	Argonne National Laboratory
ANL–ES	ANL–Energy Systems
APS	Advanced Photon Source
APM	Automotive Propulsion Materials
ASTM	American Society for Testing and Materials
CIDI	compression-ignition direct-injection
DI	deionized water
DOE	U.S. Department of Energy
DPF	diesel particulate filter
EDM	electrodischarge machining
EDX	energy-dispersive X-ray spectroscopy
EE	Electrical and Electronics
EGO	exhaust gas oxygen
EGR	exhaust gas recirculation
EN	electroless nickel
EPA	Environmental Protection Agency
EPA–NVFEL	EPA National Vehicle and Fuel Emissions Laboratory
ERDA	elastic recoil detection analysis
EXAFS	X-ray absorption fine structure
FCVT	FreedomCAR and Vehicle Technologies
FEA	finite element analysis
FT	Fischer-Tropsch
FY	fiscal year
GM	General Motors
H	hardness
H^+	hydrogen ion
H_2	hydrogen gas
HC	hydrocarbon
HCCI	homogeneous charge compression-ignition
I-V	current-voltage
ICS	Industrial Ceramic Solutions
ID	internal diameter
ITO	tin-doped indium oxide
LANL	Los Alamos National Laboratory
L/D	length-to-diameter
LLNL	Lawrence Livermore National Laboratory
MLCC	multilayer ceramic capacitor

NdFeB	neodymium-iron-boron
Nd	neodymium
NDE	nondestructive examination
Ni	nickel
NIST	National Institute for Standards and Testing
NIU	Northern Illinois University
nm	nanometer, 10^{-9} meters
NO	nitrogen oxide, nitric oxide
NO_x	oxides of nitrogen
NVFEL	National Vehicle and Fuel Emissions Laboratory
OEM	original equipment manufacturer
OFCVT	Office of FreedomCAR and Vehicle Technologies
ORNL	Oak Ridge National Laboratory
Pd	palladium
PLZT	lead lanthanum zirconium titanate
PM	permanent magnet or particulate matter
PNNL	Pacific Northwest National Laboratory
PPS	polyphenylene sulfonate
Pt	platinum
PZT	lead zirconium titanate
R&D	research and development
RBS	Rutherford backscattering
S	sulfur
Sr	strontium
SAE	Society of Automotive Engineers
SEM	scanning electron microscope/scanning electron microscopy
SHNC	superhard nanocomposite
SNL	Sandia National Laboratories
T	Tesla
WC	tungsten carbide
YSZ	yttria-stabilized zirconium

1. INTRODUCTION

Automotive Propulsion Materials R&D: Enabling Technologies to Meet FreedomCAR Program Goals

The Department of Energy's (DOE's) Office of FreedomCAR and Vehicle Technologies (OFCVT) is pleased to introduce the FY 2006 *Annual Progress Report for the Automotive Propulsion Materials Research and Development Program*. Together with DOE national laboratories and in partnership with private industry and universities across the United States, the program continues to engage in research and development (R&D) that provides enabling materials technology for fuel-efficient and environmentally friendly light-duty vehicles.

This introduction summarizes the objectives, progress, and highlights of the program in FY 2006. It also describes the technical barriers remaining and the future direction of the program. The FY 2006 annual progress reports on *Combustion and Emission Control for Advanced CIDI Engines* and *Power Electronics* provide additional information on OFCVT's R&D activities that support the development of propulsion materials technology.

In August of 2005, President Bush signed the Energy Policy Act of 2005. This comprehensive energy policy specifically addresses the development of energy-efficient vehicle technologies, including hybrid systems, advanced emission control technologies, fuel cells, and hydrogen-based systems. The Energy Policy Act is a strong indicator of the continuing federal support for advanced automotive technologies and the materials work that supports them.

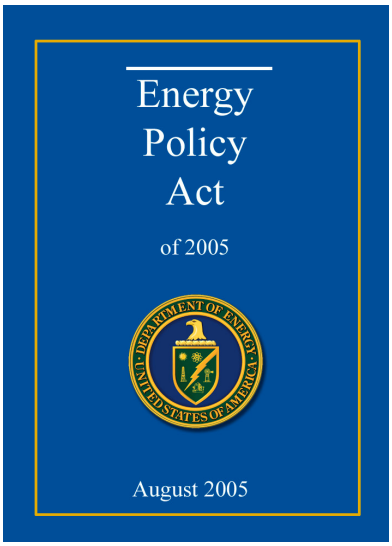

The Automotive Propulsion Materials (APM) R&D Program has supported the FreedomCAR Program since its inception. FreedomCAR is not an automobile or prototype but rather a new approach to developing the technologies for vehicles of the future. In research areas where industry views the risks as too high and uncertain, the FreedomCAR Program conducts long-term research, development, and demonstration activities that bring the technology to a stage of maturity such that industry can undertake the final commercialization stages.

The APM Program is a partner with the OFCVT programs for Power Electronics and Electric Machines and for Combustion and Emissions Control for Advanced CIDI Engines. Projects within the APM Program address materials concerns that directly impact the critical technical barriers in each of these programs—barriers such as thermal management, emissions reduction, and reduced manufacturing costs. The program engages only the barriers that involve fundamental, high-risk materials issues.

Enabling Technologies

The APM Program focuses on enabling materials technologies that are critical in removing barriers to the power electronics and compression-ignition, direct-injection (CIDI) engine and emissions control research programs. The program supports these two core technology areas by providing materials expertise, testing capabilities, and technical solutions for materials problems. The component development, materials processing, and characterization that the program provides are enablers of the successful development of efficient electric drive systems and emissions-compliant CIDI engines.

Thermal management is a crosscutting engineering issue that affects both the power electronics and CIDI programs. The components necessary for high-fuel-economy, low-emission hybrid electric and fuel cell vehicles require that power electronics be smaller and lighter and operate at higher temperatures than those for conventional vehicles. These requirements are being addressed by developing electronic materials (i.e., materials for low-cost dc bus capacitors) that operate at higher temperatures and by improving the capability to dissipate heat generated in electronic devices. The APM Program has been addressing electric drive system heat dissipation issues through the development of advanced carbon foam technology.

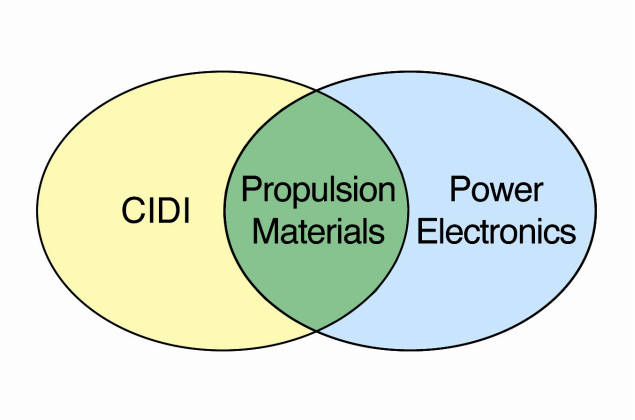

The Propulsion Materials Program focuses on two applications.

Current CIDI engines must strike a delicate balance between high efficiency and low tailpipe emissions. CIDI engine and aftertreatment system development will greatly benefit from the Program's efforts to develop improved engine components and subsystems. The APM Program featured a project to develop technology to produce very small (~50 micron) orifices for fuel injectors used in high-pressure common rail systems. The smaller orifices can enable better control of fuel atomization that will increase efficiency and reduce emissions. A study was initiated in FY 2004 at Pacific Northwest National Laboratory (PNNL) to determine the frictional behavior of metals—like those used in fuel injectors—in the hydrogen environment of a hydrogen internal combustion engine or fuel cell. The friction and wear characteristics of metallic materials depend largely on surface oxide films. However, a hydrogen environment is chemically reducing, so the loss of the surface oxide by wear will result in bare surface contact and an increase in friction and wear. The Program also completed a project to reduce emissions through the development of advanced particulate filters.

A new project was initiated at Oak Ridge National Laboratory (ORNL) in FY 2005 to identify materials requirements for the operating conditions in homogeneous charge compression-ignition (HCCI) engines and demonstrate the feasibility of the "materials by design" approach to developing advanced materials for the most critical engine components. Collaborations have already been established with two companies to work together on materials needs. Interaction with industrial partners throughout the project is expected to result in the rapid transfer of materials improvements to industry.

Collaboration and Cooperation

As with other programs under FreedomCAR, collaboration and cooperation across organizations is a critical part of the APM Program. Throughout the FreedomCAR Program, scientists at the national laboratories are collaborating with manufacturers to identify and refine the materials characteristics necessary for meeting system performance requirements. Researchers at Lawrence Livermore National Laboratory (LLNL) are working with Ford Motor Company and ORNL to develop low-cost, rapid-response nitrogen oxides (NO_x) sensors that can be used in feedback control loops to monitor and minimize NO_x emissions from diesel engines. There is also cooperation among national laboratories to take advantage of the expertise of each facility. ORNL and Sandia National Laboratories (SNL), for example, are collaborating in the development of high-temperature polymer dielectric films. ORNL is characterizing ~5-micron-thick polymer films that are being developed by SNL, which is funded by the Power Electronics Program to develop smaller, higher-temperature dc bus capacitors that will enable significant reductions in the size, weight, and cost of power electronics used in hybrid vehicles. SNL is using the information provided by ORNL to optimize the properties of the films in order to minimize manufacturing defects during capacitor winding. In another project,

ORNL is conducting friction and wear testing of candidate needle/nozzle pairs developed by researchers at PNNL for use in hydrogen internal combustion engines and fuel cells.

In addition to participation by national laboratories and large industries, the FY 2006 APM Program included important R&D conducted by a small business. Industrial Ceramic Solutions, LLC (ICS), located in Oak Ridge, Tennessee, developed a ceramic filter to reduce particulate emissions from diesel engines. As in the collaborative efforts of national laboratories with industry, researchers at ICS are working closely with representatives from DaimlerChrysler, Ford, General Motors, and ORNL to develop a filter that will meet the emissions targets of the program. The final report, *Diesel Particulate Filter Development*, is included as Appendix B.

Contractor-industry collaboration

Technology	Industrial partner
Capacitors	TPL, Inc.
	Brady Corporation
	Steiner Film, Inc.
	AVX, Inc.
	Custom Electronics
Magnets	IAP, Inc.
	Magnaquench, UG, Inc.
	Ability Engineering Technology
	Electron Energy Corporation
	Bronson and Bratton, Inc.
Carbon foam heat sinks	Ford Scientific Research Laboratory
	DaimlerChysler
	General Motors Corporation
	Delphi
	Visteon
Fuel injectors	Siemens, USA
	Siemens, AG
	Navistar/International Harvester
	Imagineering Finishing Technologies
NO_x sensors	Ford
	Cummins Engine Company
	Detroit Diesel
	Honeywell
	DuPont
Particulate traps	Ford-Jaguar
	GE Locomotive
	Ahlstrom Paper
	Tennaco Automotive
	Arvin Meritor

Accomplishments

FY 2006 featured significant advancements in the two newest materials program areas. The following section highlights some of these noteworthy accomplishments.

Smaller Orifices Could Lower Emissions

In order to comply with stringent Environmental Protection Agency (EPA) regulations, diesel engines are being redesigned to increase efficiency and reduce emissions and in-cylinder soot production. One of the design changes is an increase in the pressure at which fuel is injected. The high pressure makes it necessary to reduce the diameter of fuel injectors to improve fuel atomization, which will increase efficiency and reduce emissions. Researchers at Argonne National Laboratory (ANL) have successfully developed a process to reduce the diameter of fuel injectors from 200 to 50 μm through an electroless nickel plating process that deposits nickel/phosphorus or nickel/boron alloys on the internal diameters of injector orifices (see figure). This process is necessary to effectively produce small, uniform orifice diameters from inlet to outlet (see graph) because conventional fabrication processes result in unacceptable error rates. Collaborations have been established with commercial plating companies and fuel injector manufacturers to produce and test fuel injectors with the reduced orifice diameters.

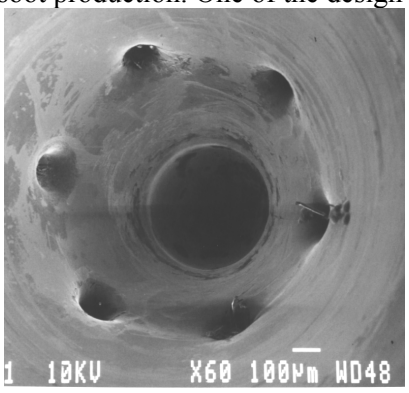

SEM image of nozzle interior (coated).

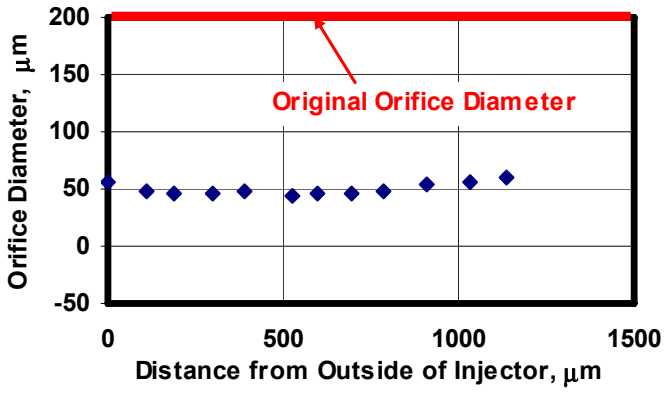

Diameter of coated orifice as a function of position.

Low-Cost, High-Energy-Product Permanent Magnets

Sintered NdFeB permanent magnets are used in the traction motors of hybrid electric vehicles because of their superior magnetic properties (energy product) compared with other permanent magnets. Higher-strength magnets are desired because they would enable manufacturers to reduce the size, weight, and volume of the traction motor and thus increase the fuel efficiency of the vehicle. A project at ANL to develop higher-strength NdFeB magnets was completed in FY 2006. The research used a high-strength superconducting magnet to improve the magnetic grain alignment of magnet powders prior to pressing and sintering (see photo). A significant increase of 12–15% in energy product (see graph) was achieved, and an economic assessment performed by a consulting firm concluded that the magnets would be no more expensive than conventional magnets. Over the past 5–6 years, nearly all of the domestic magnet manufacturers have moved overseas. It is hoped that the process developed at ANL will entice manufacturers to move back to the United States. An abbreviated version of the final report for the project, including a section on the economic analysis of this report.

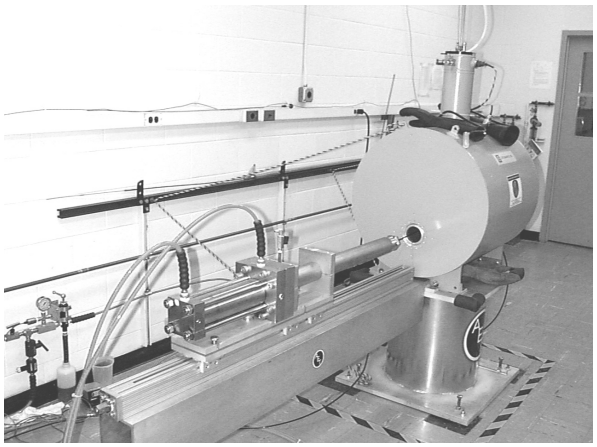

The liquid-helium-cooled superconducting magnet used to make compacts under a strong alignment field at ANL.

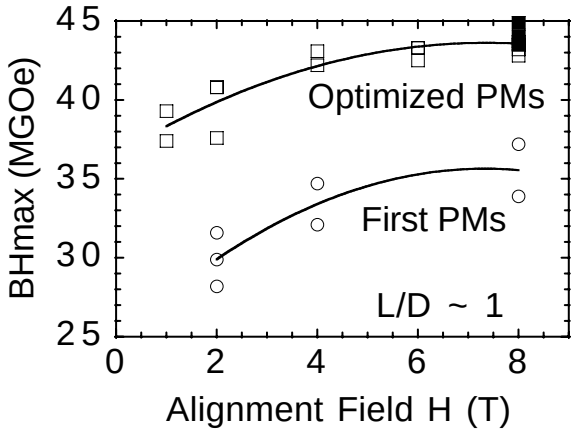

Energy product was increased 12% by tripling the alignment field. An alignment field of 2 T is used in the conventional process.

Future Direction

The APM Program will continue to work closely with FreedomCAR partners and industry to increase understanding of the requirements related to propulsion materials. Building upon recent advances in materials technologies, many of this year's projects will be moved out of the laboratory and over to industry for testing. For example, researchers at ORNL will work with identified strategic manufacturing partners (Koppers and ThermalCentric) and the automotive industry to commercialize compact, highly efficient heat exchanger/heat sink designs for power electronics that are enabled by the heat transfer properties of high-conductivity graphite foam. LLNL, Ford, and ORNL have formed a partnership to develop and prototype a NO_x sensor and control system to control the operation of NO_x traps and engine emissions. Other projects will continue to refine manufacturing requirements and necessary characteristics to meet the challenges of the FreedomCAR program.

As advanced automotive technology developments uncover new challenges, the APM Program will continue to provide breakthrough technology solutions through collaboration with industry, FreedomCAR partners, national laboratories, and small businesses.

Project Abstracts

The remainder of this report communicates the progress achieved during FY 2006 under the APM Program. It consists of seven abstracts of national laboratory projects—three that address power electronics and four that address combustion and emission technologies. The abstracts provide an overview of the critical work being conducted to improve these systems, reduce overall cost, and maintain component performance. In addition, they provide insight into the challenges and opportunities associated with advanced materials for high-efficiency automobiles. Also included as Appendixes A and B are final reports from two projects that have been completed (Diesel Particulate Filter Development and Low-Cost, High-Energy Product Permanent Magnets.)

Jerry Gibbs

Team Leader, Materials Technologies
Office of FreedomCAR and Vehicle Technologies
Energy Efficiency and Renewable Energy

2. POWER ELECTRONICS

A. Low-Cost, High-Energy-Product Permanent Magnets

Y. S. Cha and John R. Hull
Energy Technology Division, Bldg. 335
Argonne National Laboratory, Argonne, IL 60439
(630) 252-5899; fax: (630) 252-5568; e-mail: yscha@anl.gov

DOE Materials Technologies Team Leader: Jerry Gibbs
(202) 586-1182; fax: (202) 586-1600; e-mail: jerry.gibbs@ee.doe.gov
ORNL Technical Advisor: David Stinton
(865) 574-4556; fax: (865) 241-0411; e-mail: stintondp@ornl.gov

Contractor: Argonne National Laboratory, Argonne, Illinois
Prime Contract No.: W-31-109-Eng-38

Objective

- Develop a low-cost process to fabricate anisotropic NdFeB permanent magnets (PMs) with an increase of up to 25% in energy product to enable significant size and weight reductions in traction motors for hybrid vehicles.

Approach

- Use high fields of superconducting solenoids to improve magnetic grain alignment while pressing compacts for sintering, thus producing higher-performance magnets.
- Develop an automated press system, including the superconducting magnet, for the fabrication of NdFeB PMs.
- Conduct an economic analysis of the automated superconducting PM fabrication system and compare it with the conventional system.

Accomplishments

- Revised the report on the economic analysis of the PM project and issued the report in November 2005.
- Prepared the final report on the PM project.

Future Direction

- This is the last year that this project will be funded.

Introduction

The strength of sintered NdFeB magnets greatly depends on the method by which the compact is magnetically aligned and pressed. Large blocks can be made by cold-isostatic pressing that are within 5% of their theoretical maximum; but these must be sliced, diced, and ground to final shape, making the magnets very expensive. Magnets that are axial-die-pressed and sintered to near-final shape are the least expensive to make, but they have magnetic properties farthest from their theoretical maximums. The current industry goal is to fabricate higher-energy-product magnets by near-net-shape processing to avoid expensive machining operations. The major

objectives of this project are to increase the energy product of the sintered PMs by 10 to 15% (to within ~10% of the theoretical maximum) and to develop low-cost methods of production for high-energy-product, near-final-shape PMs. The higher-performance magnets will replace ones made by traditional powder metallurgy processing and will enable significant size and weight reductions in traction motors for hybrid vehicles.

Approach

Our approach is to align the NdFeB powder in a superconducting magnet, which can generate magnetic fields much higher than those generated by the electromagnets presently used in industry. Alignment of the powder in these higher magnetic fields improves the properties of the PMs. To develop a low-cost mass-production method for high-energy-product PMs, we plan to design, fabricate, and demonstrate a semi-automated axial-die-press system for making near-final-shape NdFeB PMs.

Previously, a 9-T superconducting solenoid was procured and made operational. Production-grade magnet powder was obtained from Magnequench UG. The 3- to 5-micron single-crystal grains of powder were aligned and compacted at Argonne National Laboratory (ANL). Then the anisotropic compacts, with their grains mechanically locked in place, were returned to Magnequench UG for sintering, annealing, machining, and measuring of engineering magnetic properties.

Previously, we demonstrated that significant improvement of energy product (10–15%) can be achieved by using higher alignment fields (>2 T). It was also demonstrated that near-net-shape PMs (with a diameter-to-length ratio of as low as 0.25) can be fabricated using the present technology. Industry considers an improvement in energy product of as little as 3–5% over current PMs to be significant. The progress achieved so far is based on a batch process at ANL. In FY 2005, we redesigned the die and punch set to alleviate (1) the trapped air problem during powder compaction and (2) the compact cracking problem during compact ejection from the die. The success of these two tasks will allow the PM to be fabricated at much faster rate than with the batch process. It appears that the project has achieved its initial objectives, and it was decided to bring the project to a successful conclusion by preparing an all-inclusive final report.

Results

In FY 2004, we contracted with Data Decisions to conduct an economic study of the superconducting PM manufacturing system. A preliminary report was received in FY 2005. Review comments were received from DOE, ANL, and Oak Ridge National Laboratory. These comments were transmitted to Data Decisions. After several iterations, a final report on the economic analysis of the superconducting PM manufacturing system was issued in November 2005.1 Part of the report of the economic study was incorporated into the final report of the PM project.

The major task of FY 2006 is to prepare a final report for the low-cost, high-energy-product PM project. The report summarizes all the activities and tasks carried out from the beginning to the end of this project, including background information and the economic analysis. The table of contents of the report is listed below.

I. Introduction
II. Superconducting magnet
III. Die and punch set
IV. Hydraulic press system and operation
V. NdFeB powder and the glove box
VI. Fill-density study
VII. Effect of alignment field on the magnetic properties of PM
VIII. Electromagnetic code study
IX. Magnet characterization using X-ray diffraction at ORNL
X. Some technical issues
XI. Modified die and punch sets
XII. Economic study
XIII. Summary and conclusions
Acknowledgements
References
Appendix

The final report was completed in April of 2006 and issued shortly afterward.[2] An abbreviated version of the final report that includes a section on the economic analysis of the process can be found as Appendix A of this report. Copies of the final report

and the economic analysis can be obtained by contacting David Stinton at stintondp@ornl.gov.

Conclusions

The conclusions reached in the final report are summarized below.

It was demonstrated that significant improvement of the energy product of the order of 12–15% can be achieved by using the stronger alignment field produced by the superconducting magnet. Near-final-shape PMs with length-to-diameter (L/D) ratios of as low as 0.25 were made successfully. The largest improvements in energy product were achieved with the smallest L/D ratio because the self-field (de-magnetization) effect due to the geometry of the thin cylindrical disk was largely overcome by the strong alignment fields.

Economic analysis indicates that (1) the capital and operating costs of the superconducting system are not significantly different from those of a conventional electromagnet system, and (2) the price per piece of the superconducting system appears to be 10–15% below that of the conventional system for near-final-shape magnets because the former does not require extensive grinding and/or slicing after sintering.

Overall, the superconducting manufacturing system would

1. Produce NdFeB magnets with higher energy, +15%, at a lower cost, −10% to −15%, than present technology. Even if there were no cost savings, the increase in energy product would make the technique worthwhile.
2. Present the automotive industry with higher-performance, reduced-weight magnets that
   - reduce vehicle weight
   - increase vehicle mileage
   - can be used in other applications besides traction motors
   - can be achieved without increasing the current cost of the magnets
3. Provide similar benefits to other U.S. industries
4. Encourage the use of this technique by a U.S. producer

References

1. R. E. Wolf, *An Economic Study of the Manufacture of High Energy Permanent Magnets for Traction Motors in Hybrid Electric Vehicles,* submitted by Data Decisions to Argonne National Laboratory, November, 2005.
2. Y. S. Cha, T. M. Mulcahy, and J. R. Hull, *Low-Cost, High-Energy-Product Permanent Magnets*, final report, Thermal and Electromechanics Section, Energy Technology Division, Argonne National Laboratory, June 2006.

Publications/Presentations

R. E. Wolf, *An Economic Study of the Manufacture of High Energy Permanent Magnets for Traction Motors in Hybrid Electric Vehicles*, submitted by Data Decisions to Argonne National Laboratory, November 2005.

Y. S. Cha, T. M. Mulcahy, and J. R. Hull, *Low-Cost, High-Energy-Product Permanent Magnets*, final report, Thermal and Electromechanics Section, Energy Technology Division, Argonne National Laboratory, June 2006.

B. Graphite Foam for Cooling Power Electronics

Nidia C. Gallego
Oak Ridge National Laboratory
P.O. Box 2008, MS 6087, Bldg. 4508
Oak Ridge, TN 37831-6087
(865) 241-9459; fax: (865) 576-8424; e-mail: gallegonc@ornl.gov

Albert Shih, Steve White
S. M. Wu Manufacturing Research Center
University of Michigan

Anthony G. Straatman
Department of Mechanical and Materials Engineering
University of Western Ontario
London, Canada

Brian E. Thompson and Qijun Yu
Foam Application Technologies, Inc.
Mayaguez, Puerto Rico

DOE Materials Technologies Team Leader: Jerry Gibbs
(202) 586-1182; fax: (202) 586-1600; e-mail: jerry.gibbs@ee.doe.gov
ORNL Technical Advisor: David P. Stinton
(865) 574-4556; fax: (865) 241-0411; e-mail: stintondp@ornl.gov

---

Contractor: Oak Ridge National Laboratory, Oak Ridge, Tennessee
Prime Contract No.: DE-AC05-00OR22725

Objective

- Collaborate with an automotive partner to develop an optimized heat exchanger/heat sink design that best utilizes the heat transfer properties of graphite foam to significantly reduce the size and weight of the thermal management system.

Approach

- Study fundamental mechanisms of heat transfer in graphite foam and develop an engineering model that can be used to design and/or evaluate optimized thermal management systems using graphite foam.
- Study the boiling heat transfer on the surface of graphite foam and evaluate the performance of graphite foams as a heat spreader in such a system.
- Document the heat transfer coefficients and pressure drops of graphite foams having different structures or morphologies.

Accomplishments

- Produced graphite foams with varying structure/morphology and demonstrated that more open structures produced improved heat transfer.

- In collaboration with General Motors (GM) and the University of Michigan, demonstrated an increase in boiling heat transfer from a foam surface by the addition of nanoparticles.
- Determined that boiling heat transfer was the best mechanism to capitalize on the heat transfer properties of graphite foam.

Future Direction

- Collaborate with ThermalCentric and Koppers to design and build a prototype heat exchanger for evaluation by a partner from the automotive industry.
- Evaluate the performance of graphite foam as a heat spreader.

Introduction

Porous graphite foam developed at Oak Ridge National Laboratory (ORNL)[1,2] is being investigated as a material to improve both single-phase and multiphase heat transfer. Graphite foam has a high effective conductivity (40–160 W/m K) because of the high material conductivity of the graphite material (800–1900 W/m K). In comparison, similar porous aluminum foams have effective conductivities of 2–26 W/m K, resulting from material conductivities of only 140–237 W/m K (for various aluminum alloys).[3] The high effective conductivity of the porous graphite foam combined with the open, interconnected pore structure facilitates high internal heat transfer and the potential for high convective heat transfer enhancement.

Work continued in FY 2006 to characterize the hydrodynamic and thermodynamic performance of graphite foam and how it impacts the development of modern heat exchangers and electronic heat sinks. Experiments were conducted in conjunction with modeling in order to explore the use of porous graphite foam for the removal of heat from power electronics.

A modified thermosyphon test rig was designed and built for the evaluation of the performance of graphite foam in these types of cooling systems. Additionally, the effect of using nanofluids on the performance of the graphite foam-based thermosyphon is being studied.

Experimental and Modeling Study

Characterization of the hydrodynamic and thermodynamic performance of a variety of ORNL-produced graphite foams, a commercial POCO™ foam, and a couple of experimental Koppers foams was completed. The experiments were conducted on a small-scale test rig to measure the heat transfer and pressure drop across blocks of porous graphite foam. The test setup shown in Figure 1 consists of a channel with a fluid inlet and outlet; a heating element; and instrumentation to measure the flow rate, the heat input, and the fluid pressure drop across the foam block (from position 1 to 2). Graphite foam samples of different porosities and pore diameters were subjected to a range of flow rates and power densities to quantify variations in pressure drop and thermal effectiveness in the foam structure (characterized by porosity, ε, and void diameter, Dp). The flow Reynolds number (defined as $Re=\rho VpbDep/\mu$, where ρ is the density of the fluid, *Vpb* is the channel bulk velocity, *Dep* is the equivalent solid particle diameter of the foam and μ is the dynamic viscosity of the fluid) was also determined.

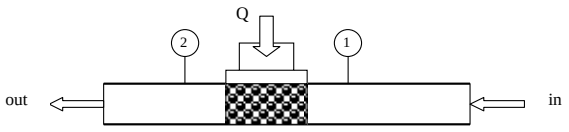

Figure 1. Schematic of experimental setup showing the position of the graphite foam, the fluid inlet (in) and outlet (out), and the heat input (Q).

The goal was to study the heat transfer and pressure drop obtained when passing fluid through the internal structure of the foams. Expressions describing the pressure drop and pore-level heat transfer could then be developed for use in the design of electronic heat sinks.

Table 1 lists the geometric properties and effective thermal conductivities of representative graphite foam specimens. Results were also compared with similar results for aluminum foams.

Table 1. Summary of properties for a selected set of graphite foam specimens tested

Specimen	Porosity (%)	Average pore diameter (μm)	k_{eff} (W/m K)
ORNL-A	88	400	61
ORNL-B	86	350	72
POCO™	82	500	120
Koppers-A	78	500	46
Koppers-B	92	850	NA

* As obtained from the unit-cube geometry model.

In the foams studied, the sizes of the cell windows connecting the pores varied significantly. The cell windows provide the interconnectivity between the voids and thus afford access to the internal surface area of the foam. To facilitate heat transfer, it is best to have small cell windows to maximize the internal surface area available for convection; however, small cell windows will lead to much higher pressure drops due to the hydrodynamic loss associated with rapid contraction/expansion through the cell windows. Thus, the most *open* foam will undoubtedly yield the lowest pressure, but it may not necessarily yield the highest convective heat transfer because of its lower internal surface area.

Results for the pressure drop as a function of the average channel velocity, *v*, are shown in Figure 2 for several foams of varying pore structures. The permeability and form drag coefficients established from the experiments are listed in Table 2. It is clear from Figure 2 and Table 2 that the permeability and related pressure drop differ significantly for the specimens tested, with ORNL-B having the highest fluid pressure drop and Koppers-B having the lowest. As suggested previously, the pressure drop is strongly affected by the pore diameter and, perhaps more important, the sizes of the cell windows connecting the pores. It is difficult, however, to assess the impact of pore diameter and cell window size independently based on current data. Figure 3 shows SEM images of three representative specimens.

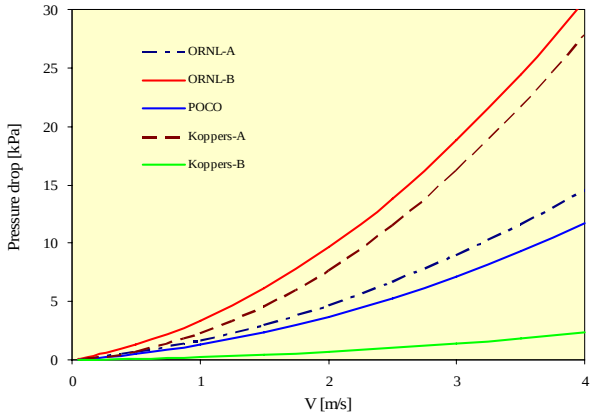

Figure 2. Pressure drop as a function of channel velocity, *v*. The symbols are measured data and the curves are generated from classical Darcy-Forchheimer law with the values of permeability and form drag summarized in Table 2.

Table 2. Summary of permeability and Forchheimer coefficients for the carbon foam specimens tested

Specimen	Permeability, K [m^2]	Forchheimer Coefficient, e_f
ORNL-A	4.46E-10	0.4548
ORNL-B	2.41E-10	0.7444
POCO™	6.13E-10	0.4457
Koppers-A	5.69E-10	1.3445
Koppers-B	3.89E-09	0.2453

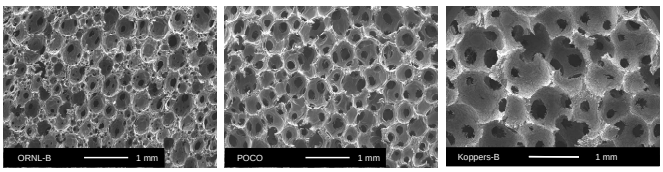

Figure 3. SEM images of graphite foams with varying pore structures.

Pressure drop data can be compared in terms of permeability with similar results obtained for aluminum foams. Boomsma and Poulikakos[4] evaluated the permeability of 6101 aluminum alloy foams with and without compression. The uncompressed foam had porosities in the range of 92–93% and internal surface areas of 820—2700 m^2/m^3, while the compressed foams had porosities in the range of 66–88% and internal areas 2 to 4 times higher. Compared with the Koppers-B foam, which has the lowest

pressure drop among the foams tested, a 6101 compressed aluminum foam of similar porosity has a permeability approximately three times higher. It is much easier to pass a fluid through the aluminum foam, largely because of the difference between the internal structures of the aluminum and graphite foams. The aluminum foam is composed of thin fused strands and large open cell windows but relatively little internal surface area. The graphite foam is composed of spherical voids and smaller cell windows but a larger amount of internal surface area. Since the low permeability of the current graphite foam is due to the restrictive cell windows that link the spherical voids, modification of the graphite foaming process could provide larger and smoother cell windows and lower the hydraulic loss.

The thermal performance of each foam was determined based on the temperature rise of the fluid across the specimen, and a thermal model that considers the block to be an extended surface heated from one side was used. The thermal performance of graphite foam was considerably better than that of an equivalent aluminum (or other metal foam) block as a result of the higher effective conductivity and the increased surface-area-to-volume ratio of the porous graphite foam. Results indicated significant advantages to using graphite foam as an extended surface convective enhancement material in energy exchange and electronic cooling applications.

Thermosyphon System

A third-generation thermosyphon test rig was designed and built to continue the evaluation of graphite foams in an evaporative cooling system. A thermosyphon uses the latent heat of vaporization of a low-boiling-point fluid to dissipate heat. The heat is transferred from the source to the graphite foam, which is submerged in the fluid. The foam provides larger surface area and nucleation sites for boiling to occur. The vapor formed rises into the condenser section of the system, where it is condensed and drips back down to the evaporator section. This forms a closed-loop system that allows the heat to be transferred from a small source to a larger area where condensation takes place. A schematic and a photo of the thermosyphon system built for the current project are shown in Figures 4 and 5, respectively.

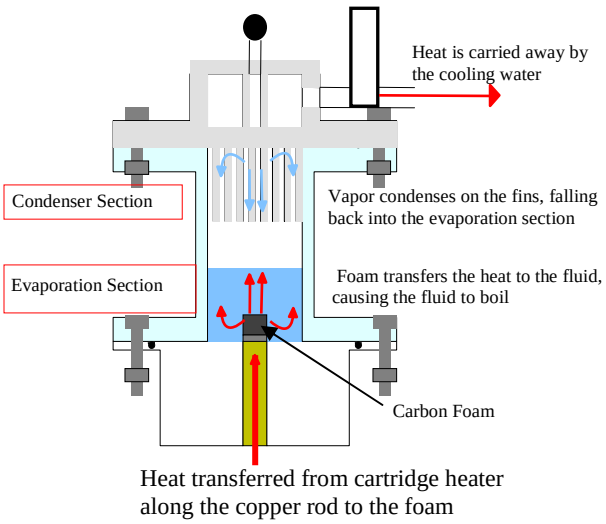

Figure 4. Schematic of thermosyphon test rig.

Figure 5. Photograph of third-generation thermosyphon test rig.

A generic heat source was created by using a cartridge heater embedded in a copper rod that was insulated in a low-conductivity glass-wool–filled PTFE housing. The heat was transferred axially along the copper rod and measured along the rod at three different locations. This allowed the heat flux to be calculated and the surface temperature of the rod to be extrapolated. The graphite foam was attached to the copper by spray-coating the bottom surface of the foam with copper and then soldering

the two surfaces together. The condenser had the top surface of its aluminum fins controlled by cooling water. The fluid used in the experiments was HFE-7000, a Novec Engineered fluid by 3M with a boiling point of 34°C.

Heat sources of three different diameters (½, ¾, and 1 in.) were used to evaluate the effect of sample size (diameter and height) on system performance. Table 3 lists the dimensions of the graphite foam samples used in the experiments, as well as their corresponding external surface areas and volumes (not accounting for the internal surface area due to the pores). Results from these tests are being used to determine if changes in the boiling convection are due to the increased surface area of the foam or to capillarity due to the internal pore structure. Samples from the first set of tests (tests 1–3) had a total external surface area of about 2.56 in.^{2}, while samples from tests 4–6 had a surface area of 1.64 in^2.

Figure 6 plots the heat flux versus wall temperature for samples 1–6. It was observed that samples of 0.75–in. diameter performed slightly better than samples of either 0.5- or 1-in. diameter. The reason for this improved performance is not known yet, but there may be an optimum diameter that balances the capillarity of the internal pores and the increased surface area. It was also observed that most of the nucleation sites were near the bottom of the foam.

Addition of Nanofluid to the Thermosyphon

In collaboration with GM, the use of nanofluids in the graphite foam-based thermosyphon was evaluated. The thermosyphon test setup was used to compare the boiling performance of pure deionized (DI) water and that of a nanofluid. The nanofluid was synthesized using 1% volume fraction of 30-nm Al_2O_3 particles dispersed in DI water. A photo of the nanofluid in the chamber is shown in Figure 7. Figure 8 compares the performance of the thermosyphon (heat flux versus wall temperature) using DI water with its performance using the nanofluid. It is observed that, for a given heat flux, the use of the nanofluid resulted in a lower surface temperature, indicating an increase in performance. Some nanoparticles fell out of solution and attached to the foam surface and pores. This observation is similar to those in other studies where researchers found changes in surface roughness due to sedimentation. This phenomenon may increase the surface area of the foam, provide more nucleation sites, and subsequently increase the boiling performance.

Table 3. Dimensions of samples used for testing.

Test	Diameter (in.)	Length (in.)	Surface Area (in.^{2})	Volume (in.^{3})	SA/V
1	0.960	0.605	2.548	0.438	5.820
2	0.710	0.970	2.560	0.384	6.665
3	0.475	1.600	2.565	0.284	9.046
4	0.960	0.304	1.641	0.220	7.456
5	0.710	0.553	1.629	0.219	7.442
6	0.475	0.980	1.640	0.174	9.441

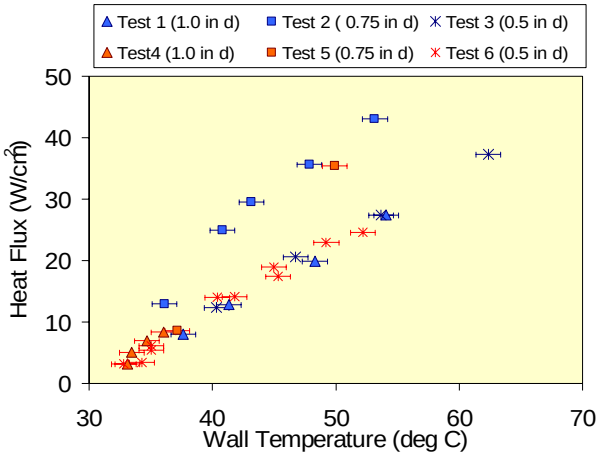

Figure 6. Plot of heat flux versus wall temperature for samples tested.

Summary

Work in FY 2006 focused on developing foams with varying pore structures and morphologies and studying their hydrodynamic and thermodynamic performance. Experimental results showed a wide range of performance corresponding with the wide range of pore structures. The new ORNL and Koppers foams had the best hydrodynamic performance, i.e., lower pressure drop for a given fluid velocity. Results also showed that the thermal performance of graphite foam was considerably better than that of an equivalent aluminum foam block, indicating significant advantages for using graphite foam as an extended surface convective enhancement material in electronic cooling applications.

Studies of the boiling heat transfer on the surface of graphite foam showed that the addition of nanoparticles to the circulating fluid increases the

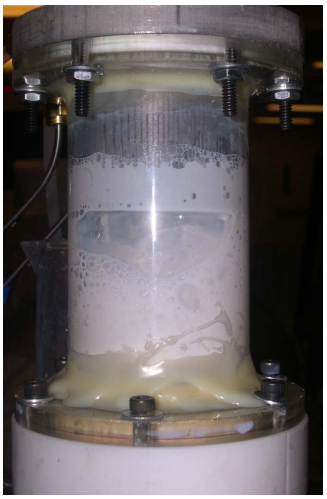

Figure 7. A picture of the fluid in the chamber.

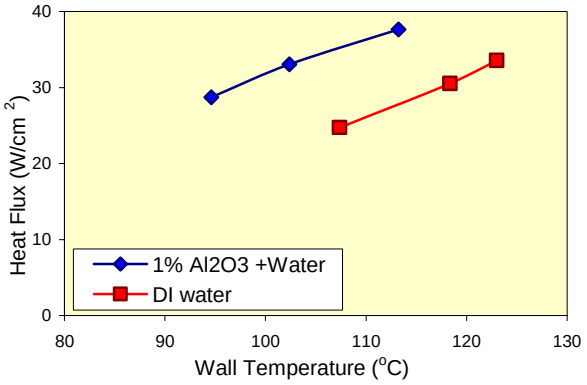

Figure 8. A plot of heat flux into the system and the surface temperature.

performance of the thermosyphon system. This work was conducted in collaboration with GM.

References

1. W. J. Klett, R. Hardy, E. Romine, C. Walls, T. Burchell, "High-thermal-conductivity, Mesophase-pitch-derived Carbon Foam: Effect of Precursor on Structure and Properties," *Carbon* **38**, 953–973 (2000).
2. N. C. Gallego and W. J. Klett, "Carbon Foams for Thermal Management," *Carbon* **41**, 1461–1466 (2003).
3. W. J. Paek, H. B. Kang, Y. S. Kim, and M. J. Hyum, "Effective Thermal Conductivity and Permeability of Aluminum Foam Materials," *Int. J. of Thermophysics* **21**(2), 453–464 (2000).
4. K. Boomsma and D. Poulikakos, "The Effects of Compression and Pore Size Variations on the Liquid Flow Characteristics in Metal Foams," *ASME J. Fluids Engineering* **124**, 263–272 (2002).

Publications/Presentations

Publications

Q. Yu, A. G. Straatman, and B. E. Thompson, "Carbon-foam Finned Tubes in Air–water Heat Exchangers," *Applied Thermal Engineering* **26,** 131–143 (2006).

Q. Yu, B. E. Thompson, and A. G. Straatman, "A Unit Cube-based Model for Heat Transfer and Fluid Flow in Porous Carbon Foam," *ASME Journal of Heat Transfer* **128,** 352–360 (2006).

A. G. Straatman, N. C. Gallego, B. E. Thomson, and H. Hangan, "Thermal Characterization of Porous Carbon Foam—Convection in Parallel Flow," *International Journal of Heat and Mass Transfer* **49,** 1991–1998 (2006).

A. G. Straatman, N. C. Gallego, Q. Yu, and B. E. Thompson, "Forced Convection in Porous Carbon Foam," Submitted to *ASME J. Heat Transfer*, January 2006.

A. G. Straatman, N. C. Gallego, Q. Yu, and B. E. Thompson, "Characterization of Porous Carbon Foam as a Material for Compact Recuperators," Accepted in *ASME J. of Engineering for Gas Turbines and Power*, June 2006.

Presentations

L. J. Betchen and A. G. Straatman, "An Investigation on the Effects of Porosity Gradient on Non-equilibrium Heat Transfer in Porous Carbon Foam," *Proceedings of the 14th Annual Conference of the CFD Society of Canada*, Kingston, Canada, July 2006.

A. G. Straatman, N. C. Gallego, Q. Yu, and B. E. Thompson, "Characterization of Porous Carbon Foam as a Material for Compact Recuperators," *Proceedings of the ASME Turbo Expo 2006*, Barcelona, Spain, May 2006.

C. Mechanical Characterization of Electronic Materials and Electronic Devices

A. A. Wereszczak, T. P. Kirkland, and H. -T. Lin
Ceramic Science and Technology Group
Oak Ridge National Laboratory
P.O. Box 2008, MS 6068, Bldg. 4515
Oak Ridge, TN 37831-6068
(865) 576-1169; fax: (865) 574-6098; e-mail: wereszczakaa@ornl.gov

DOE Materials Technologies Team Leader: Jerry Gibbs
(202) 586-1182; fax: (202) 586-1600; e-mail: jerry.gibbs@ee.doe.gov
ORNL Technical Advisor: David Stinton
(865) 574-4556; fax: (865) 241-0411; e-mail: stintondp@ornl.gov

Contractor: Oak Ridge National Laboratory, Oak Ridge, Tennessee
Prime Contract No.: DE-AC05-00OR22725

Objectives

- Support dielectric polymer film and ceramic nano-dielectric development at Sandia National Laboratories (SNL).
- Compare mechanical performance of SNL-processed dielectric film (measured in FY 2004–FY 2005) with that of a dielectric film from a Toyota Prius capacitor.
- Characterize SNL nano-dielectric microstructures and develop finite element analysis (FEA) models to aid in strength and device performance interpretations.

Approach

- Mechanically evaluate next generation of SNL polymer dielectric films (PPS).
- Mechanically evaluate Toyota Prius dielectric film for comparison.
- Initiate mechanical evaluation of SNL nano-PLZT (lead lanthanum zirconium titanate) dielectric ceramics.

Accomplishments

- Determined that the dielectric film (polyethylene teraphthalate) in the Prius capacitors exhibits a very large amount of strain-to-failure.
- Initiated characterization of grain-size microstructures in SNL-processed nano-PLZT dielectrics.
- Developed FEA models whose results guided PLZT strength coupon design.

Future Direction

- Characterize strength distributions of nano-PLZT ceramic dielectrics.
- Develop models that can be used to optimize multilayer ceramic capacitor (MLCC) design and predict MLCC reliability.

Introduction

A primary focus of the Power Electronics effort in the Automotive Propulsion Materials Program is to develop novel polyfilm and nano-ceramic dielectrics that address high-temperature/electric requirements for dc bus capacitors for power electronic modules in hybrid electric vehicles. The ultimate objective is to make the power modules more compact while maintaining tight voltage and temperature requirements and long service life. Furthermore, these specifications are to be achieved without compromise caused by mechanical breakdown of the candidate dielectric film or nano-ceramic dielectrics.

SNL surveyed companies and the technical literature and found that multilayer ceramic or polyfilm capacitors are the best choices for dc bus capacitors. Polymer film capacitors are the most cost-effective; ceramic capacitors are smaller and have better high-temperature characteristics.

The mechanical reliability of polymer and ceramic dielectrics can be a limiter of their intended electronic function; this project is intended to evaluate their mechanical capabilities by specifically testing polyfilm and ceramic dielectrics developed or supplied by SNL.

Results

Test results are grouped into two categories: those from the polymer film testing and those from the nano-ceramic dielectric characterization.

Polymer dielectric testing

The intent is to develop polymer dielectric films for eventual fabrication into a cylindrical capacitor geometry. Such a capacitor is shown in Figure 1. A pneumatic gripping test system (Figure 2) is used to measure tensile strain-to-failure of the films. Strain-to-failure dependencies on temperature for SNL-2005-processed films are shown in Figure 3. To compare these strains-to-failure against a dielectric film already in service, SNL supplied a polyethylene teraphthalate dielectric film that was extracted from a Toyota Prius capacitor (Figures 4–5). Strips were cut from the roll shown in Figure 5 that had a 12.7-mm width and approximately a 100-mm length. They were tensile tested in displacement control with tensile load and elongation continuously monitored. This film's strains-to-failure were several times that of the films shown in Figure 3 at room temperature (Figure 6) and were an order of magnitude higher at elevated temperatures (Figure 7). The test coupons shown in Figure 8 illustrate the large strains-to-failure. This response strongly suggests that the mechanical reliability of this film will not be problematic.

Figure 1. Photo of 0.2-µF wound capacitor.

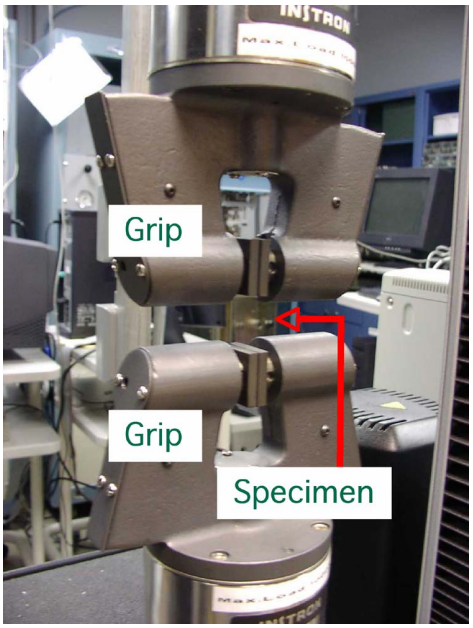

Figure 2. Polymer film tensile test gripping setup.

Nano-ceramic dielectric characterization

Two groups of supplied PLZT specimens were provided by SNL. One was "bulk" processed and

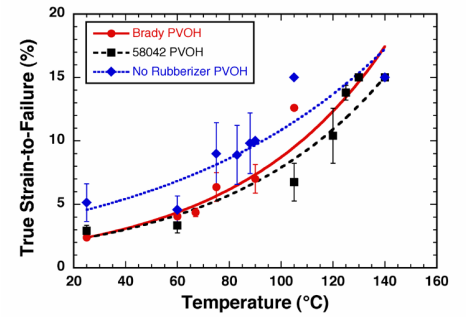

Figure 3. Strain-to-failure of 2005 SNL-processed films as a function of temperature.

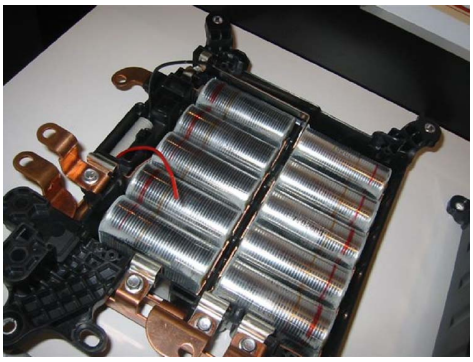

Figure 4. Bank of capacitors in 2004 Prius inverter.

Figure 5. Extracted capacitor roll from Prius inverter.

the second was processed via a chemical route. Microstructures of the as-processed surfaces of both are shown in Figures 9 and 10.

Only a few specimens of each film were provided, so statistically significant strength distributions were unobtainable. Specimen sizes were small,

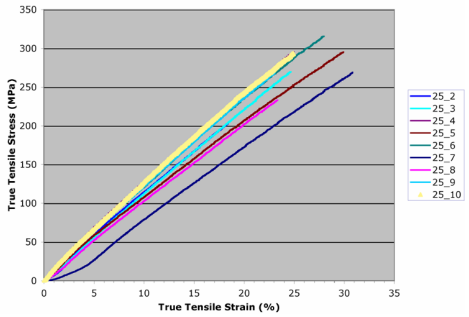

Figure 6. Room temperature strains-to-failure of Prius capacitor film.

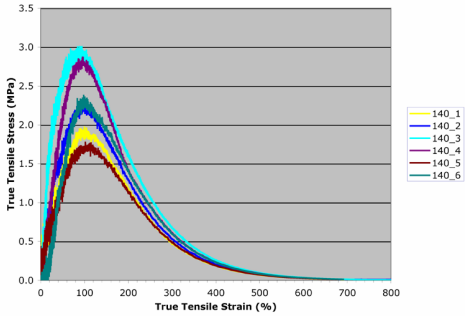

Figure 7. 140°C strains-to-failure of Prius capacitor film.

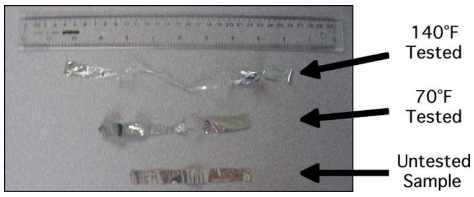

Figure 8. Tested Prius capacitor films.

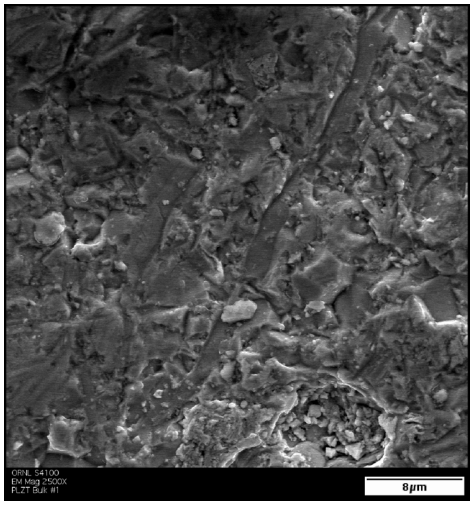

Figure 9. Surface microstructure of "bulk-processed" PLZT ceramic dielectric.

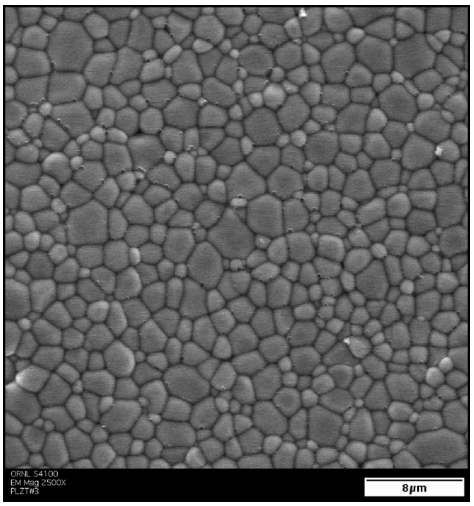

Figure 10. Surface microstructure of PLZT nano-ceramic dielectric.

and thicknesses were only on the order of 200 microns. Strength testing was therefore relegated to ball-on-ring biaxial flexure testing (test setup shown in Figure 11). In preparation for measurement of future strength distributions, an FEA model was created (Figure 12) to enable stress field interpretations and effective area analysis for Weibull strength-size scaling. An example of the fracture surface of one of the tested specimens is shown in Figure 13. Failure initiated at the specimen surface, and there is a suggestion that a localized asperity may have created a stress concentration prompting specimen fracture. Such fractographical examinations will be performed in future testing, and their results can guide strength improvement.

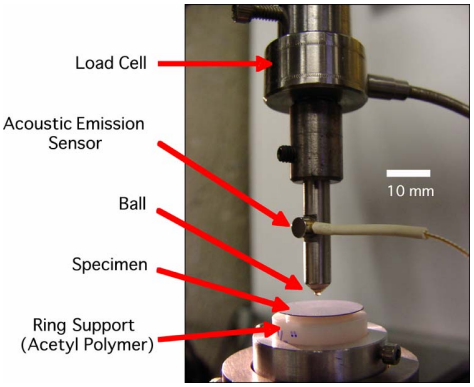

Figure 11. Ball-on-ring biaxial flexure test setup used to evaluate small coupons.

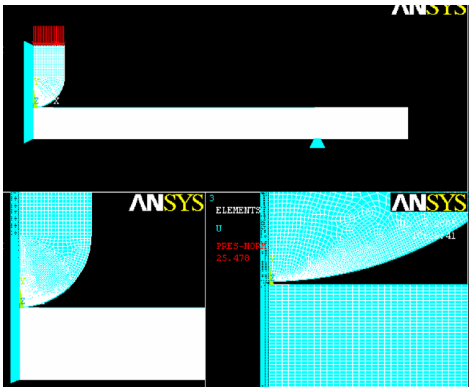

Figure 12. FEA model of ball-on-ring biaxial flexure test setup.

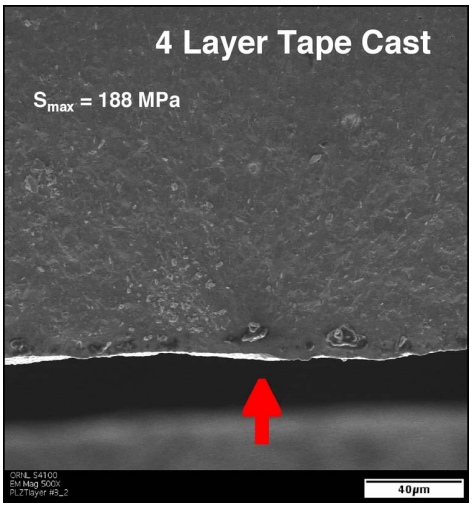

Figure 13. Example of failure initiation location in a biaxial-strength-tested ceramic dielectric specimen.

Conclusions

The polyethylene teraphthalate dielectric film from the Toyota Prius capacitors exhibited a very large amount of strain-to-failure. Such a response is one to which to aspire as future dielectric films are developed.

Characterization of grain-size microstructures in SNL-processed nano-PLZT dielectrics was initiated and FEA models were developed whose results guided PLZT strength coupon design. Quantification of strength distributions can now validly proceed when additional test coupons are provided.

3. CIDI ENGINES

A. Fabrication of Micro-orifices for Diesel Fuel Injectors

John B. Woodford and George R. Fenske
Argonne National Laboratory
9700 South Cass Avenue
Argonne, IL 60439
(630)252-5190; fax (630)252-4798; e-mail: gfenske@anl.gov

DOE Technology Development Manager: Jerry Gibbs
(202) 586-1182; fax: (202) 586-1600; e-mail: jerry.gibbs@ee.doe.gov

Contractor: Argonne National Laboratory, Argonne, Illinois
Prime Contract No.: W-31-109-Eng-38

Objectives

- Develop a methodology for reducing the diameters of fuel injector orifices to 50 μm by applying material to the internal diameter (ID) of the orifice. Micro-orifices should improve fuel distribution, increase efficiency, and reduce emissions.
- Characterize the spray and combustion properties of the fuel injector system coated with electroless nickel (EN) and other advanced ID coating processes.
- Transfer the developed technology to DOE industrial partners.

Approach

- Transfer EN plating deposition technology for reducing the orifice diameter to a commercial plating company.
- Evaluate the potential of EN plating for improving the surface finish and reducing deposit formation on injector nozzles.
- Evaluate the potential of vapor deposition processes to form uniform nickel (Ni) coatings.

Accomplishments

- Devised a new approach for preparing test nozzles in concert with the U.S. Environmental Protection Agency–National Vehicle and Fuel Emissions Laboratory (EPA-NVFEL). Also initiated collaboration with a major fuel injector manufacturer for further engine testing of plated nozzles for deposit mitigation.
- In concert with Imagineering, Inc., a commercial plating company, developed a method for improving the surface finish of commercial-scale plated nozzles.
- In the area of deposit formation testing, refined the test method to include examination of oxidative volatiles and characterized the effect of phosphorous levels in the EN plating on deposit formation. Provided alloy samples for testing to Pennsylvania State University and began to work with Northern Illinois University (NIU) on studying this issue.
- Developed an X-ray phase contrast imaging technique for nondestructive examination of thin EN coatings applied to the interiors of diesel injectors.

Future Direction

- Characterize spray characteristics of coated injectors in collaboration with Argonne National Laboratory–Energy Systems (ANL–ES) and ANL–Advanced Photon Source (ANL–APS).
- Provide coated injector tips to EPA-NVFEL personnel for spray characterization and combustion tests.
- Apply advanced characterization methods for detailed examination of surface chemistry during deposit formation, particularly extended X-ray absorption fine structure (EXAFS).
- Evaluate the potential of high-rate deposition processes based on vapor deposition and alternative EN bath chemistries.

Introduction

In 2007, EPA regulations mandate diesel engine emission reductions to 0.01 grams of particulate matter (PM) per engine horsepower per hour and 0.2 grams of nitrogen oxides (NO_x) per engine horsepower per hour. Further reductions are expected for 2010. To achieve these levels, engines are being redesigned to reduce in-cylinder soot production. One design change under consideration is the reduction of the fuel injector orifice diameter.

Pickett and coworkers[1,2] have shown elimination of soot in a test cylinder by reducing the injector orifice diameter to 50 μm, even with high levels of exhaust gas recirculation and concomitant reduction in NO_x emissions. NVFEL researchers have observed reduced PM emissions from a light-duty diesel engine equipped with 75-μm-diam injector orifices. These reductions arise from increases in fuel atomization efficiency, leading to more complete combustion.[3] Although it is currently possible to economically mass-produce injectors with 100-μm-diam orifices using electrodischarge machining, further reductions in hole size are accompanied by unacceptable fabrication error rates.

Reducing orifice diameter (e.g., from 150 to 50 μm) carries with it a number of penalties, however. It will lead to a reduction in the amount of fuel that can be delivered to the combustion chamber without increasing the number of spray holes, the injection pressure, and/or the discharge coefficient. The potential impact of coking on smaller orifices is also much greater, as smaller holes will be more readily blocked by coking deposits on the injector tip and in the spray holes themselves. Coking deposits are a particular problem with tapered-orifice nozzles, another technique for increasing fuel atomization and thus reducing PM emissions.

Another issue is alternative fuels. One method to minimize dependence on foreign oil is the increased use of bioderived fuels such as vegetable oil esters. Because of the presence of carbon-carbon double bonds in the carboxylic acid chain precursors, these fuels readily form coking deposits in the combustion chamber—a major problem in concert with smaller spray holes. Other alternative fuels include alcohols such as methanol or ethanol. These are not typically used neat but are blended with conventional diesel fuel. One emissions reduction strategy is to inject an ethanol/water mixture along with conventional fuel, reducing combustion temperature and NO_x emissions. However, alcohol partial oxidation products can include corrosive carboxylic acids, which will damage the steel nozzles over time.

In concert with more commonly used fabrication techniques, EN plating has been used to prepare fuel injector nozzles with orifice diameters as small as 50 μm. EN plating also promises to mitigate or solve all of the difficulties described above. The plated surface is corrosion-resistant and smoother, and the discharge coefficient of the plated orifices is higher. This method can be used to deposit a wide variety of alloys, offering the possibility of tailoring surface chemistry to reduce or eliminate deposit formation.

Approach

As described in previous reports, orifice diameter can be reduced by coating the orifice interior with EN plating. This technique has been used to deposit nickel/phosphorous or nickel/boron alloys onto metallic surfaces from aqueous solutions. It has been successfully used in previous years to reduce orifice diameter from 200 to 50 μm on a bench scale, and from 180 to 75–80 μm on a commercial scale. Other metal alloys have been deposited using the same principle.

Having demonstrated that EN plating reduces orifice diameter to the desired size, the next goal is to demonstrate the usefulness of EN-plated nozzles for solving the problems described in the Introduction: improving spray properties and discharge coefficient, reducing deposit formation, and resisting corrosion. To this end, the use of Argonne's APS was explored for nondestructive examination of plated nozzles. This technique is capable of measuring coating thicknesses on internal passages, and it will be applied as a quality check on nozzles that have been sent to EPA for engine tests.

Results

Initial research focused on demonstrating the feasibility of coating internal passages with EN. The early lab results on single nozzles were very successful. Commercial nozzles with orifices 200 µm in diameter and 1 to 1.55 mm long were plated with EN, producing an orifice 50 µm in diameter. Figure 1 presents scanning electron microscopy (SEM) images of a coated nozzle produced with laboratory setup. The interior of the coated nozzle (Figure 1a) is quite smooth. The SEM image of a cross-sectioned nozzle (Figure 1b) further demonstrates the smooth finish of the EN coating.

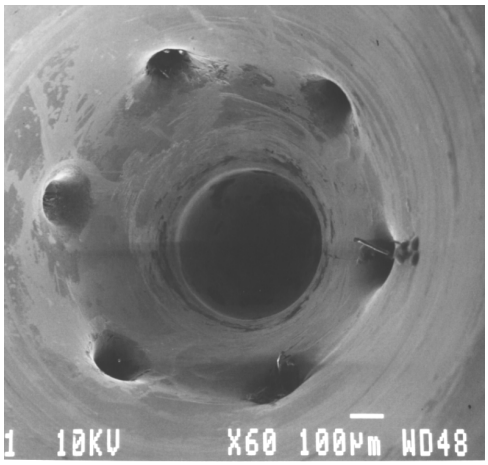

Figure 1a. SEM image of nozzle interior (coated).

A number of nozzles deposited with the laboratory setup were sectioned to measure the uniformity of the coating through the length of the orifice. Figure 2 shows the orifice diameter (initial diameter was 200 µm) as a function of position from the outside of the injector. As is evident from the data, the diameter of the orifice is quite uniform. Adjusting the flow through the orifices can produce tapered holes, with the direction of the taper dependent on the direction of flow.

During the next stage of research, the EN plating concept was transferred to a commercial plating company (Imagineering) specializing in electroless coating—particularly Ni-phosphorous coatings. Imagineering modified its coating process to elimi-

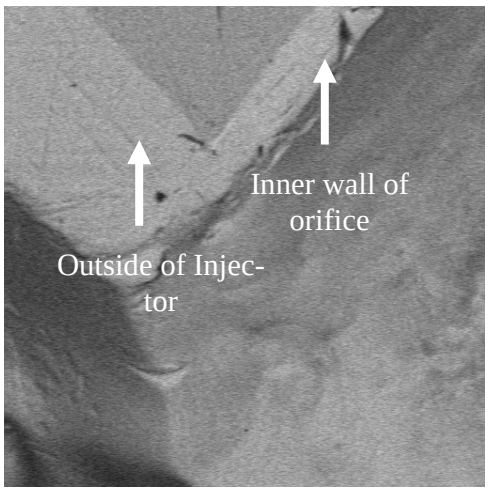

Figure 1b. SEM image of coated orifice.

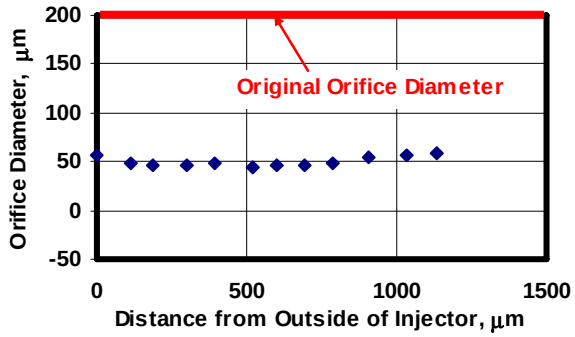

Figure 2. Diameter of coated orifice as a function of position.

nate surface blemishes/pits observed on initial coating trials. Imagineering also attempted to develop Ni stripping processes to remove EN plating from selected (non-orifice) regions. The company's method of removing EN from a plated surface without damaging the substrate did not work for keeping the needle guide free of plating, and its use of conventional maskants on the guide area did not allow sufficient plating bath flow to coat the orifices

uniformly. Imagineering suggested that the plating be removed mechanically, as EN plating can be ground off. This approach proved to be feasible. The same approach can remove overcoating from the needle seat area,[4] which might otherwise adversely affect needle sealing.

These issues all arise from the use of existing nozzles with matching needles. In production, it is anticipated that needles and nozzles will be ground and lapped after plating. Thus no net cost or increase in time will accrue from the machining, and the only increases in cost will be from the plating process itself.

We also continued deposit formation tests using the test method developed 2 years ago: dropping diesel fuel onto heated plated and unplated surfaces. The test protocol was expanded to include different materials, EN compositions, and higher temperatures (200, 250, and 300°C). The test method has also been refined for use with less-volatile fluids, in this case, a high-oleic-content sunflower oil lubricant. This last change was made to investigate a worst case for deposit formation, in that this oil has a large number of carbon-carbon double bonds and contains no antideposit additives. By weighing the samples before and after heating and again after rinsing with hexane, the mass loss due to the formation of volatiles by oxidative cleavage can be decoupled from the mass gain due to deposit formation.

Previously,[4] we showed that EN plating applied to mild steel significantly reduced the formation of deposits in the presence of high-sulfur (500-ppm) diesel fuel. Results were also presented on ANL proprietary superhard nanocomposite (SHNC) coatings that exhibited near-zero deposit formation when exposed to high-oleic sunflower oils. During FY 2006, deposit formation tests were performed on SHNC coatings exposed to 500-ppm-S diesel and Fischer-Tropsch diesel (FT).

The results are shown in Figures 3 and 4, respectively, for the diesel fuel and FT fuels. In contrast to the excellent deposit resistance observed for the high-oleic sunflower oil, the SHNC coating showed significantly poorer deposit resistance when exposed to either petroleum-based diesel with 500-ppm-S or synthetic FT diesel.

Continuing with a collegial arrangement with EPA-NVFEL, commercial light-duty diesel injectors were procured and coated for tests at the EPA-NVFEL site to measure the impact of reduced orifice size on particulate emissions. A subset of the nozzles provided by the EPA were sent to Imagineering, coated, and returned to Argonne for subsequent nondestructive examination (NDE) to determine the coating thickness and uniformity. Results of the NDE indicated the coating met requirements, and Imagineering was directed to coat the remaining nozzles. The second set of nozzles was inadvertently removed from the EN bath before completion. Attempts to strip the coating and re-

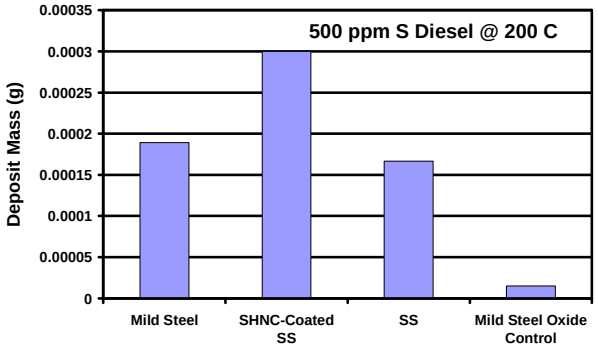

Figure 3. Diesel deposit mass on SHNC coated and uncoated steels (exposed to 500-ppm-S diesel fuel).

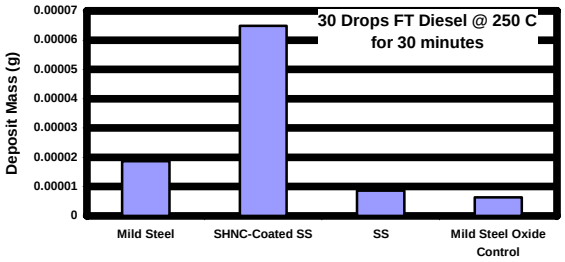

Figure 4. Fischer-Tropsch diesel deposit mass on SHNC coated and uncoated steels.

apply a new coating were not successful. A second set of 125-µm nozzles was procured and sent to Imagineering. All nozzles were coated in one run, and half were removed early at a nominal coating thickness of 25 µm (75-µm final diameter); the second half were removed after 75 µm was deposited. The coated nozzles were shipped to a grinding shop that specializes in custom nozzle fabrication, and

excess coating was removed mechanically to match the pintle to the nozzle.

Figures 5a and 5b show boroscope images of the nozzle interiors for 50- and 75-µm orifices, respectively. Subsequent to the final grinding (to remove excess coating in the pintle region), each nozzle was installed on a flow rig to confirm that flow was maintained through each of the seven orifices. All of the 75-µm nozzles exhibited uniform flow (visual inspection); however, two of the 50-µm nozzles exhibited some degree of blockage. Figure 6 shows a boroscope image of one of the blocked nozzles. The cause for the blockage is under investigation.

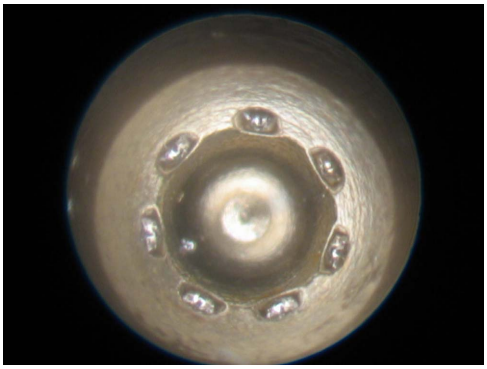

Figure 5a. Boroscope image of the interior of a 7-orifice nozzle coated with EN to a final orifice size of 75 µm.

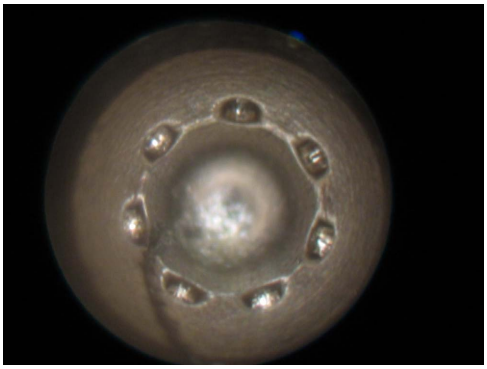

Figure 5b. Boroscope image of the interior of a 7-orifice nozzle coated with EN to a final orifice size of 50 µm.

As part of an effort to provide a nondestructive technique to measure the thickness and uniformity of the EN coatings applied to injectors prior to engine tests, ANL supported the development of a phase-contrast imaging technique at the APS.[5] This imaging technique provides a high-resolution nondestructive metrology tool for examining the injection nozzle orifice before and after fabrication (Figure 7). This imaging technique can readily reveal surface finish and possible defects with micron and even sub-µm spatial resolution. More recently, such phase-contrast imaging techniques were further extended to directly visualize fuel jet breakup, spray formation, and liquid atomization. This new development at the APS can be exploited to clarify the significant effect of the small-orifice nozzle on combustion efficiency and engine-out emissions.

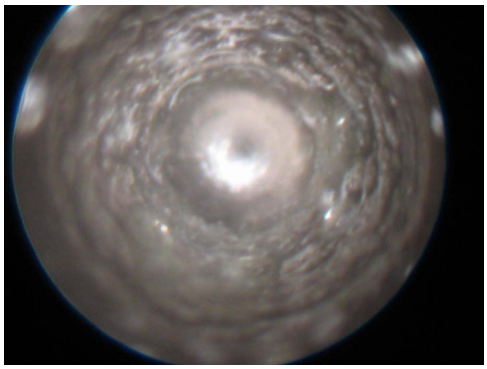

Figure 6. Boroscope image of blocked nozzle.

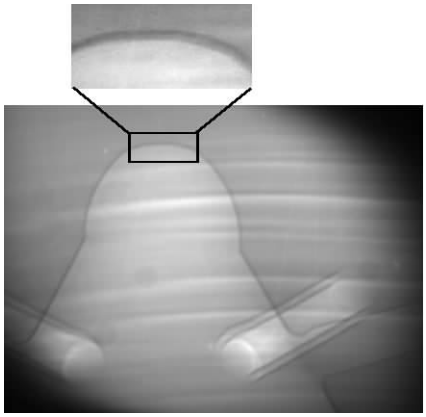

Figure 7. Phase-contrast imaging of an Ni-plated Siemens diesel injector nozzle with six orifices of 200 µm diameter. The scope of view is ~1.4×2.1 mm.

ANL demonstrated the feasibility of measuring the thickness of Ni thin films through mm-thick steel using the X-ray phase-contrast imaging technique. The electron density difference between Ni and steel is very small (10% or so). It was not known if micron-thick Ni film could be visualized through the nozzle housing. Figure 7 shows the phase contrast imaging of a Ni-plated Siemens diesel injector noz-

zle with six orifices of 200-µm diameter each. The top portion in the sac part is magnified to demonstrate that the Ni layer is very thin but readily visible. This image was analyzed at several locations in the sac region (top portion of Figure 7) to quantify the Ni film thickness. While the intended plating thickness was 25 µm, the measurement showed that the thickness varied from below10 µm to 15 µm.

ANL received two additional contacts from outside researchers. One contact, associated with a domestic engine manufacturer, has expressed interest in the use of EN coatings to mitigate premature cavitation wear in laser fabricated orifices. Brittle phases (e.g., martensite) produced along the interior surfaces of laser-fabricated orifices are thought to contribute to rapid cavitation and premature failure. ANL has established a collegial agreement with this firm to coat experimental nozzles for its studies. A second firm has approached ANL to evaluate the use of EN to mitigate deposit formation on light-duty diesel injectors. Negotiations are in progress to define what tests will be performed on the nozzles and to share test data.

Conclusions

A candidate method has been developed for fabricating nozzles with micro-orifices for spray testing, and arrangements have been made with EPA-NVFEL and a major fuel injector manufacturer to perform engine tests in the next year. A series of commercial nozzles were coated by Imagineering and transferred to EPA-NVFEL for emissions tests. Deposit formation studies of a promising SHNC coating, which showed excellent resistance to deposit formation in sunflower oil, indicated that it formed deposits faster than EN or mild steel when exposed to conventional diesel or FT diesel. A novel X-ray phase-contrast imaging technique was applied to image thin EN coatings on the interior regions of commercial six-orifice injectors.

References

1. Lyle M. Pickett and Dennis L. Siebers, Paper No. 2001-ICE-399, ICE Vol. 37-1, ed. V. W. Wong, *2001 Fall Technical Conference, American Society of Mechanical Engineers,* 2001.
2. L. M. Pickett, D. L. Siebers, A. F. Morales, J. Hachman, and A. K. Sinensky, "An Investigation of Diesel Soot Formation Processes Using High Aspect Ratio Micro-Orifices," presented at HARMST 2003 High-Aspect Ratio Micro-Structure Technology Workshop, Monterey, CA, 2003.
3. John B. Heywood, *Internal Combustion Engine Fundamentals*, McGraw-Hill, 1988.
4. John B. Woodford and George R Fenske, "Fabrication of Small Fuel Injector Orifices," *2005 Annual Progress Report, Automotive Propulsion Materials*, U.S. Department of Energy, Washington, D.C., 2005.
5. Kamel Fezzaa, Wah-Keat Lee, Seong-Kyun Cheong, Christopher F. Powell, Jin Wang, and Ming-Chia Lai, "Ultrafast X-ray Phase-Enhanced Microimaging for Visualizing Fuel Injection Process," SAE 2005-24-093, Society of Automotive Engineers, 2005.

Publications and Presentations

J. Woodford and G. Fenske, "Fabrication of Small Orifice Fuel Injectors," DEER (Diesel Engine Emissions Reduction) 2005, August 2005.

J. B. Woodford and G. R. Fenske, *Fabrication of Small-Orifice Fuel Injectors for Diesel Engines*, Argonne National Laboratory Report, ANL-05/06, March 2005.

J. B. Woodford, G. R. Fenske, and J. M. Perez, "Deposit Formation on Electroless Nickel," submitted to *Energy & Fuels*.

Inventions and Patents

G. Fenske and J. Woodford, "Nickel Vapor Deposition Orifice Coatings," ANL-IN-06-030, patent application.

B. Electrochemical NO_x Sensor for Monitoring Diesel Emissions

L. Peter Martin and Robert S. Glass
Lawrence Livermore National Laboratory
P.O. Box 808, MS L-353
Livermore, CA 94551-0808
(925) 423-7140; fax: (925) 423-7914; e-mail: glass3@llnl.gov

DOE Materials Technologies Team Leader: Jerry Gibbs
(202) 586-1182; fax: (202) 586-1600; e-mail: jerry.gibbs@ee.doe.gov

Contractor: Lawrence Livermore National Laboratory, Livermore, California
Prime Contract No.: W-7405-Eng-48

Objectives

- Develop a compact, rapid-response electrochemical nitrogen oxide (NO) or total nitrogen oxides (NO_X) sensor for compression-ignition, direct-injection (CIDI) exhaust gas monitoring.
- Explore and characterize novel, effective sensing methodologies based on impedance measurements.
- Collaborate with the Ford Research Center and Oak Ridge National Laboratory to optimize sensor materials, operating parameters, and performance.
- Identify materials issues pertaining to aging and performance for candidate sensor materials.

Approach

- Use an ionic (O^{2-}) conducting ceramic as a solid electrolyte and metal or metal-oxide electrodes.
- Apply sinusoidal voltage between a working and counter electrode and measure impedance or phase angle shifts to correlate with NO_x concentration.
- Evaluate sensing mechanism using electrochemical techniques.

Accomplishments

- Identified a new impedance-based method using multiple frequencies to compensate for O_2 interference.
- Demonstrated sub-10 ppm NO_x sensitivity over a wide range of O_2 concentrations (<7% to >18%).
- Published one journal article, two in preparation.

Future Direction

- Continue to explore sensing mechanism and apply findings to optimization of the sensing strategy.
- Evaluate cross-sensitivity to important redox gases and perform dynamometer testing.
- Demonstrate the commercialization potential of the impedance-based sensor methodology.
- Transfer the technology to a commercial entity.

Introduction

Increasingly stringent emissions regulations will require the development of advanced gas sensors for a variety of applications. For example, compact, inexpensive sensors are needed for detection of regulated pollutants, including hydrocarbons (HCs), CO, and NO_x, in automotive exhaust. Of particular importance will be a sensor for NO_x to ensure the proper operation of the catalyst system in the next generation of diesel (CIDI) automobiles.

Because many emerging applications, particularly monitoring of automotive exhaust, involve operation in harsh environments that include high temperatures and corrosive or chemically reactive conditions, ceramic-oxide–based electrochemical sensors are of considerable interest. Sensors using yttria-stabilized zirconia (YSZ) as an oxygen-ion-conducting electrolyte have been widely reported for both amperometric and potentiometric modes of operation.[1,2] These include the well-known exhaust gas oxygen (EGO) sensor.

Recently, an ac impedance-based technique has been reported for sensing NO_x, CO, HCs, and humidity using a YSZ electrolyte and various electrode materials.[3–7] In the impedancemetric technique, an ac voltage input signal is applied to the sensor and changes in the complex impedance are measured as the sensing signal. A total-NO_x sensor has been reported that uses a tubular YSZ electrolyte, $ZnCr_2O_4$ sensing electrode, and platinum/air reference electrode.[4] The modulus of the impedance, |Z|, was measured at 1Hz as the sensing signal at 600–700°C. This operating frequency was selected as a compromise between improved response (at lower frequency), and decreased noise and sampling time (at higher frequency). In follow-on work, a planar YSZ configuration was demonstrated for a CO sensor using an Au-Ga_2O_3 sensing electrode.[6] Once again, the sensing signal was provided by measurement of |Z| at 1 Hz.

The current work presents an impedancemetric NO_x sensor consisting of a planar YSZ electrolyte and YSZ/Cr_2O_3 composite electrodes attached with gold leads. The electrodes were nominally identical, and both were exposed to the test gas (i.e., no air reference). NO_x sensing was performed by monitoring the impedance (|Z|) and/or phase-angle (Θ). However, for the current sensor configuration, the Θ response has been shown to provide higher sensitivity and better stability. Cross-sensitivity to O_2 at 10 Hz can be compensated for by using data from a second measurement frequency (1000 Hz) at which the response to NO_x is limited but the response to O_2 is robust.

Experimental

The sensor was fabricated by spray-coating composite electrodes onto a YSZ electrolyte. Electrodes were composed of 10% Cr_2O_3 (by weight) and 90% YSZ, with a geometry consisting of two side-by-side rectangular electrodes on the same side of the electrolyte. The electrodes were fired at 1000°C for one hour and had a thickness of approximately 7.5 microns. Sensor testing was performed in a quartz tube heated in a tube furnace to 600°C. In the test configuration, both electrodes were exposed to the gas flow, and the gas composition was controlled by mixing air, N_2, and 1000-ppm NO or NO_2 in N_2 using a standard gas handling system equipped with thermal mass flow controllers. A foil was overlaid on top of the sensor electrodes to provide electrical contact. The foil was held in place by an Al_2O_3 flat spring-loaded to apply a constant pressure. Electrochemical measurements were performed using a Solartron 1260 Impedance Analyzer and the ZPlot software.

Results

Figure 1 shows the impedance spectrum for the sensor at 600°C in 10.5% O_2. Also shown are the spectra for 100 ppm concentrations of NO and NO_2 at the same O_2 concentration. Points corresponding

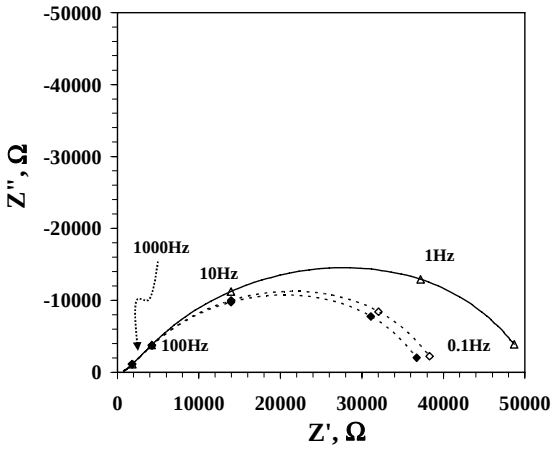

Figure 1. Impedance spectrum of the sensor for 10.5% O_2 (open triangles), 100 ppm NO (filled diamonds), and 100 ppm NO_2 (open diamonds).

to 0.1, 1.0, 10, 100, and 1000 Hz are marked on each spectrum. The data indicate that the cell has a high dc impedance of approximately 50 kΩ and that the dc impedance decreases markedly with the introduction of NO_x to the gas stream. Two arcs were observed within the frequency range explored: a small arc at high frequencies above approximately 100 kHz (too small to be visible in the figure) and a large arc visible below 1 kHz. The small, high-frequency arc is insensitive to the presence of NO_x; however the large, low-frequency arc is significantly depressed with the introduction of either NO or NO_2.

Figure 2 shows Θ and |Z| measured during continuous operation at 10 Hz. The data show the sensor response as the O_2 concentration is cycled through the sequence 10.5, 2.0, 7.0, 10.5, and 18.9%. These O_2 concentrations are indicated in the figure, and the sensor response to the changing concentrations is clearly apparent. At each O_2 concentration, NO_x exposures are achieved by introducing 50, 25, 15, and 8 ppm of NO followed by the same levels of NO_2. The responses to these NO_x additions are the stair-step signals superimposed on the O_2 response curve. The responses to NO and NO_2 are comparable in magnitude, with the NO response being slightly larger. The Θ response to the NO_x exposures is particularly apparent and is significantly more pronounced than the |Z| response. Also, the Θ response is significantly more sensitive to NO_x than the |Z| response at all O_2 concentration levels, with 8 ppm of NO_x clearly resolvable. Relative to |Z|, the Θ response is faster and more stable over the course of the measurements.

Figure 3 is identical to Figure 2, except that the measurement frequency has been increased to 1000 Hz. At this higher frequency, the sensor shows no response to NO_x in either Θ or |Z|. It is noteworthy, however, that the response to changes in the O_2 concentration shows qualitatively the same behavior as that observed during 10-Hz operation. In fact, this similarity is sufficient to allow compensation of the baseline (i.e., zero NO_x) measured at 10 Hz for the effect of changes in the O_2 concentration. This compensation is made using the linear relationship (obtained by linear least squares regression analysis) between the Θ response measured at 10 and 1000 Hz. To correct for the baseline at 10 Hz, where NO_x is detected, the response at 1000 Hz is measured and from it the predicted response at 10 Hz is calculated. This value is then subtracted from the

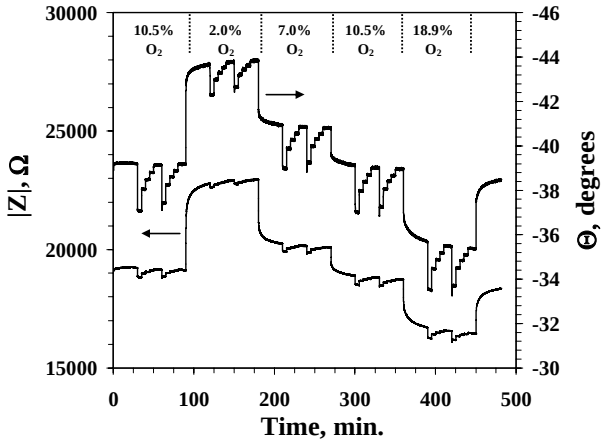

Figure 2. |Z| and Θ measured at 10 Hz. The O_2 concentration varies from 2 to 18.9%, and NO_x exposures of 50, 25, 15, and 8 ppm of NO (first) and NO_2 (second) are performed at each concentration.

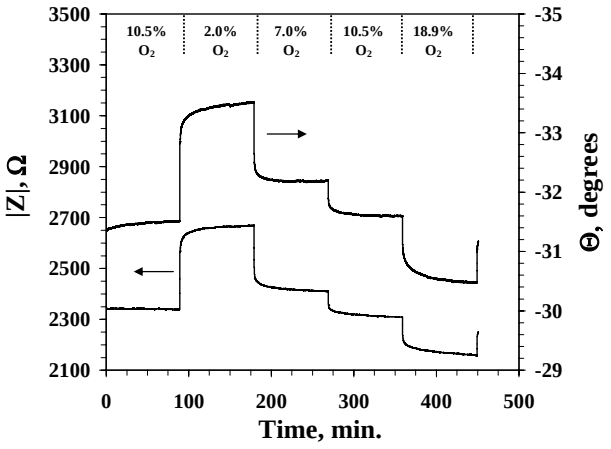

Figure 3. |Z| and Θ measured at 1000 Hz. The O_2 concentration varies from 2 to18.9%, and NO_x exposures of 50, 25, 15, and 8 ppm of NO (1^{st}) and NO_2 (2^{nd}) are performed at each concentration.

measured Θ (10 Hz) response to obtain the response due to NOx alone.

Figure 4 shows the compensated sensor response as a function of the concentrations of NO and NO_2 for different baseline O_2 concentrations. An approximately linear relationship is found at all O_2 concentrations in the range of 2–18.9%. The response in 2% O_2 varies from that for the other concentrations as a result of a slow O_2 response. While these results clearly indicate that it is possible to detect low levels of NO_x in the laboratory, significant improvement will probably be necessary before the

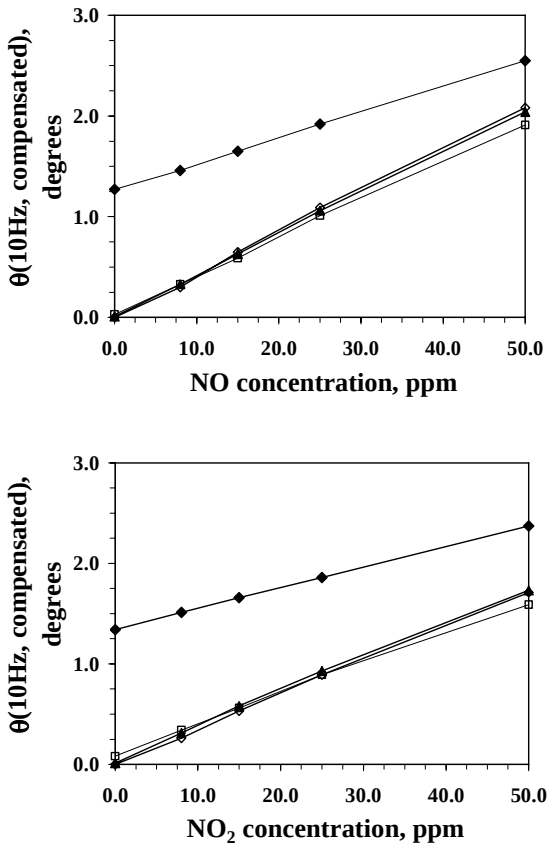

Figure 4. Compensated sensor response Θ(10 Hz) illustrating the NO and NO_2 response at the different O_2 concentrations.

methodology can be deployed in a real application where more significant background noise would be apparent.

Conclusions

A new impedancemetric method for NO_x sensing is described. The sensor consists of a planar YSZ electrolyte and two identical YSZ/Cr_2O_3 composite electrodes. Using ac impedance measurements, the NO_x concentration can be correlated with the measured |Z| or Θ. However, Θ̇ appears to be more stable and show a higher sensitivity to NO_x. The responses to NO_2 and NO are similar in magnitude, with the NO response being slightly larger. Under the conditions employed in this study, Θ measured at 10 Hz is sensitive to both NO_x and O_2 concentrations, while at 1000 Hz it is sensitive only to O_2. An algebraic relationship relating the measured Θ at the two frequencies relative to the changing O_2 concentration allows extraction of the NO_x concentration. The response curve (ΔΘ versus NO_x concentration) is linear over the entire range for background O_2 concentrations ranging from 2 to 18.9%. The response in 2% O_2 is offset from measurements at other O_2 concentration levels because of a slow sensor response to changing O_2. However, this is unlikely to be a problem for operation of the sensor in real applications where the anticipated O_2 levels are expected to be in the range of 6–15% (i.e., for diesel exhaust monitoring). The potential viability of the sensing method has significant implications for "real world" applications, including the opportunity for improved noise correction, faster sensor response time, and reduced sampling time.

References

1. F. Menil, V. Coillard, and C. Lucat, *Sensors and Actuators B* **67**, 1 (2000).
2. W. Göpel, G. Reinhardt and M. Rösch, *Solid State Ionics* **136–137**, 519 (2000).
3. M. Nakatou and N. Miura, *J. Ceram. Soc. Japan* **112**, S532 (2004).
4. N. Miura, M. Nakatou and S. Zhuiykov, *Sensors and Actuators B* **93**, 221 (2003).
5. M. Nakatou and N. Miura, *Solid State Ionics* **176**, 2511 (2005).
6. N. Wu, Z. Chen, J. Xu, M. Chyu and S. X. Mao, *Sensors and Actuators B* **110**, 49 (2005).
7. M. Nakatou and N. Miura, *Electrochem. Comm.* **6**, 995 (2004).

Publications/Presentations

"Impedance Characterization of a Model Au/Yttria-stabilized Zirconia (YSZ)/Au Electrochemical Cell in Varying Oxygen and NO_x Concentrations," submitted to *J. Electrochem. Soc.*

"Impedancemetric NO_x Sensing Using YSZ Electrolyte and YSZ/Cr_2O_3 Composite Electrodes," submitted to *J. Electrochem. Soc.*

"Aging Studies of Sr-doped $LaCrO_3$/YSZ/Pt Cells for an Electrochemical NO_x Sensor," *J. Electrochem. Soc.* **153**, H171–H180 (2006).

C. Hydrogen Materials Compatibility

Chuck Henager, Jr., Stan Pitman, Mike Dahl, Karl Mattlin, Howard Heinisch, Rick Kurtz, Jim Alzheimer, James Holbery
Pacific Northwest National Laboratory
P.O. Box 999
Richland, Washington 99354
(509) 375-3686; fax: (509) 375-2379; e-mail: james.holbery@pnl.gov

Peter Blau, Jun Qu, John Truhan, Jr., Laura Riester
Oak Ridge National Laboratory
Oak Ridge, TN 37831
(865)574-5377; fax: (865) 574-6981; e-mail: blaupj@ornl.gov

DOE Technology Development Manager: Jerry Gibbs
(202) 586-1182; fax: (202) 586-1600; e-mail: jerry.gibbs@ee.doe.gov

Contractor: Pacific Northwest National Laboratory, Richland, Washington
Prime Contract No.: DE AC06 76RLO 1830

Objectives

- Measure the friction and wear characteristics of injector materials in hydrogen environments, including in-situ and ex-situ materials characterization.
- Measure the performance of piezoelectric actuators and actuator materials in hydrogen environments.

Approach

- Develop a test methodology for piezo materials in hydrogen.
- Conduct failure analysis of piezo materials and epoxy layers on actuators.
- Develop models of hydrogen effects on piezo materials.
- Investigate sliding and impact wear on injector materials in hydrogen environments.

Accomplishments

- Conducted hydrogen diffusion modeling, exposure testing, and failure analysis on injector piezo materials.
- Developed a second hydrogen pressure vessel, tested it, and had the vessel line fully safety checked and on-line.
- Completed the design, construction, safety check, and full operation of a high-pressure hydrogen test apparatus for actuator and injector materials, including complete system for in-situ monitoring of piezo materials.
- Conducted hydrogen exposure and initial friction-wear testing of candidate injector needle-nozzle pairs.

In-Situ Piezoelectric Actuator Tests and Analysis

The hydrogen testing capability at Pacific Northwest National Laboratory (PNNL) was greatly increased this year with the addition of a second high-pressure hydrogen autoclave and a second KCI power supply. Currently, up to four actuators can be simultaneously and independently tested and controlled in a wide variety of environments, including up to four at 100°C in 4500 psi (31 MPa) hydrogen.

A new test matrix was devised to help us understand the root cause of actuator failure, and a substantial effort in failure analysis was begun. Figure 1 depicts the dual hydrogen autoclave setup at PNNL in which each autoclave can be independently pressurized and controlled. The data acquisition system was also improved so that simultaneous data can be obtained from up to four actuators.

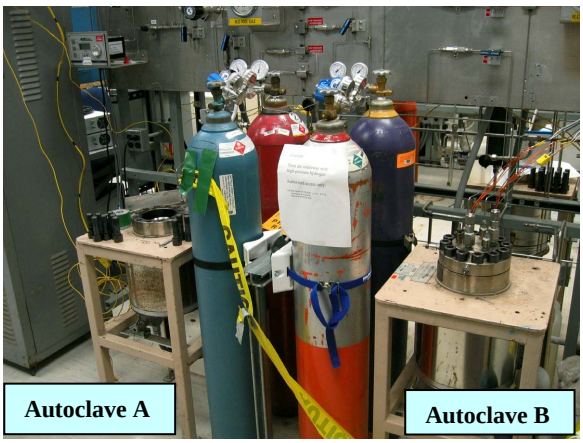

Figure 1. High-pressure hydrogen autoclaves at PNNL, each equipped with high-pressure gas fittings, check valves, and heaters.

The performance of KCI piezoelectric actuators is currently being evaluated in a high-pressure hydrogen autoclave. The autoclave chamber has a pressure rating of 60 MPa and a temperature limit of about 400°C. The system to electrically energize the actuators consists of a KCI power supply controlled by a computer data acquisition system running LabView software. The system is pressurized from high-pressure gas bottles and the oxygen content is determined using an oxygen analyzer. The autoclave has a rupture disk and pressure relief valve in case of an over-pressurization accident, with check valves to isolate the high-pressure hydrogen gas from all components except the high-pressure autoclave.

New actuators were obtained from KCI for FY 2006 testing, and two of the previously tested actuators were examined metallographically for hydrogen degradation. The new actuators were manufactured from the same PZT materials and epoxy as the previous actuators but were smaller in diameter, do not have a hollow central core, and require 1000-V actuation because they have thicker elements, compared with 450-V actuation for the larger actuators.

The older, larger actuators are shown in Figure 2. Both failed in high-pressure hydrogen exposure while being actuated at 450 V. Figure 3 shows the smaller actuators being tested in FY 2006.

Actuators 03-4016 and 03-4044 both failed in high-pressure hydrogen at 100°C after several hundred hours of operation, but such testing does not adequately reveal failure mechanisms or adequately control the test variables to isolate a root cause variable, if any. Control specimens are required, and a clear separation of environmental variables is required to adequately assess failure modes for these materials. Therefore, a test matrix (Table 1) was de-

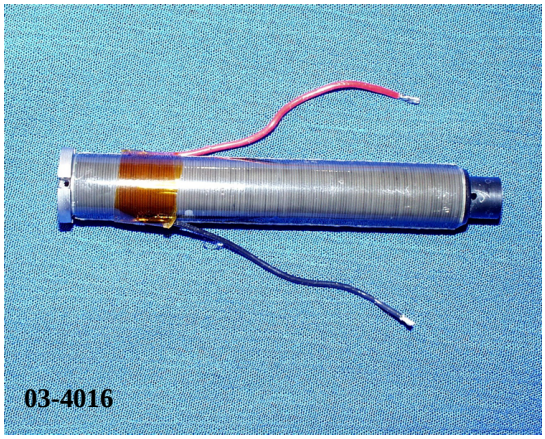

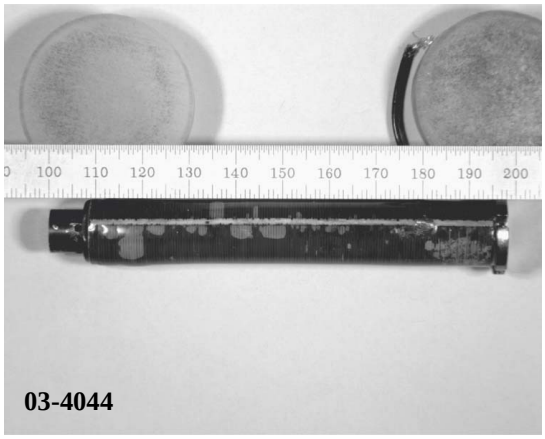

(a) (b)

Figure 2. KCI large actuators tested in high-pressure hydrogen autoclaves at 100°C. (a) KCI 03-4016 tested for 350 h and (b) KCI 03-4044 tested for 580 h. Note the large blisters on actuator 03-4044. Actuator 03-4016 failed in open-circuit condition and 03-4044 failed in short-circuit condition.

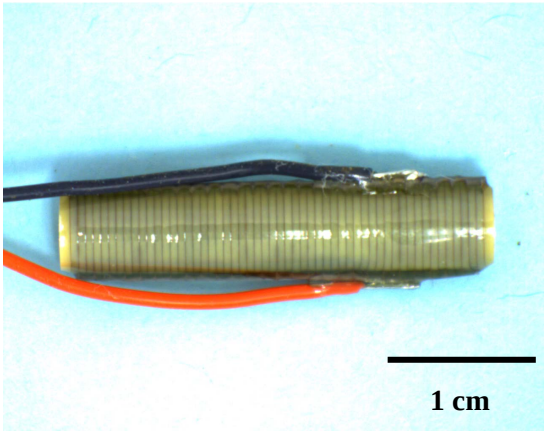

Figure 3. New smaller actuators currently under testing at PNNL. Thirty of these smaller (30×5 mm) actuators have been obtained from KCI for subsequent testing and failure analysis. These actuators require 1000 V to operate.

vised to allow a clear understanding of the effects of various environments on actuator failure. In addition to this test matrix, a more rigorous failure analysis methodology was developed based on a combination of nondestructive and destructive methods. All samples were photographed before exposure or testing. A control sample was prepared using standard metallographic methods, including longitudinal and transverse sections. Optical and scanning electron microscope (SEM) imaging were employed, combined with electron dispersive X-ray (EDX) analysis, Rutherford backscattering (RBS), and elastic recoil detection analysis (ERDA) to determine chemical changes and to locate and quantify hydrogen uptake.

Piezoelectric Actuator Test Results

This year and last year, two large KCI actuators were tested to failure in high-pressure hydrogen at 4600 psi and at 100°C in the PNNL hydrogen autoclaves. These actuators apparently failed without warning or obvious precursor degradation indicators. Accordingly, a new test matrix was devised, shown as Table 1, and new KCI actuators were procured by Westport Innovations for testing. Six of the newer actuators were tested according to the revised test matrix in order to understand the effects of several exposure variables: temperature, atmosphere or hydrogen, and pressure. Table 2 lists the actuator tests performed to date and their outcomes. The failure analysis of each is described in a separate section.

The test results indicate that actuation in high-pressure hydrogen at 100°C can cause failure but that, as indicated in Table 2, actuation in low-pressure hydrogen at ambient temperature does not. Further tests will be required to determine what are the primary variables causing piezoelectric actuator failure. These tests include actuation in high-pressure hydrogen at ambient temperature, actuation in low-pressure hydrogen at 100°C, and then repetition of the high-pressure hydrogen tests at 100°C. This method will effectively isolate the key variables in this case.

Piezoelectric Actuator Failure Analysis

Samples 03-4016 and 03-4044 were examined by a variety of techniques to determine likely failure mechanisms. At this time, no simple mechanism has been identified as the failure mechanism, other than surface corona discharge due to carbon buildup on the actuator beneath the epoxy coating layer in the case of one of the large KCI actuators tested in high-pressure hydrogen, 03-4016. The role of hydrogen in this case is not clear at present. The literature on piezoelectric devices in hydrogen includes papers that discuss a role of hydrogen permeation into the lattice and subsequent electrical property degradation due to changes in internal dipole moments within the crystal from the formation of OH bonds. Apparently, however, this particular degradation mechanism did not occur for these actuators, as the failure seems to be due to surface corona discharge. However, further testing and analysis may be required to reveal this degradation process and to determine the overall reason for the surface discharge that seems to occur.

Figure 4 shows optical photos of actuator 03-4016 and 03-4044 after failure but prior to sectioning. Large delamination regions or bubbles are observed beneath the epoxy coating of the actuators. Actuator 03-4016 was examined more closely with optical microscopy and was then sent to KCI for failure analysis and testing.

Higher-magnification photos of 03-4016 are shown in Figure 5, which shows two interesting features that KCI also identified in its failure analysis as important damage mechanisms. One is the surface discharge signature, which apparently is carbon on the surface of the actuator material underneath the epoxy coating layer. KCI actuated 03-4016 upon receiving it after testing and observed surface dis-

Table 1. Piezoelectric actuator test matrix

Test number	Condition	Test description	Variable explored	Number tested (minimum)
1[a]	Untested controls	No testing	Initial state	1
2[b]	Ambient actuation control	Ambient air or nitrogen under actuation	Actuation	2
3[c]	Hydrogen control	Ambient hydrogen with no actuation	Hydrogen	2
4[d]	Hydrogen actuation control	Ambient hydrogen under actuation	Hydrogen/actuation at ambient	3
5	Temperature control	100°C nitrogen with no actuation	Temperature	2
6[e]	Temperature actuation control	100°C nitrogen under actuation	Temperature/actuation	2
7	Temperature hydrogen control	100°C hydrogen with no actuation	Temperature/hydrogen	2
8	Temperature hydrogen control	100°C hydrogen with actuation	Temperature/hydrogen	3
9	Pressure control	High-pressure hydrogen at ambient with no actuation	Hydrogen/pressure	2
10	Pressure actuation control	High-pressure hydrogen under actuation	Hydrogen/pressure and actuation	3
11	Temperature–pressure–hydrogen control	Temperature, high-pressure hydrogen, actuation	All	5
	Spares			3
	Totals			**30**

[a] Photographed and sectioned.
[b] Actuated for 1376 hours at 1000V in ambient nitrogen.
[c] Exposed for 1073 hours in hydrogen at 150 psi, actuated at beginning and after exposure.
[d] Actuated for 1073 hours in hydrogen at 150 psi.
[e] Actuated for 1241 hours at 1000V in 100˚C nitrogen

Table 2. Specifics of the piezoelectric material tests

Test condition	Sample number	Variable explored	Number tested	Result summary
4600 psi H_2, 100°C	03-4044	H_2, P, T,	1	**Actuated device fails after 580 h.** Destructive failure analysis at PNNL.
4600 psi H2, 100°C	03-4016	H_2, P, T,	1	**Actuated device fails after 350 h.** Nondestructive and destructive failure analysis at KCI.
Untested, control	06-50XX	Control	1	Photographed and sectioned for as-received control sample. **Control only.**
Actuated in Ambient N_2	06-5027	Actuated control, no H_2	1	Sample actuated for 1376 h in N_2 at ambient at 40 Hz, 1000 V. **Benign environment actuation OK.**
Actuated in 100°C N_2	06-5028	T	1	Sample actuated for 1241 h in N_2 at 100°C at 40 Hz, 1000 V. **100°C actuation OK**.
Actuated in Ambient H_2	06-5020 06-5023	150 psi H2	2	Samples actuated for 1073 h in H_2 at ambient at 40 Hz, 1000 V. **Hydrogen actuation OK.**
Exposed in Ambient H_2	06-5018 06-5021	150 psi H2	2	Samples exposed for 1073 h in H_2 at ambient. Actuated at beginning and end at 40 Hz, 1000 V. **Hydrogen exposure OK.**

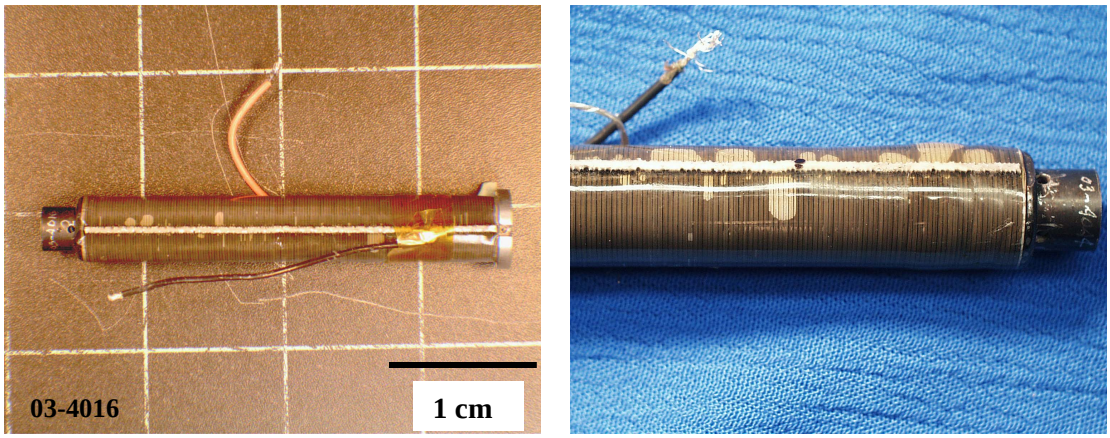

Figure 4. Large KCI actuators after failure in high-pressure hydrogen tests. Optical microscopy reveals the most obvious change after testing, which is the formation of the delamination regions or bubbles beneath the outer epoxy layer on the actuators.

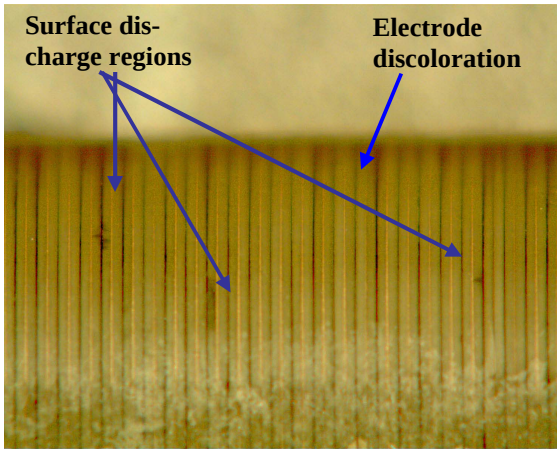

Figure 5. Actuator 03-4016 after high-pressure H_2 testing at 100°C and failure at 350 hours. Apparent surface discharge regions are indicated, as well as copper electrode discoloration. The bright copper electrodes apparently darkened during this testing.

charges at one of these regions. Also, the bright copper electrodes darkened during this testing, and KCI identified these as the negative electrodes that had changed color while the positive electrodes remained bright and shiny. Further tests are required to identify this darkening process and apparent chemical change at the negative electrodes.

Actuator 03-4044 was sectioned at PNNL and examined at higher-magnification optical imaging and with SEM. Figure 6 shows 03-4044 after 580 h in high-pressure hydrogen at 100°C. Similar degradation signatures can also be observed on the surface. In addition to these degradation signatures, it was observed that the epoxy coating had severely cracked and delaminated in large regions in the inner bore of the actuator. Figure 7 shows the sectioned and polished actuator after longitudinal sectioning. Epoxy cracking and delaminations are visible, as well as the copper electrode discoloration; the latter shows through on the epoxy inner surfaces as a dark line, suggesting that it may be an electrode-epoxy interaction.

The SEM analysis conducted to date has revealed more than these tests and has confirmed that the electrode materials are nearly pure copper, that the solder on the electrode bus was Pb-Sn solder, and that the piezoelectric ceramic is indeed a Pb-Zr-Ti-O (PZT) ceramic. SEM also revealed that some

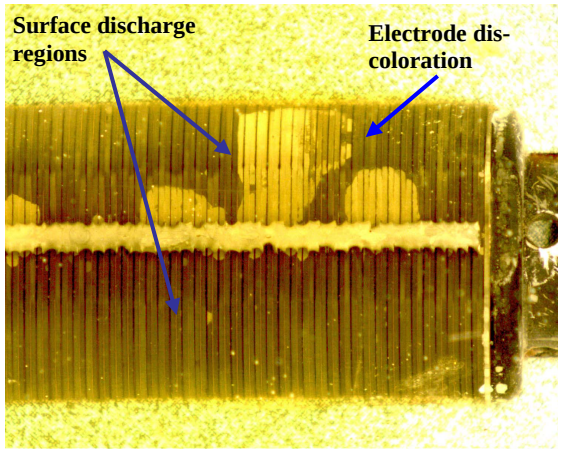

Figure 6. High-magnification optical photo of 03-4044 prior to sectioning. Large delaminations, electrode discoloration, and surface discharge regions are visible.

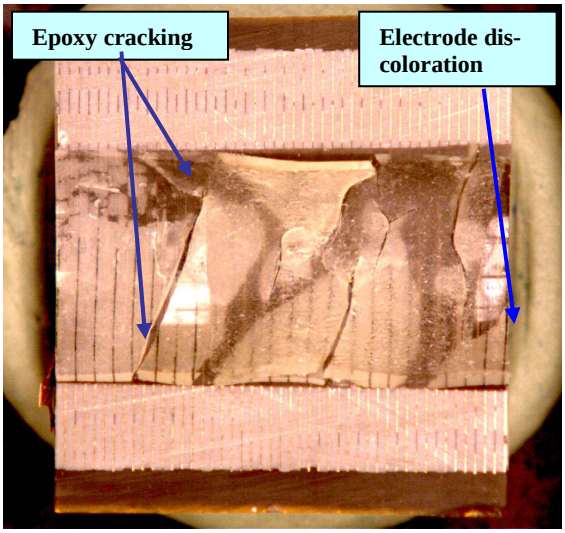

Figure 7. Optical microscopy of polished section of 03-4044 showing extensive epoxy cracking in inner core and electrode discoloration marks on epoxy inner surface.

cracking and etching of the PZT grains structure has occurred during operation, as shown in Figure 8, but this has no known role in a specific degradation mechanism yet.

Summary of Piezoelectric Testing and Analysis

Two large KCI actuators were tested in high-pressure hydrogen at 100°C, and both failed during operation before 1000 h. The most likely failure cause was shown to be surface discharges or arcing between electrodes, but the root cause of that has not yet been established. Thus a new test matrix was devised to probe individual variables, such as pressure, temperature, and environment or hydrogen. Several small piezoelectric actuators were procured, and testing has begun with the actuators passing the 1000-h test mark for ambient N_2, 100°C N_2, and low-pressure H_2 at ambient temperature. These tests have not yet been analyzed. Future tests will include the more aggressive hydrogen pressure and temperature testing as was done before. The failed actuators also exhibited delamination bubbles in the epoxy coating and negative electrode discoloration that remains to be explained. A new technique for hydrogen analysis in materials, nuclear reaction analysis, was explored and demonstrated to be capable of sensitive hydrogen measurement on one of the large KCI actuators. The amount of hydrogen was quantified, but more study is required to demonstrate that this amount of hydrogen is significant or is degrading to the piezoelectric materials.

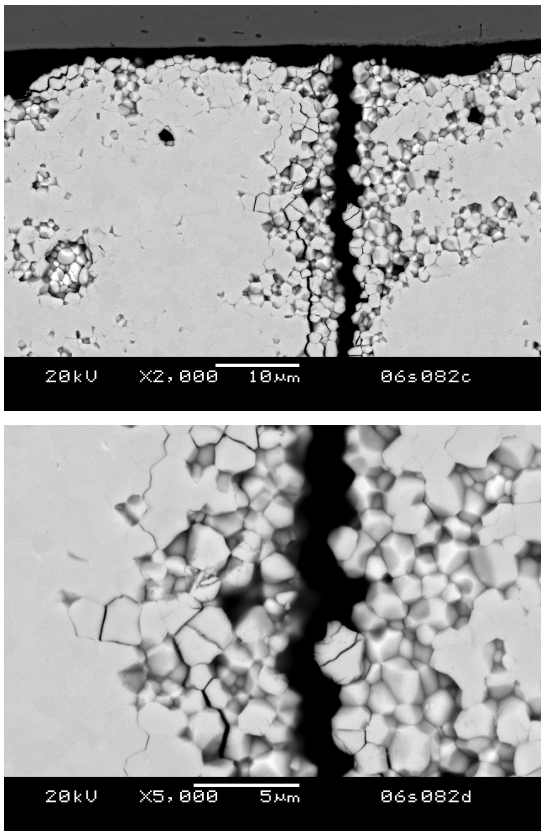

Figure 8. SEM photos of polished sections of PZT region of actuator 03-4044 showing transverse cracking likely due to specimen preparation and grain etching. The role of hydrogen in this is not clear at present.

Hydrogen Effects on Dielectric Ceramics

Dielectric ceramics, such as $BaTiO_3$ and $Pb(Zr,Ti)O_3$ (PZT), have permanent dipole moments because of their slightly asymmetric crystal structures (Figure 9). PZT is widely used as a piezoelectric ceramic. It either generates a small electric field upon being distorted or distorts as a result of an applied electric field. The structure is such that, when viewed along a certain crystallographic direction, it is a distorted cubic structure, with the smaller tita-

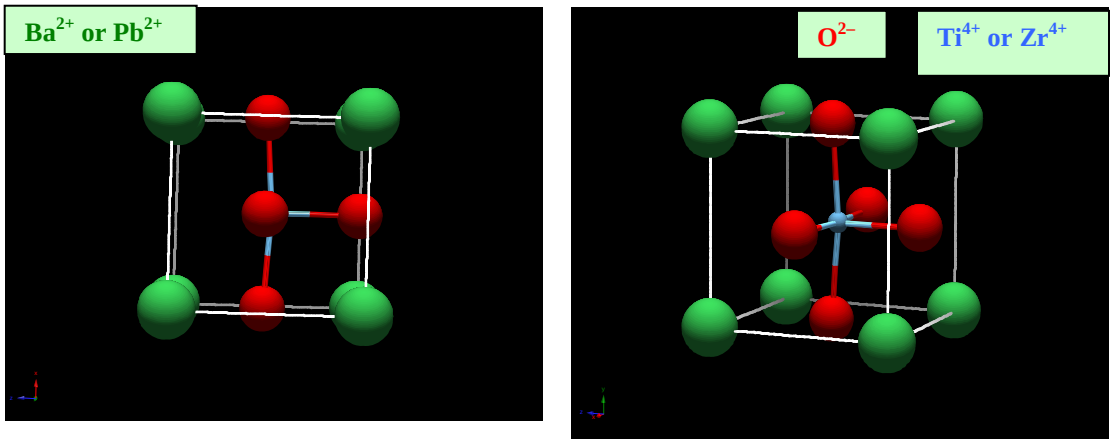

Figure 9. Structure of $BaTIO_3$ showing atomic positions and distorted lattice.

nium or zirconium atoms in a distorted octahedral interstitial site. This gives rise to the electric dipole, and both $BaTiO_3$ and PZT are ferroelectrics.

Hydrogen degradation of PZT was first noticed during forming of gas anneals—which contain hydrogen (4% H_2, balance N_2)—because the desired polarization disappeared after annealing in hydrogen. This was initially attributed to the formation of atomic hydrogen by the platinum electrodes and degradation of the Pt/PZT interface, and some studies showed that damage was less with gold or silver electrodes, which do not catalyze the $H_2 = 2H$ reaction as effectively as does Pt.

However, other studies suggest that the damage is due to diffusion of atomic hydrogen into the PZT crystal and the formation of OH^- (hydroxyl) ions, which effectively kills the polarization by redistributing the electric field in the PZT crystal. Leakage current increases, polarization decreases, and resistivity decreases (conductivity increases). Hydrogen can donate an electron to the crystal by becoming H^+ and reacting with the O^{2-} to form OH^- groups in the crystal. Anneals in oxygen can reverse this degradation. This type of damage can also occur in the presence of water or water vapor as a result of electrolysis of water near the electrodes due to the high voltages applied to these devices. The liberated hydrogen can diffuse into the PZT and cause degradation.

The effects are worse at elevated temperatures, likely because of the more rapid diffusion and reaction of hydrogen with the PZT crystal. For example, 400°C anneals in hydrogen are much worse than 100°C anneals. Finally, hydrogen embrittles PZT and can cause spontaneous cracking.

Suggested Hydrogen Degradation Mitigation

- The PZT-electrode data suggest that gold, iridium, or indium electrodes can be explored for increased hydrogen reliability. The dissociation of H_2 into atomic hydrogen appears to be a necessary step for damage to occur, and platinum- or palladium-based electrodes allow this step to occur more easily.
- At 100°C the degradation due to hydrogen diffusion into the lattice is relatively slow. High pressures obviously work against this and may be a cause of degradation at 100°C that is difficult to prevent. A permeation barrier might be helpful in these circumstances. If the epoxy is having some benefit, then this might be a weak spot in the design since epoxy failures allow hydrogen ingress into the crystal.
- Some simple electronic measurements are in order to look for changes in resistivity and polarization in the bulk material as compared with degradation occurring at the electrode-PZT interface.
- We might observe changes in lifetime (tending toward longer life) at lower temperatures that would suggest that diffusion into the bulk material is occurring.

Friction and Wear Testing

The friction and wear characteristics of metallic materials depend upon several factors, including material conditioning, environment, lubrication, and in the case of many materials, the growth of surface oxide films. Within a hydrogen service environment, which by definition is chemically reducing so that

the loss of the surface oxide by wear will result in bare surface contact, the result is an increase in friction and wear. Additionally, because of the very low density of hydrogen that powers an internal combustion engine, larger volumes of fuel must be injected per engine stroke; and of the major internal combustion fuel choices, hydrogen has the least lubricity.

Candidate needle-nozzle materials are listed in Table 3, along with a description of their material compositions and processing. Also included in Table 3 are samples we have exposed to hydrogen that will be used in our studies of hydrogen diffusion into metals. A few of these samples are to be used to better understand the diffusion mechanisms involved; they will not be tested using reciprocating friction.

Friction and wear tests were carried out on Christopher Tool (Ohio, US) and DUAP (Switzerland) needle-nozzle materials, as-received (unexposed to hydrogen) and exposed (1000 h) to hydrogen. Test were conducted using a pin-on-flat reciprocating sliding configuration under 1-N normal load and 5-Hz oscillation frequency with 4.3-mm stroke for 20 min, 50 s (53.75 m sliding distance) in both ambient (air) and inert (argon) environments. Table 4 describes the test setup and the data collected to date on the sample hardness effects due to hydrogen exposure. It is very interesting to note that even this limited amount of data indicates that the hardness of the DUAP material does increase by 0.32–0.58 Hv, depending upon the indenter depth, as a function of exposure at 1000 h. Additional data are being generated on these samples and will be reported in subsequent reports.

Reciprocating pin-on-flat tests of both hydrogen exposed and unexposed samples have begun in conjunction with the High Temperature Materials Laboratory at Oak Ridge National Laboratory (ORNL) (Peter Blau's group). The pin-on-flat testing was run at 5 Hz with a 1-N load on the pin, a 4.3-mm stroke (as agreed upon with Westport Innovations) at 0.043 m/s. A synopsis of the testing to date is provided in Table 5.

At this stage of the testing, it is too early to draw conclusions, as the body of data is still being developed. However, trends have been observed, and based on the data presented in Table 5, we can identify the following observations:

1. The hardness of H_2-exposed DUAP material appears to be slightly higher than that of the non-exposed ones. Microindentation will be applied to other materials to confirm the trend.
2. The material effect is the biggest factor. CT clearly outperformed DUAP with significantly lower friction and wear. The wear on CT was minimum and not measurable by profilometry.
3. Hydrogen exposure does have effects on frictional behavior. It seemed beneficial (unexpected) for both CT and DUAP in argon but had mixed influence in air.
4. Environment did play an important role. Unexpectedly, argon appeared to be beneficial in most cases, especially for H_2-exposed samples. Lower friction coefficient was achieved in argon than in air for hydrogen-exposed samples. Different wear modes were observed, oxidized-wear dominating in air and abrasive-wear dominating in argon. The wear volumes produced in argon were significantly less (by 40–80%) than those in air for DUAP.
5. The small pin tip radius seemed to accelerate the test with a quicker friction transition.

Future Friction and Wear Test Direction

In future activities, we will complete the friction and wear testing of the Christopher Tool, DUAP, and standard test samples in conjunction with ORNL. Currently we are awaiting funds to complete these tests.

In addition, we have completed the in-situ test apparatus for hydrogen (see next section) and will employ it in the next experimental series.

- Complete current test matrix of exposed samples.
- Conduct matrix of coated samples in the following year with the input from Ford Motor Company, Westport, and Argonne National Laboratory.
- Conduct in-situ tests next year in hydrogen environment.
- Conduct in-situ sliding impact wear tests in hydrogen environment.

Table 3. Composition of test samples and processing details

Material	Manufacturer	Composition	Certified (Yes/No)	Heat treatment	Case hardened	Coating
Nickel	Metal Samples Co., AL, USA	99.9% Ni	Yes			
Iron	Metal Samples Co., AL, USA	99.7 Fe	Yes			
M2 steel	Metal Samples Co., AL, USA	4%Cr 2%V 5%Mo 6%W	Yes			
H13 steel	Metal Samples Co., AL, USA	5%Cr 1.3%Mo 1.1%V	Yes			
CT nozzle	Christopher Tool, Ohio, USA	AISI H13 (5%Cr 1.3%Mo 1.1%V)	No—from manufacturer	Through hardened Rc 65-70		
CT needle	Christopher Tool, Ohio, USA	AISI M2 (4%Cr 2%V 5%Mo 6%W)	No—from manufacturer	Through hardened Rc 60-65		WCC Rc 66-72
DUAP nozzle	DUAP Switzerland	DIN 1.5920 (18%Cr Ni%8)	No—from manufacturer		Hardened Rc 60-64	
DUAP needle	DUAP Switzerland	DIN 1.3343 (5%Mo 6%W)	No—from manufacturer		Hardened Rc 60-64	
DUAP needle	DUAP Switzerland	DIN 1.3343 (5%Mo 6%W)	No—from manufacturer		Hardened Rc 60-64	Ion-bonded A-DLC-HP

Table 4. Candidate materials and test matrix—in process

Pin	Disk	Exposure to hydrogen	Test environment	Contact stress	Hv (avg.) load (g-f)/Hv
DUAP needle material	DUAP nozzle material	None	Argon Air	Low,[a] high[b]	**DUAP nozzle** 200/6.82 100/7.26 50/7.00
DUAP needle material	DUAP nozzle material	1000 hours	Argon Air	Low,[a] high[a]	**DUAP nozzle** 200/7.40 100/7.72 50/7.32
CT needle	CT nozzle	None	Argon Air	Low,[a] high[b]	**CT nozzle** 200/ll.52 100/10.89 50/12.24
CT needle	CT nozzle	1000 hours	Argon Air	Low,[a] high[b]	In process
M2 steel	H13 steel	None	Argon	Low,[a] high[b]	In process
M2 steel	H13 steel	1000 hours	Argon	Low,[a] high[b]	In process

[a]Pin tip radius 25.4 mm.
[b]Pin tip radius 3.175 mm.

Table 5. Test results, to date, of experiments conducted on CT and DUAP sample materials

Material	H2	Storage	Environ.	Tip radius (mm)	Initial coef. friction (COF)	Final coef. friction (COF)	COF<0.5 duration (seconds)	Wear rate (mm^3/N-m)	Wear vol. ($x10^{-3}$ mm^3)	Notes and observations
CT	0	RT	Air	25.4	0.16	0.20	1250	n/m*	n/m*	
CT	0	RT	Air	25.4	0.19	0.41	1250	n/m*	n/m*	
CT	0	RT	Air	3.175	0.21	0.51	710	n/m*	n/m*	
CT	0	RT	Argon	25.4	0.17	0.07	1250	n/m*	n/m*	
CT	0	RT	Argon	3.175	0.12	0.82	1035	n/m*	n/m*	
CT	0	RT	Argon	3.175	0.19	0.96	320	n/m*	n/m*	
CT-1000	1000	40C ->dry ice	Air	25.4	0.16	0.33	1250	n/m*	n/m*	
CT-1000	1000	40C ->dry ice	Air	3.175	0.14	0.34	1250	n/m*	n/m*	
CT-1000	1000	40C ->dry ice	Argon	25.4	0.15	0.11	1250	n/m*	n/m*	
CT-1000	1000	40C ->dry ice	Argon	25.4	0.08	0.10	1250	n/m*	n/m*	
CT-1000	1000	40C ->dry ice	Argon	3.175	0.15	0.11	1250	n/m*	n/m*	
DUAP	0	RT	Air	25.4	0.21	0.82	15	2.85E–05	1.53	Brown debris
DUAP	0	RT	Air	3.175	0.28	0.72	10	5.68E–05	3.06	Brown debris
DUAP	0	RT	Argon	25.4	0.23	1.16	170	1.62E–05	0.87	Black debris
DUAP	0	RT	Argon	3.175	0.29	1.04	35	1.06E–05	0.57	Black debris
DUAP-1000	1000	40C ->dry ice	Air	25.4	0.38	1.07	5	3.49E–05	1.88	Brown debris
DUAP-1000	1000	40C ->dry ice	Air	3.175	0.38	1.03	5	6.65E–05	3.58	Brown debris
DUAP-100	1000	40C ->dry ice	Argon	25.4	0.25	0.96	55	1.49E–05	0.80	Black debris
DUAP-1000	1000	40C ->dry ice	Argon	3.175	0.12	0.96	55	1.79E–05	0.96	Black debris

*n/m—not a measurable amount of material removed.

In-Situ Hydrogen Wear Fixture Design

This section describes a pin-on-flat wear fixture designed for testing of materials in a high-pressure hydrogen environment (Figure 10). The fixture is intended for use inside an autoclave where the specimens can be tested in a high-pressure hydrogen environment and at an elevated temperature. The fixture needs to be compatible with the test environment and fit within the space available. The fixture described in this document is the prototype of the concept and is as yet untested. Limited performance data for some of the components related to the effects of the hydrogen environment are available. Part of the initial testing will be to determine if the components are compatible with the hydrogen test environment.

Two ASTM standards exist that provided some guidance in the design of the wear fixture. Standard

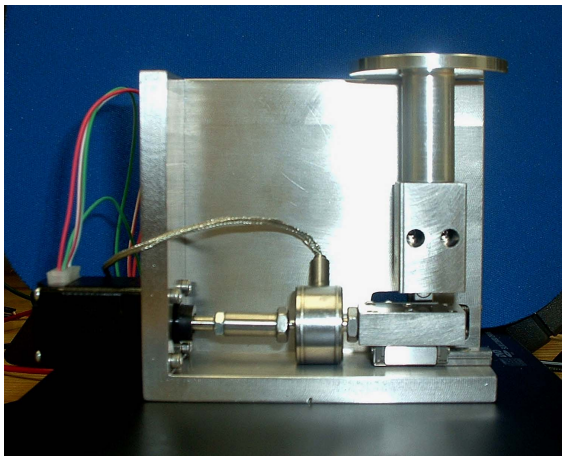

Figure 10. Picture of the in-situ tribometer setup in the lab. The next phase of testing will be in a pressurized hydrogen environment. Height of unit is ~5 in.

ASTM G99-05, "Standard Test Method for Wear Testing with a Pin-on-Disk Apparatus," and ASTM G133-05, "Standard Test Method for Linearly Reciprocating Ball-on-Flat Sliding Wear," both describe test methods somewhat similar to that required for our wear fixture. ASTM 99-05 covers a pin with a tip of known radius positioned perpendicular to a rotating disk. ASTM 99-05 does not consider reciprocating motion but rather deals with a constantly rotating disk. ASTM 133-05 covers reciprocating motion between a flat specimen and a spherically ended specimen. ASTM 133-05 has two procedures, one for unlubricated wear and one for lubricated wear. The radius of the specimen, applied normal force, stroke length, and oscillating frequency are all specified in ASTM 133-05 and the values used are not appropriate for our hydrogen wear testing. However, the general guidance provided was used. In addition, these two specifications provide accepted methods for measuring and calculating wear.

The nominal contact stresses are imposed using a combination of applied dead load and wear pin diameter. The lateral or frictional force is measured using the load cell. The motion of the flat plate is controlled using the linear stepper motor. The slotted optical switch is used to home the device whenever the power to the system is turned off. The linear stepper motor does not have an absolute encoder to keep track of its location. The optical switch will be used whenever the reference location needs to be reestablished.

All components are rated for at least 100°C. However, data are not available on using the load cell, the linear actuator, or the optical switch in a high-pressure hydrogen environment. We have not identified anything in the design of these components that would suggest problems with their use in a high-pressure or hydrogen environment. While we have no data indicating they will not work in a high-pressure hydrogen environment, we will need to test the actual hardware for an extended period of time at temperature and pressure to confirm that they will function adequately.

D. Advanced Materials Development through Computational Design for HCCI Engine Applications

Vinod K. Sikka, G. (Murali) Muralidharan, and Rick Battiste
Materials Science and Technology Division
(865)574-5112: fax: (865) 574-4357; e-mail: sikkavk@ornl.gov
Bruce G. Bunting
Engineering Science and Technology Division
(865) 946-1512; fax: (865) 946-354; e-mail: buntingbg@ornl.gov

DOE Materials Technologies Team Leader: Jerry Gibbs
(202) 586-1182; fax: (202) 586-1600; e-mail: jerry.gibbs@ee.doe.gov
ORNL Technical Advisor: David Stinton
(865) 574-4556; fax: (865) 241-0411; e-mail: stintondp@ornl.gov

Contractor: Oak Ridge National Laboratory, Oak Ridge, Tennessee
Prime Contract No.: DE-AC05-00OR22725

Objectives

- Identify and catalog the materials operating conditions in homogeneous charge compression-ignition (HCCI) engines and use computational design concepts to develop advanced materials for such applications.
- Interact with designers of HCCI engines and manufacturers of components in order to identify the components that will be affected by the harsh operating conditions resulting from the HCCI design.
- Identify the highest-priority component(s) that are critical to the implementation of the HCCI concept.

Approach

- Identify engine components, currently used materials, and current operating conditions and compare them with the expected component operating conditions for HCCI engines.
- Demonstrate the feasibility of the "materials-by-design" approach for the highest-priority item. Improve material performance for HCCI applications through computational modeling and experimental validation.

Accomplishments

- Identified high-temperature fatigue as a critical property of interest in improving the performance of valve materials and identified weight percent (or volume fraction) of γ' as a critical microstructural characteristic that needs to be optimized.
- Identified eight commercially available compositions of nickel (Ni) -based alloys as potential candidates for further study in developing correlations between microstructure and properties.
- Completed thermodynamic calculations on all seven alloys and initiated microstructural characterization and mechanical property testing.
- Through discussions with suppliers of Ni-based alloys, identified one major supplier who has expressed interest in tracking progress in the project with regard to alloy properties and interest in active collaboration in the future.

- Based on computational approach for alloy design, obtained funding for a Work-For-Others project from a major automobile manufacturer to optimize compositions of cast irons for exhaust manifold applications.

Future Direction

- Communicate with automotive companies, Diesel Cross-Cut Team, FreedomCAR, and 21st Century Truck on the progress made through computational design.
- Develop data on mechanical properties of selected Ni-based alloys and correlate microstructure with properties. This will validate the computational design concept for design of advanced Ni-based alloys.

Introduction

There has been an increasing interest in HCCI combustion in recent years because of its potential to increase engine combustion efficiency and reduce emissions. However, the use of HCCI combustion will subject the engine components to significantly higher temperatures and pressures. The temperatures for diesel engines will reach over 1600°F, and pressure may reach > 2000 psi, which is approximately four times that of the normal combustion engine. Such severe engine operating conditions will require a significant improvement in materials performance in order to take advantage of the HCCI engine concept. This project deals with identifying materials requirements for HCCI engines for automotive and truck applications and the development of advanced, yet cost-effective, materials through computational design.

"Materials-by-design" is an Oak Ridge National Laboratory (ORNL) concept that encompasses a collection of materials-related techniques including modeling, correlation, and materials modification. The premise behind materials-by-design is that mechanical properties are correlated to microstructure and phase chemistry. The phase composition and microstructure can be achieved through thermodynamic equilibrium or through non-equilibrium techniques such as quenching, rapid casting solidification, or mechanical working. These characteristics can then be correlated to desired mechanical properties through equilibrium thermodynamics or through a variety of correlation techniques. The correlations allow untested compositions or treatments to be modeled so that desired trends can be rapidly established. Small heats of targeted materials can then be processed to confirm the modeled properties and to broaden the correlation data base.

Finally, there are several techniques, such as magnetic processing or low-temperature carburizing, that can be applied to allow further modification and optimization of desired properties. Materials-by-design is ideally suited to cast materials and heavily thermally processed materials (e.g., stainless steels, Ni alloys, cast irons, alloy steels, and brazed wrought aluminum alloys), and the concept has been successfully applied in such diverse areas as high-temperature furnace components, exhaust valves, exhaust manifolds, and tube fittings. Figure 1 and Table 1 provide an outline of the materials-by-design approach and a summary of the techniques that can be applied.

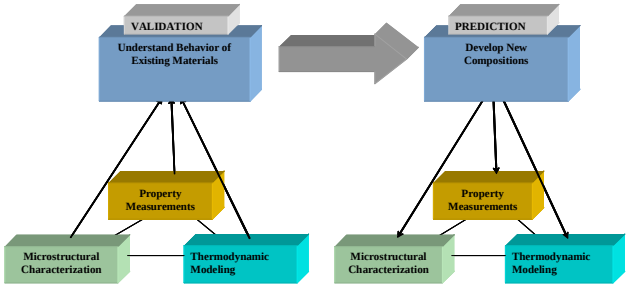

Figure 1. Overall approach for materials-by-design.

In our approach, we examined critical heavy-duty diesel engine materials and identified means to reduce their cost for acceptance in HCCI applications. This was accomplished through the following tasks:

Task 1. Identify critical material requirements for HCCI engines based on their operating conditions. This task will be accomplished through interactions with advanced engine and component designers. The interactions will include personal visits to six companies: Caterpillar, Cummins Engine, Deer, International Truck, Eaton Corp., and General Motors. Visits will be supplemented by a literature search, a review of advanced engine design studies, and follow-up discussions afterward. The key outcomes from this task will include (1) identifying

Table 1. ORNL materials by design toolbox

Modeling	Experimentation	Characterization
Thermodynamic modeling of material properties vs alloy composition	Ultra-high-gauss magnetic stabilization of alloy steels	Advanced microscopy techniques
Neural-network modeling of diverse, nonlinear materials properties and process variations	Low-temperature gas carburization of finished components	X- ray and neutron scattering
Detailed microstructure based empirical modeling	Ability to produce small quantities of materials and fabricate them into test bars for property measurements and production of prototype components by a variety of methods, including sand and die casting, extrusion, forging and rolling	Surface and bulk property measuring techniques
Non-equilibrium modeling of solidified structures		
Extrapolation of properties from simple alloy systems to complex systems using interaction parameters		

operating conditions for advanced engine concepts, with a focus on the HCCI concept; (2) identifying components most affected by these operating conditions; (3) identifying currently used materials, new requirements, and performance targets; and (4) ranking the highest-priority items for study by the materials by design approach.

Task 2. Demonstrate the feasibility of materials-by-design approach for the highest-priority item. In this task, we will identify the details of the currently used material for the highest-priority item. Specifically, we will examine material compositions, processing methods, mechanical properties, corrosion properties, and cost.

Based on the available mechanical properties data, microstructural analysis, and thermodynamic phase stability calculations, we will identify the underlying mechanism that delivers the current properties.

Task 3. Improve materials performance for HCCI application through computational modeling and experimental validation. In this task, we will use computational modeling (key basis for the material-by-design concept) to identify compositions that will deliver the desired phases for two purposes: (1) improving property performance and (2) finding alternatives to reduce cost for both current and improved performance. The outcome of the analysis will be validated through experimentation. The validation will be carried out in the following steps:

1. Prepare compositions identified based on computational design in 1-lb heats for microstructural analysis and very limited property determination; compare the results with output based on computational analysis for validation.
2. Scale up the validated composition into 20-lb to 100-lb heats and cast them into ingots for processing trials. In most cases, the material is expected to be used in the wrought condition. However, if it is to be used in the cast condition, we will save part of the ingots for analysis of as-cast properties.
3. Subject cast ingots to processing steps that are currently used by industry. Develop optimum processing and heat-treatment conditions to obtain the desired microstructure.
4. Carry out microstructural analysis and mechanical properties analysis on the material processed and heat-treated with optimum conditions.
5. Prepare autotype components for HCCI engine tests.

Extensive interaction with industrial partners will occur during all three tasks. This collaboration is expected to result in the rapid transfer of materials improvement from this project to industry for use in HCCI and other advanced engine concepts.

Results

Materials Development through Computational Design

Ni-based alloys have been identified as potential candidates for improved valve materials. There is particular interest in increasing the operating temperature of exhaust valves to about 1600°F (870°C). High temperature fatigue strength has been identified as a critical factor in determining the performance of these alloys in the valve application. An evaluation of the microstructure of various Ni-based alloys and correlation with limited information on the fatigue properties that are available show that the volume fraction of the γ' phase is likely to be a dominant factor in determining the performance of these alloys at high temperatures. Since the size of the strengthening precipitates is also critical, it is anticipated that the kinetics of coarsening this phase would also be influential in the long-term performance of the alloys in this application. Based upon discussions with various users and suppliers, a range of Ni-based alloys with potentially varying weight fractions (or volume fractions) of γ' have been identified in efforts to correlate the fatigue properties with the microstructure of the alloys. Table 2 shows a summary of these alloys and the compositions of specific heats procured for this study. IN 751 is the alloy currently used, and it has been added to the matrix as a reference.

To obtain initial information on the microstructures of these alloys at equilibrium, thermodynamic calculations have been carried out using JMatPro V4 for all the alloys shown in Table 2. Figures 2 to 9 show the phases present in the alloys as a function of temperature.

Comparison of the results of the calculations shown in Figures 4 to 9 shows that all alloys have a matrix of γ with the major strengthening phase as γ'. One or more carbide phases such as M23C6, MC, and M7C3 may also be present in different alloys. The primary difference between the microstructures of the various alloys is in the weight percent of the γ' phase at a given temperature and the highest temperature at which the γ' phase is stable in the different alloys. Table 3 shows a summary of the type and phases present at 900°C in the different alloys. The variation in γ' phase content is well illustrated in the table.

A survey of the data available on the high-temperature fatigue properties of these alloys was conducted. Results show that such data are available not for specific compositions of the alloys but for a broad range of compositions that could be associated with a particular grade. Thermodynamic calculations show that significant variations in the phase contents occur over this composition range. Thus it is not feasible to develop relationships between the microstructures of the alloys and their mechanical properties based on data available in the literature. The required high-temperature fatigue property data will be obtained as a part of the project, and equipment for testing has been assembled as outlined below.

Mechanical Property Measurement

To conduct fatigue tests on the selected Ni-based alloys**,** an existing material test system servohydraulic closed loop control material test facility has been upgraded to include high-temperature, low-cycle-fatigue testing capability for round bar type specimens. Test results will be reported next quarter.

Table 2. Compositions of various alloys selected for studying the correlation between microstructure and mechanical properties

Alloy	C	Si	Mn	Al	Co	Cr	Cu	Fe	Mo	Nb	Ni	Ta	Ti	W	Zr
X750	0.03	0.09	0.08	0.68	0.04	15.7	0.08	8.03	–	0.86	Bal	0.01	2.56	–	–
Nimonic 80A	0.08	0.1	0.06	1.44	0.05	19.6	0.03	0.53	–	–	Bal	–	2.53	–	–
IN 751	0.03	0.09	0.08	1.2	0.04	15.7	0.08	8.03	–	0.86	Bal	0.01	2.56	–	–
Nimonic 90	0.07	0.18	0.07	1.4	16.1	19.4	0.04	0.51	0.09	0.02	Bal	–	2.4	–	0.07
Waspaloy	0.03	0.03	0.03	1.28	12.5	19.3	0.02	1.56	4.2	–	Bal	–	2.97	–	0.05
Rene 41	0.06	0.01	0.01	1.6	10.6	18.4	0.01	0.2	9.9	–	Bal	–	3.2	–	–
Udimet 520	0.04	0.05	0.01	2.0	11.7	18.6	0.01	0.59	6.35	–	Bal	–	3.0		
Udimet 720	0.01	0.01	0.01	2.5	14.8	15.9	0.01	0.12	3.0	0.01	Bal	–	5.14	1.23	0.03

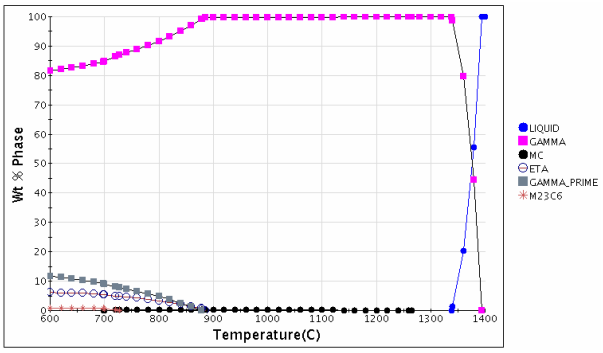

Figure 2. Phase equilibria in alloy X750.

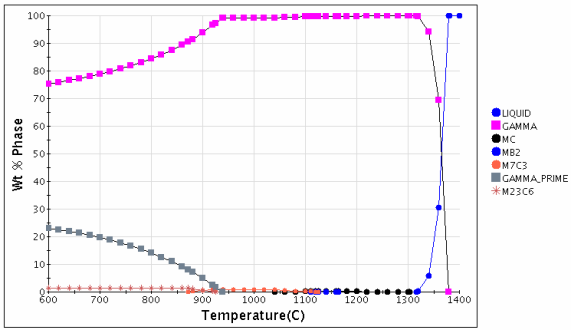

Figure 3. Phase equilibria in alloy Nimonic 80A.

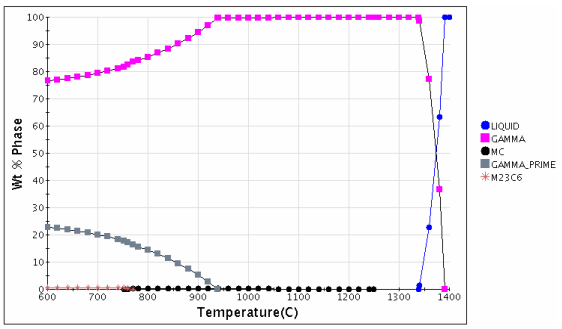

Figure 4. Phase equilibria in alloy IN751.

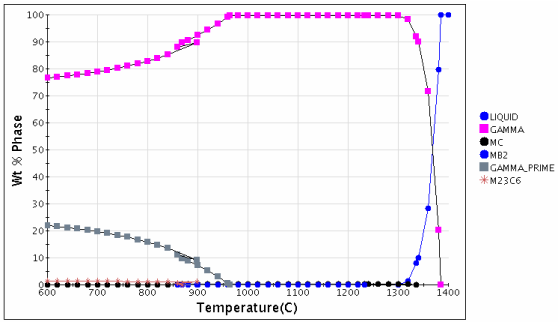

Figure 5. Phase equilibria in alloy Nimonic 90.

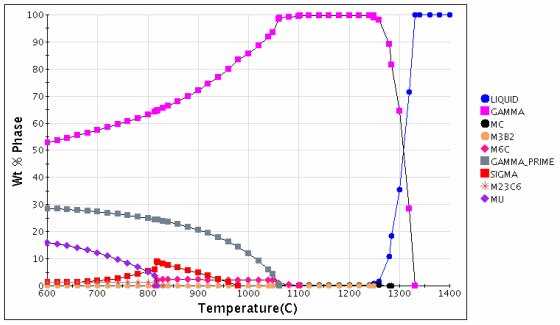

Figure 6. Phase equilibria in Waspaloy.

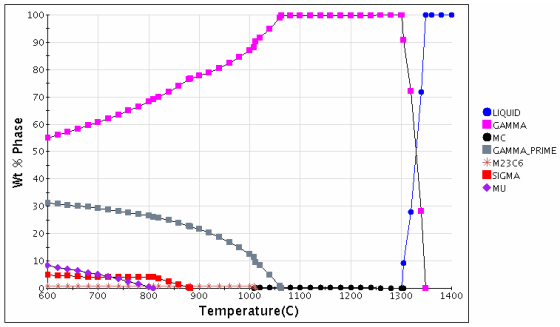

Figure 7. Phase equilibria in Rene 41.

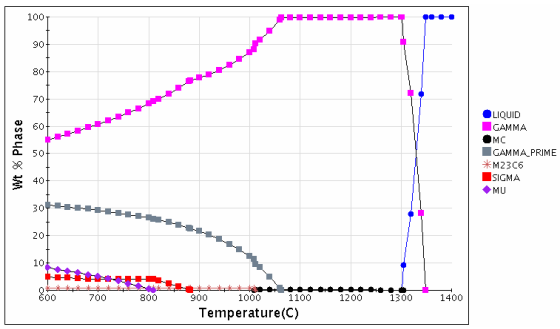

Figure 8. Phase equilibria in Udimet 520.

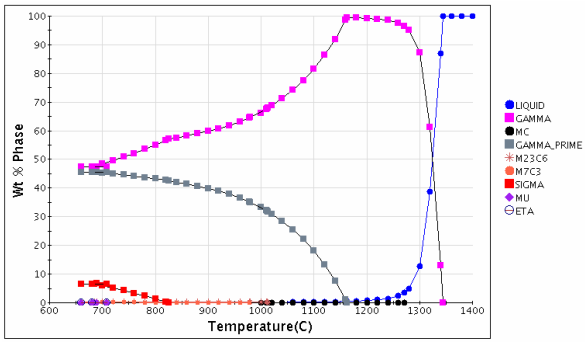

Figure 9. Phase equilibria in Udimet 720.

Table 3. Calculated major phase contents of various alloys at 900°C

Alloy	Wt % γ	Wt % γ'	Wt % carbides	Wt % other
X750	99.8	**0**	0.2	
Nimonic 80A	93.9	**5.0**	1.1	
IN 751	94.5	**5.3**	0.2	
Nimonic 90	89.8	**8.9**	1.3	–
Waspaloy	84.7	**14.7**	0.6	–
Rene 41	72.1	**20.7**	2.4	4.8
Udimet 520	77.6	**21.6**	0.8	–
Udimet 720	59.6	**40.0**	0.4	–

Conclusions

- Potential commercial Ni-based alloys that need to be evaluated for use in higher temperature exhaust valves were identified.
- Thermodynamic calculations show that the variation in the major strengthening phase spans a significant range and hence is appropriate for developing correlations between microstructure and mechanical properties.
- High-temperature fatigue data were identified as essential in the selection and/or development of Ni-based alloys for this application.

Publications/Presentations

Bruce Bunting, Govindarajan Muralidharan, V. K. Sikka, presentation at Cummins International.

Govindarajan Muralidharan, Steve Weber, Michael Pollard, and Haydn Chen, "Coarsening of Coherent Precipitates in Multi-Component Ni-Based Alloy Systems: Experiment vs Theory," a poster presentation at the Gordon Research Conference on Physical Metallurgy, July 23–28, Holderness School, Plymouth, NH.

Appendix A

Low-Cost, High-Energy-Product Permanent Magnets

Final Report

Low-Cost, High-Energy-Product Permanent Magnets

Y. S. Cha, T. M. Mulcahy, and J. R. Hull

Thermal and Electromechanics Section
Energy Technology Division
Argonne National Laboratory

Final Report
(Abbreviated)

June 2006

I. Introduction

The overall goal of DOE's FreedomCAR program is to reduce oil consumption. Hybrid electric vehicles (HEVs) provide a near-term opportunity to save energy. A major challenge for wide acceptance of HEVs is cost. It is estimated that hybrid technology may cost $4,000–6,000 more than conventional technology using an internal combustion engine. Therefore, one of the primary objectives of developing HEVs is to reduce cost. Another major objective is to reduce the weight of the vehicle, which will translate into reduced oil consumption.

A major component of the HEV is the electrical machine (traction motor) used to drive the wheels. The traction motor employs a number of permanent magnets (PMs). Sintered NdFeB PMs are used in HEVs because of their superior magnetic properties (energy product) compared with other PMs. Energy product is directly proportional to the energy stored per unit volume of the magnet; the torque produced by a PM electric motor is approximately proportional to the energy product of the PM. Increasing the energy product of the PM will proportionally increase the torque. Therefore, increasing the energy product will reduce the weight and size of the PM required to generate the same torque. Furthermore, reducing the weight and size of the PM may reduce the size of the entire motor required to generate the same torque. This will further reduce the overall weight of the motor and increase the mileage of the HEV.

An important step in the fabrication of the highest-energy-product PMs is the unidirectional magnetic alignment of the 3-μm to 5-μm single-crystal grains while the powder is pressed into compacts for sintering. The PM's remnant magnetism is proportional to cos (θ), where θ is the angle between each grain's easy magnetic axis and the desired direction of alignment. For perfect alignment, $\theta = 0$ for each grain, but this ideal situation is never realized. Primarily, grain alignment is limited by mechanical friction between grains and the self-fields generated by the powder volume in the die. To align the grains in the press direction, today's PM producers use 1- to 2-Tesla pulsed electromagnets in axial-die pressing. Axial-die pressing dominates anisotropic magnet production because it is the most cost-effective method and best suited for making near-final-shape magnets—a current goal of industry. But alignment is far from complete, even when organic lubricants are added to the magnet powder to promote rotation of the grains. In particular, the use of lubricants is limited because they oxidize the free neodymium (Nd), which is present in the powder as a sintering aid and for production of magnetic coercivity. Addition of more paramagnetic Nd would reduce the percentage of hard magnetic material and therefore the remnant magnetization of the PM. Just as important, too much lubricant weakens the strength of the compact. Press loads are minimized so that they just hold the compacts together for handling. Larger loads increase the partial buckling of the columns of grains and their misalignment.

Expectations are that the higher alignment fields (higher than the 2-Tesla field that can be produced by a conventional electromagnet) and the greater torque on each grain will improve and maintain grain alignment before and during pressing and thus produce better PMs. To generate a magnetic field higher than 2 Tesla, a superconducting magnet (SCM) is usually employed, which requires a cryogenic system to keep the superconductor coil below its critical temperature.

The other major cause of grain misalignment is associated with the magnetization of finite-size volumes of powder. When the magnetic powder in the die is subject to a uniform external alignment field, a non-uniform self-field occurs spontaneously. Since the magnetic axes of the grains align along the combined field lines, unidirectional alignment of the grains is distorted. Unfortunately, the self-field and distortion are greatest for compacts with the smaller length-to-diameter (L/D) ratios that are typical of near-final-shape magnets. However, the higher alignment fields of SCMs are expected to improve the alignment of near-final-shape magnets by overwhelming the self-field distortions. Clearly, the potential exists for improved grain alignment using an SCM.

In FY 1999, a project was initiated to demonstrate a new PM fabrication technology, in collaboration with industry, using an SCM that is capable of producing a much higher magnetic field than a conventional electromagnet. The idea is to increase the energy product of the PM by using the stronger alignment field generated by the SCM during compact pressing. The goal of the project is to develop a process that will

increase the energy product significantly and lower the cost of producing these PMs by fabricating near-final-shape magnets. An economic study of the new superconducting technology was also carried out following a suggestion made during the annual review meeting for FY 2003. All the results are documented in this report.

It should be noted that besides traction motors in HEVs, PMs are used in many other places in an automobile (Figure 1). In addition to automobile applications, these improved magnets would also find wide industrial and military application.

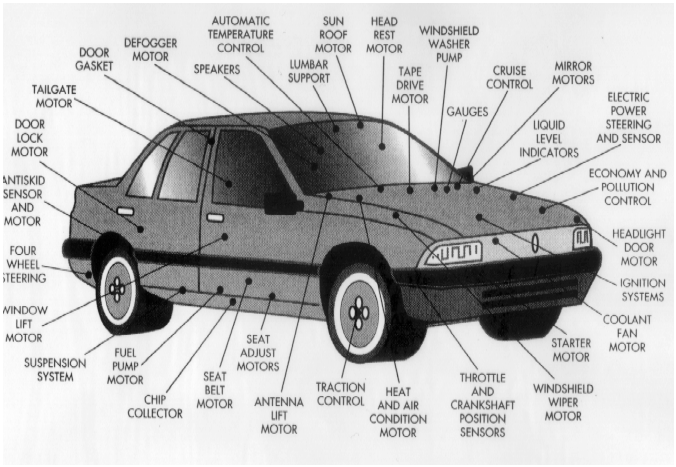

Figure 1. Potential applications of PMs in an automobile.

Energy Product and Coercive Field

Energy product, BH, is defined as the product of the magnetic flux density B and the magnetic field strength H for a given point on the demagnetization curve (the second quadrant of the B-H curve) of a PM. It is an important property of the PM because a given volume of magnetic material will produce the highest field in a given air space when the energy product is at a maximum.[1] Energy product is proportional to the energy stored per unit volume of the magnet. A magnet should be shaped for the most efficient use in such a way that its operating point is close to the $(BH)_{max}$ point. The torque produced by a PM electric motor is approximately proportional to the energy product of the PM.

A typical value of the energy product for commercially available sintered NdFeB magnet is approximately 40 MGOe (mega gauss-oersted) or 320 kJ/m^3. The theoretical limit of the energy product is 64 MGOe (512 kJ/m^3) based on 100% perfect alignment and 100% volume fraction of the $Nd_2Fe_{14}B$ hard phase. Besides the Curie temperature and the energy product, the remanence (B_r) and the coercive field (H_c) are important properties of a PM. The maximum energy product $(BH)_{max}$ is proportional to $(B_r)^2$. The coercive field determines the magnetic hardness against external magnetic fields, which is important for many applications. Figure 2 shows the required magnetic properties of PMs for various applications. Typical performance requirements for linear drive motors are $(BH)_{max}$ = 40 MGOe (320 kJ/m^3) and H_c = 2 Tesla (1.6 MA/m). It is the objective of this study to increase the energy product by using stronger magnetic alignment fields generated by the SCM while maintaining the same coercive field (by raising the operating point vertically in Figure 2). So far, NdFeB magnets show the highest value of remanence B_r and energy product $(BH)_{max}$, and samarium-cobalt magnets exhibit the highest coercive fields, H_c. The results shown in Figure 2 indicate that as the energy product increases, the coercive field decreases. This is mainly because the

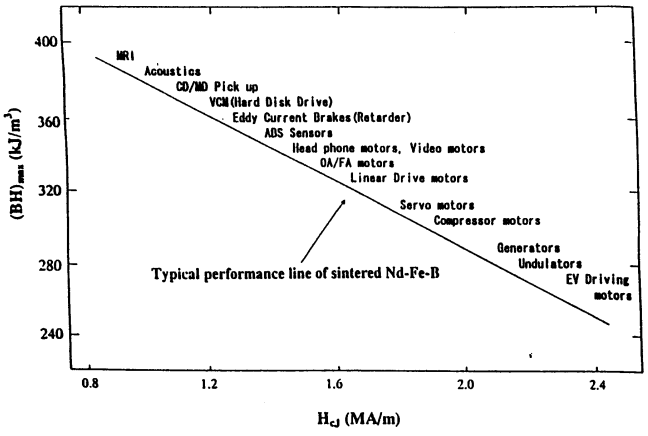

Figure 2. Energy product vs coercive field for various applications.

remanence and energy product increase with decreasing Nd content, whereas the coercive field increases with increasing Nd content.

Typical Process for Manufacturing NdFeB PMs

Figure 3 is a diagram of the typical manufacturing process for sintered NdFeB PMs.

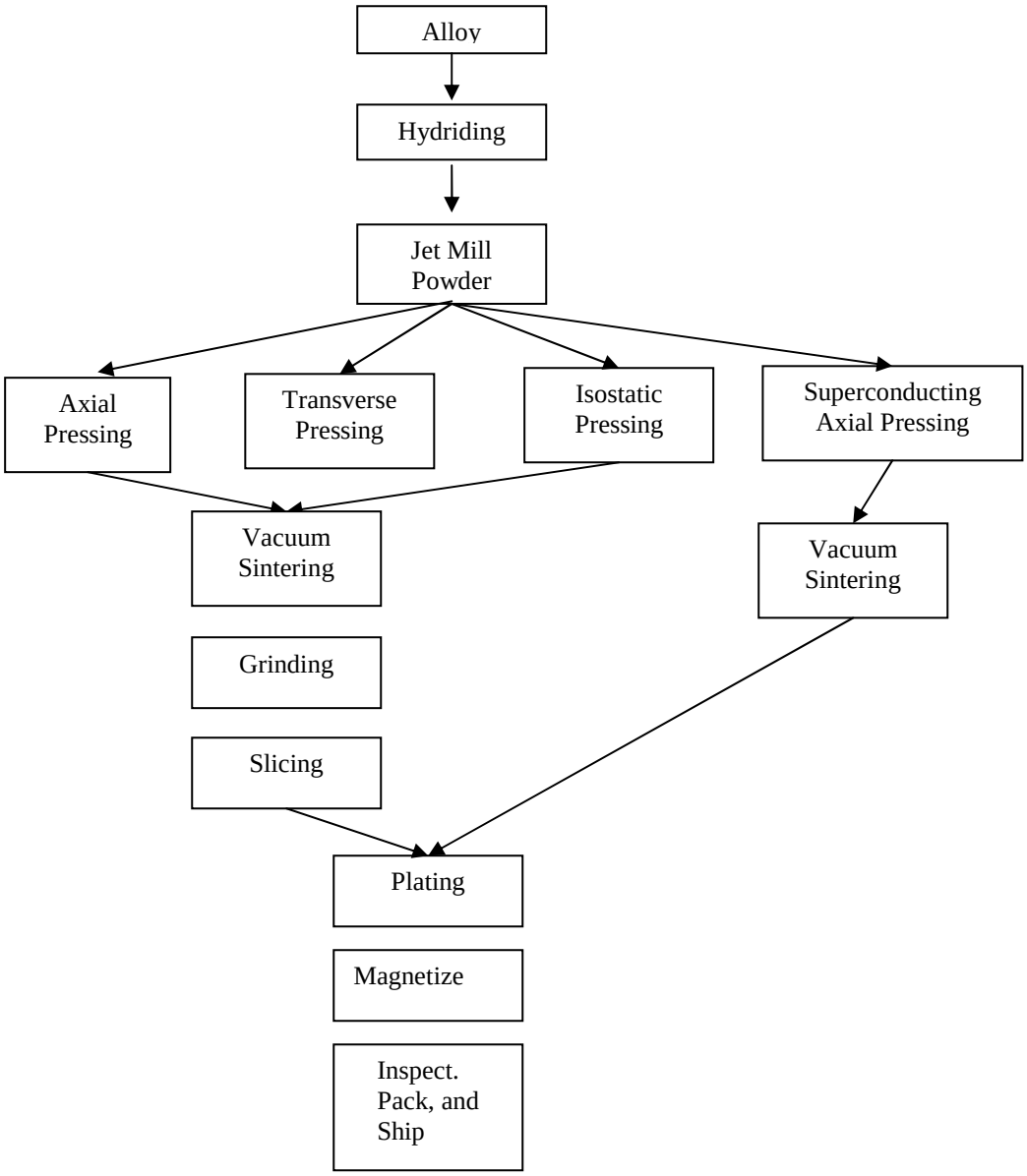

Figure 3. Typical NdFeB magnet manufacturing process.

Raw materials and initial powder processing

Most manufacturers begin with NdFeB alloy purchased from suppliers such as Santoku. The large "chunk"-size alloy is then processed using jaw crushers or hydrogen decrepitating techniques to reduce the particle size before final size reduction in jet mills or attritor mills. During these stages, other rare earth elements, such as dysprosium and praseodymium, are added to enhance particular characteristics of the final magnets. The final size of the grains is made smaller than a single crystal so that each grain can be orientated and anisotropic PMs can be produced. They are capable of achieving near theoretical maximum energy products.

Magnequench UG, Inc., the PM manufacturer, uses a different approach. It melts the alloy and then allows for rapid solidification using spinning chill plates. This rapid solidification produces the melt-spun amorphous ribbon used in the remainder of the Magnequench process. The grain size is smaller than can be achieved by jet milling, but the particles are inherently formed of multi-crystals and are best for producing isotropic PMs with lower energy products.

Pressing

Currently, four pressing techniques are used in the production of NdFeB magnets: axial, transverse, isostatic, and rubber isostatic. In all instances, the ratio between the compact before pressing and the compact after pressing is typically 3 to 1. That is, to press a piece 1 in. long in the press direction, the cavity is typically filled to a depth of 3 in. Also, the alignment field—produced by an air-core solenoid around the die cavity—is less than 3 Tesla. A high, pulsed-current rectifier energizes the solenoid.

1. In axial pressing, the alignment coil surrounds the die cavity and produces an alignment field parallel to the direction of pressing. This method has the least degree of particle alignment and produces the lowest-energy magnets compared with other methods. However, it is the least expensive of all the processes.
2. In transverse pressing, the alignment coils are placed on both sides of the die cavity and produce an alignment field perpendicular to the direction of pressing. This method has an improved degree of particle alignment and yields magnets with approximately 10% improved properties.
3. In isostatic pressing, the powder is placed in a molded rubber boot, which is then sealed from the outside environment. The boot is then placed in an air core solenoid and magnetized with one or more pulses. The boot with the aligned compact is placed in a large pressure vessel and compacted with equal high pressure in all directions. This method produces the greatest degree of particle alignment and the highest magnetic properties. Typically, there is another 10% improvement over the transverse pressing method.
4. In the rubber (pseudo) isostatic pressing technique developed by M. Sagawa and others,[2] the objective is to develop a powder compaction technique for producing green compacts with improved orientation. In this process, a rubber mold with a cavity for the powder is inserted into the die. The mold is then pressed by the upper and lower punches of the press. Using a pulsed field of up to 3 to 4 Tesla, the intent is to achieve isostatic alignment with axial die pressing. Multistation presses are used for filling, pressing, ejecting, and cleaning of the parts. The powder-filled mold must be transferred from station to station.

Sintering

After pressing, the magnet compact is sintered and heat-treated in a vacuum furnace. The sintering cycle is used to establish the remanence, B_r, and the heat treatment cycle establishes the coercivity, H_c, of the magnet.

Grinding and/or slicing

After sintering and heat treatment, grinding and/or slicing operations are usually required to produce the final form and dimensional tolerances required of the finished magnet. With axial pressing, it is possible to have only the pole faces ground to final tolerance so long as the other dimensions can be allowed tolerances of ± 0.015 to 0.030 in. The axial press system using an SCM proposed by Argonne National Laboratory (ANL) is expected to be able to produce a near-final-shape magnet and thus eliminate some of the grinding and slicing processes, as shown in Figure 3.

II. Superconducting Magnet

Conventional electromagnets can produce a continuous maximum magnetic field of up to 2 Tesla. To increase the field beyond 2 Tesla, SCMs are usually employed. Although SCMs are not yet widely used in industry, many laboratories in the United States and elsewhere in the world routinely operate SCMs for various scientific experiments. Many hospitals operate and maintain SCMs for their magnetic resonance imaging facilities, and SCMs are used commercially for magnetic separation (for example, large-scale clay separation).

Based on cost and budget constraints, it was decided to employ a liquid-helium-cooled, 9-Tesla SCM with a 3-in. room-temperature bore. An SCM was purchased from Cryomagnetics, Inc. (shown in Figure 4). This device has a horizontal 7.6-cm-diameter warm bore and is similar to other Cryomagnetics designs. The length of the bore tube is 76.2 cm. The magnitude of the steady field in the bore of the SCM can be continuously varied up to 9 Tesla. The powder can be aligned in a field that is uniform within 5%, over a volume that is large enough to press 2.54-cm-diameter cylindrical PMs that are over 10 cm long. SCM cooling was achieved with only liquid helium and superinsulation.

A cryo-cooler and magnetic shielding for the SCM were not included, because these additions would have more than doubled the initial cost. Both additions would be needed for acceptance into factory operation. In retrospect, the SCM should have been shielded for laboratory use. The laboratory was large enough to isolate the far field and satisfy all environmental, health, and safety issues; but the cost of shielding nearby computer monitors, which are sensitive to the milliTesla level, nearly equaled the cost of initially shielding the SCM.

Superconducting solenoids with much higher rates are available at additional cost. In commercial operation with a reciprocating die, the field should remain constant and no ramping should be required. In retrospect, heating coils should have been included to intentionally quench the solenoid. After several cycles, remnant fields of 5 to 10 milliTesla, with sharp axial gradients, were present at each end of the SCM. The supercurrents circulating around the diameters of the wires that were responsible for remnant fields can be removed only by quenching. During operation at high fields, the remnant fields were not a concern. But part of the proof-of-concept testing included the removal of loose magnet powder from the de-energized SCM bore. Custom means of shielding these specimens had to be designed and used.

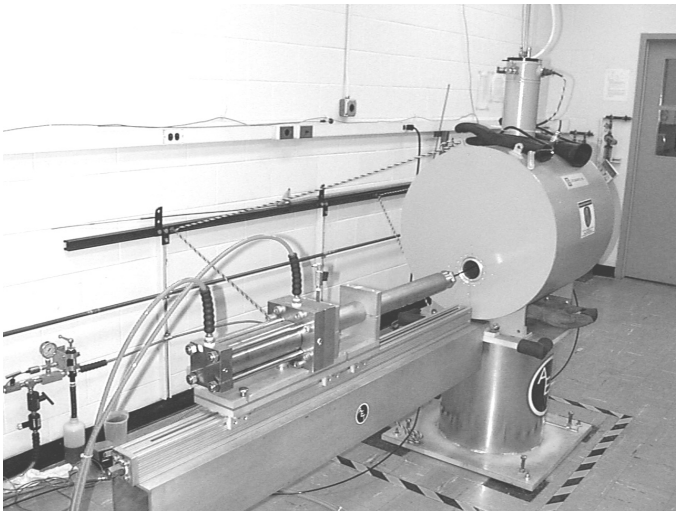

Figure 4. Photograph of the liquid-helium-cooled SCM used to make compacts under strong alignment field at Argonne National Laboratory.

III. Die and Punch Set

A 5/8-in. axial-die and punch set was designed in consultation with Magnequench and with Bronson and Bratton, Inc., the tooling fabricator. The set was made using very low-magnetic-permeability material (μ_r <1.002), which will not affect significantly the uniformity of the SCM's magnetic field or the alignment of the magnet powder. Still, when it was operating at 8 Tesla, a force of 136 N was required to extract the empty die/punch set from the SCM. The die insert and the punches were made of nickel carbide, while the die case was made of Inconel 718. Tight diametrical clearances (<0.025 mm) were required to maintain alignment of this simple die and punch set. The tooling was polished to mirror finishes, and very light coatings of stearic acid lubricants were used to ensure "floating die" operation. Clearly, tool steel with carbide tips would be difficult to use in an SCM's reciprocating press.

IV. Hydraulic Press System and Operation

To achieve automated operation, the design concept chosen was to reciprocate the press into and out of the active SCM. A similar concept has been used with superconducting solenoids in the clay separation industry.[3] An unorthodox press-in-tube device for axial die-pressing in a batch (manual) mode was designed and built by Ability Engineering Technology, Inc. This device met the magnetic and geometric constraints created by the SCM.

The press tube and ram are made from materials of very low relative magnetic permeability (<1.002). The hydraulic cylinder was custom made by Atlas Cylinders, Inc., from stainless steel with a low relative permeability (< 1.01). Electromagnetic code calculations were made to determine the magnetic field of the SCM and the forces on the powder and compacts for design of the SCM and its supports. The length of the press tube was chosen to enable access to the SCM centered 38 cm within its helium dewar and to locate the more magnetic hydraulic cylinder in the far field of the SCM, where the field gradient is weak. Also, the press tube could be rotated, which allowed die/punch set insertion in an even weaker field. The insertion mechanism and press tube were sized to withstand the magnetic forces and behave essentially as rigid bodies.

V. NdFeB Powder and the Glove Box

The NdFeB powder was purchased from our industry collaborator, Magnequench. The powder (Grade A jet-milled T3AJ) is identical to the production-grade powder used by Magnequench to manufacture its commercial PMs. Powder formulations are proprietary information. The particle size ranged from 3 to 5 microns. Because the magnetic properties of the PM are very sensitive to the oxygen content of the powder, it must be handled in a low-oxygen environment (either in a vacuum or in an inert gas) before sintering. This is because the rare earth element, such as Nd, is easily oxidizable. The powder is usually delivered in a vacuum-packed container to prevent oxidation. It is stored in a glove box with low oxygen content as soon as the vacuum-packed container is opened. It is recommended by the powder supplier that the oxygen content be less than 300 ppm in order not to degrade the magnetic properties of the PM. The oxygen content inside the glove box is usually maintained below 200 ppm by purging inert nitrogen gas, and the oxygen content is monitored continuously by an oxygen meter. Powder filling of the die before alignment and compact ejection from the die after alignment in the SCM are performed in the glove box. Compacts were sent to Magnequench for heat treatment. The sintering and annealing procedures are proprietary to Magnequench. After heat treatment, the magnet pieces were cut, ground, and polished for measurement of their magnetic properties. Powder composition and heat treatment were not investigated because that is beyond the scope of this study.

VI. Fill-Density Study

More than 250 NdFeB cylindrical compacts have been pressed in the ANL test facility using production-grade magnet powder obtained from Magnequench. Subsequently, many batches of the anisotropic compacts, with their grain orientation mechanically locked in place, were returned to Magnequench. As part of normal production runs, the compacts were sintered and annealed, and the PM faces were ground flat and parallel, before their demagnetization curves and/or residual flux densities were measured using hysteresisgraphs and Helmholtz coils. The first PMs had properties that were far from optimal. Thus, in cooperation with Magnequench, a significant effort was made to optimize pressing at ANL.[4, 5]

Different press loads, press rates, lubricants, and powder fill techniques were studied and changed. Before optimization, the dies were gravity-filled in a glove box and the punches were fully inserted to the fill level. The magnetic properties were most significantly improved by filling the die to powder densities less than can be achieved by gravity. However, leaving headroom in powder-filled die cavities was not a feature originally included in the design of the ANL axial-die press facility. To maintain headroom, split-ring plastic constraints were attached to each punch. The friction on each ring was calibrated to hold during insertion into an active superconducting solenoid, but they slipped when compaction loads were applied.

The results of the fill-density optimization study for cylindrical compacts with an L/D ratio ~1 are shown in Figure 5, where the maximum energy product, $(BH)_{max}$, is given for various densities. The alignment fields were applied just before and during the pressing of these compacts. By decreasing the fill density by ~20% below the gravity-fill density levels, the energy product was improved by ~20% for a 4-Tesla alignment field. The same optimal fill density was found for compacts aligned at 8 Tesla. Subsequent pressing used the same fill density.

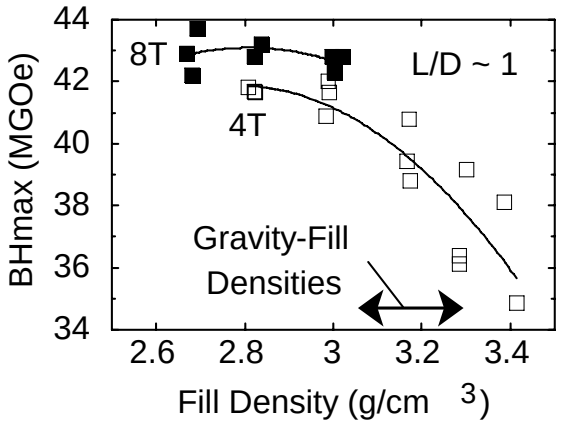

Figure 5. Maximum energy product as function of fill density.

The compacts aligned at 8 Tesla (see Figure 6) were made as part of a study to correlate energy-product improvements with increases in the alignment field, again for compacts with L/D ~1. The results are summarized in Figure 6. The maximum energy product, $(BH)_{max}$, was increased ~12% by tripling the maximum 2-Tesla alignment field available with electromagnets. The increase was the same for the first magnets made and for magnets made after the processing was optimized, but the optimized magnets had 30% higher energy products. Unexpectedly, the best magnets (solid symbols) were made when the alignment field was always on. This condition simulates the severe field gradients that loose powder in the die would experience during insertion into an operating superconducting solenoid by a reciprocating press. Most important, these maximum energy products are comparable to those of more expensive magnets made by the transverse-die-pressing technique. About 92% of the theoretical maximum was achieved. Thus what was initially considered a potential serious impediment to using superconducting solenoids (having the SCM on all the time) should not be a problem and could actually result in a cost savings.

The most effective use of the high alignment fields that can be provided by superconducting solenoids is in making near-final-shape magnets. Their finite and usually short length in the direction of magnetization

makes alignment of the powder grains especially difficult. When subjected to a uniform alignment field, the powder in the die cavity develops a highly non-uniform self-field. Because grains align along the total field lines, unidirectional alignment can be achieved only by increasing the strength of the applied alignment field until the effects of the self-field become negligible. Since the self-field distortion becomes greater for shorter magnets, there will always be short magnets that the 2-Tesla industrial electromagnets cannot adequately align. Clearly, the higher fields produced by a superconducting solenoid can provide the necessary alignment.

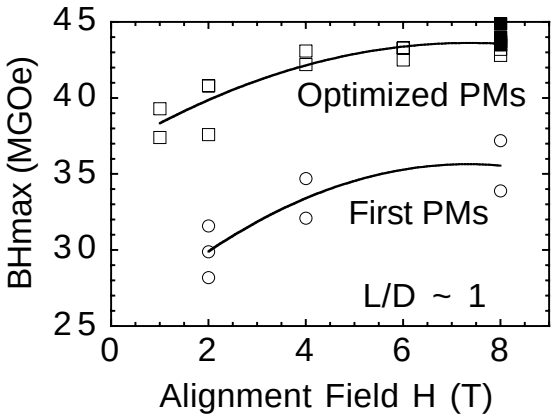

Figure 6. Maximum energy product as function of alignment field for L/D ratio ~1.

VII. Effect of Alignment Field on the Magnetic Properties of PMs

Previously, the properties of PMs with an L/D ~1 were improved significantly compared with those of industrial PMs made by axial-die pressing and were comparable to the properties of more expensive PMs obtained by transverse-die pressing. About 96% of the practical limit on remnance, B_r = 1.44 T, was achieved. Also, a preliminary study of NFS cylindrical PMs indicated that the relative improvements in B_r were greater for L/D <1, as H was increased from 2 to 8 Tesla. In particular, the B_r of the shortest PMs showed the greatest improvement, although a smaller B_r was achieved.

A study of near-final-shape cylindrical magnets was performed for compacts with L/D = 0.25, 0.50, and 0.73. The results are given in Figure 7. The remnant magnetization B_r of the shortest magnets, with a compact L/D = 0.25, improved the most. Quadrupling the alignment field from 2 Tesla increased B_r by 8%. This is equivalent to a 16% increase in the maximum energy product, since $(BH)_{max}$ is proportional to (B_r). The magnets made from compacts thicker than L/D > 0.5 did not appear to suffer self-field effects. Length-to-diameter ratios smaller than those tested are common for near-final-shape magnets, but such magnets could not be accurately made and measured with the small-diameter die (5/8-in.) available. Even larger improvements in energy product are expected for L/D < 0.25.

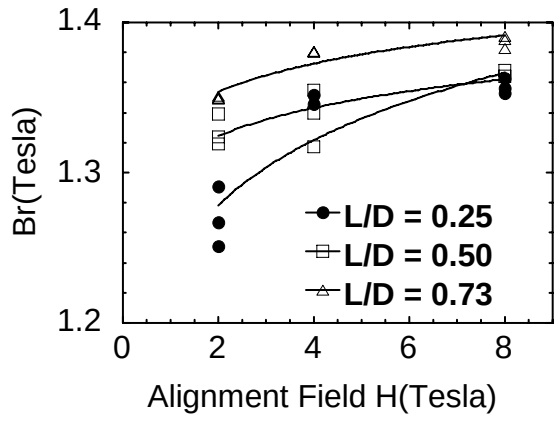

Figure 7. Remnant magnetization as a function of alignment field for L/D = 0.25, 0.50, and 0.73.

To confirm and quantify the improvements, 69 compacts, with L/D = 0.52, 0.40, or 0.27, were pressed in alignment fields of H(T) = 1, 2, 4, or 8 T.[3] Smaller L/D compacts were desirable, but they became too thin to handle. The difficulties encountered in making smaller PMs are apparent in the scatter of the B_r data shown in Figure 8. However, the data for L/D = 0.27 and 0.52 confirm the improvement trend. The B_r of the shortest PMs improved the most. Quadrupling H from 2 Tesla increased B_r by greater than 8%. This is equivalent to a 16% increase in $(BH)_{max}$, which is ~ B_r^2.

In summary, it was demonstrated that significant improvement of the energy product on the order of 12–15% can be achieved by using the stronger alignment field produced by the SCM. Near-final-shape PMs with L/D ratios of down to 0.25 were made successfully. The largest improvements in energy product were achieved with the smallest L/D ratio because the self-field (demagnetization) effect due to the geometry of the thin cylindrical disk was largely overcome by the strong alignment fields. However, as the cylindrical-shaped

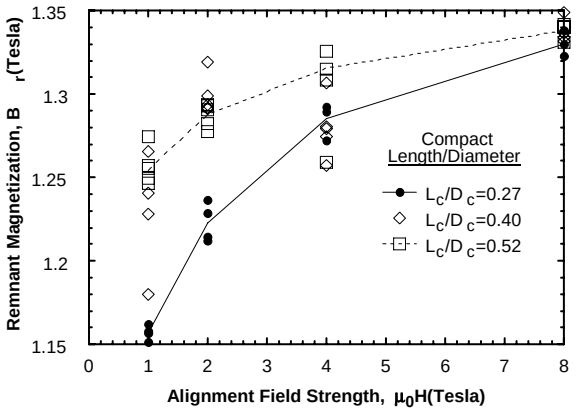

Figure 8. Remnant magnetization of short magnets.

PM became thinner as the L/D ratio was decreased, it became more difficult to handle. The compacts cracked more frequently and the rate of failure increased.

VIII. Economic Study

The objective of the economic analysis is to compare the estimated cost of the superconducting system with that of a conventional electromagnet system. Subsequently a subcontract was issued to Data Decisions to conduct the economic analysis. The key staff member of Data Decisions, Robert Wolf, has been associated with the PM industry for more than 30 years. A final report on the economic study[6] was issued in December of 2005. Following is a summary of the results of the economic study.

To estimate the capital costs of the superconducting press system, a workable system must be designed first. After several iterations, it was decided to adopt a horizontal axial press system, as shown in Figure 9. The system includes a semi-automated, four-position, dual-ended, horizontal press. The SCM has a horizontal room-temperature bore, and the alignment magnetic field is in the axial (horizontal) direction.

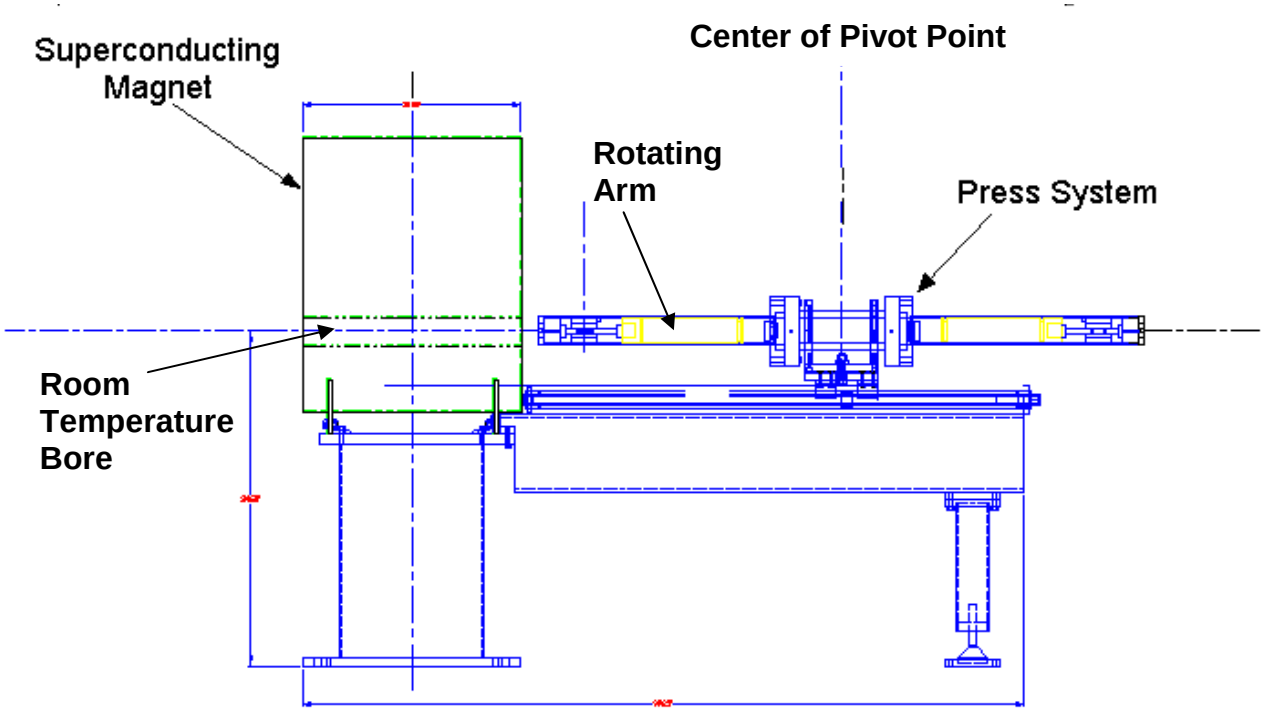

Figure 9. Schematic diagram of the proposed superconducting axial press system.

The press system needs a double-acting ram to compact the pellet. This cylinder will have to be manufactured from stainless steel, as will the balance of the system. The hydraulics can be located far enough away to avoid interaction with the magnetic field for all components except perhaps the control valves. The

four positions are located 90° apart and provide pressing, compact ejection, cleaning, and die filling, respectively.

The SCM is an actively shielded, 9-Tesla, liquid-helium-cooled superconducting solenoid with a 3-in. room-temperature bore. The vendor has determined that a liquid-cryogen-free system would be too risky for this application because eddy-current heating produced by moving the magnetic material in and out of the bore is very difficult to handle using a cryo-cooler. The superconducting manufacturer feels confident that the material can be moved out of the high field region in approximately 10 s by using a liquid-helium-cooled solenoid. Because of the high field (up to 9 Tesla) that can be generated by the SCM, magnetic shielding is required to protect nearby workers. The design of the SCM includes an active-shielding mechanism (by canceling the magnetic field around the magnet). The active shielding is very effective, and the stray field is <10 gauss in any direction measured 1 m from magnetic center. Detailed specifications for the 9-Tesla SCM are provided in the report on the economic study.[6] The 9-Tesla SCM quoted by the vendor is very similar to the one currently being used at ANL to make compacts (Figure 4). Therefore, the design is highly credible.

Quotations were received from vendors for the estimated cost of the SCM and the semi-automated press system. This cost estimate is included in Table 1, which shows a comparison of the estimated capital costs of various production systems. In Table 1, the estimated capital cost of the ANL superconducting system is for an axial press system. Therefore, it should be compared with the axial press system currently used in industry. This comparison shows that the capital costs for the ANL processing are comparable to current industry costs.

Table 1. Capital cost ($) of various production systems

	Current industry			**ANL axial superconducting press system**	
	Axial	**Transverse**	**Isostatic**	**(8 magnet/ minute)**	**(16 magnet/ minute)**
Alloy	6.8–8.0/lb	6.8–8.0/lb	6.8–8.0/lb	6.8–8.0/lb	6.8–8.0/lb
Hydrider	380,000	380,000	380,000	380,000	380,000
Jet Mill	255,000	255,000	255,000	255,000	255,000
Press	300,000	300,000	500,000	150,000	250,000
Alignment Coil	20,000	20,000	20,000	150,000	150,000
Rectifier	55,000	55,000	55,000	0	0
Sintering	440,000	440,000	440,000	440,000	440,000
Grinder	54,500	54,500	54,500	54,500	54,500
Slicer TS 23	0	175,000	175,000	0	0
Total	1,504,500	1,679,500	1,879,500	1,429,500	1,529,500

A comparison of estimated operating costs is also provided in the economic report.[6] For the conventional system, the major cost is the electricity required to charge the electromagnet. For the superconducting system, the major cost is the liquid helium required to run the SCM. The estimated operating cost for the superconducting system is significantly lower than that for the conventional electromagnet system ($3.1/hour versus $8.0/hour). However, the estimated annual operating cost is only a small fraction (1%) of the estimated capital cost.

Table 2 shows the comparison of the price per piece among the Vacuumschmelze, the Tridus, and the estimated ANL superconducting production system. For a near-final-shape magnet (0.45 × 0.45 × 0.4 in.), the estimated price per piece of the ANL process is about 13% lower than that of the magnet supplied by Tridus. This is mainly because grinding and/or slicing are not required for the superconducting production system.

Table 2. Summary of price/piece ($) comparison

Size	1 × 1 × 0.5	0.45 × 0.45 × 0.4
Vacuumschmelze	4.77	1.27
Tridus	3.17	0.75
ANL	3.99	0.65

IX. Summary and Conclusions

In summary, it was demonstrated that significant improvement of the energy product on the order of 12–15% can be achieved by using the stronger alignment field produced by the SCM. Near-final-shape PMs with L/D ratios of down to 0.25 were made successfully. Largest improvements in energy product were achieved with the smallest L/D ratio because the self-field (demagnetization) effect due to the geometry of the thin cylindrical disk was largely overcome by the strong alignment fields.

The current status of production for NdFeB PMs and the magnet industry in the United States are surveyed and reviewed. As a result of recent mergers and acquisitions, all production of licensed NdFeB magnets in the United States has ceased and the magnets now are mainly imported from China, Japan, and Europe. The market for NdFeB PMs has grown considerably since its inception. There are many applications of NdFeB magnets in automobiles, such as actuator,, motors, pumps, loudspeakers, and sensors. An HEV employs NdFeB PMs in its electric motor. Designers are looking for motors with low weight, high efficiency, and high output.

The specific objective of the economic study is to compare the estimated costs of a superconducting manufacturing system developed at ANL with that of a conventional system using electromagnets. The major conclusions reached are (1) the capital and operating costs of the superconducting system are not significantly different from those of a conventional electromagnet system, and (2) the price per piece of the superconducting system appears to be 10 to 15% below that of the conventional system for near-final-shape magnets because the former does not require extensive grinding and/or slicing after sintering.

Overall, the superconducting manufacturing system would

- Produce NeFeB magnets with higher energy, +15%, at a lower cost, –10% to –15%, than present technology. Even if there were no cost savings the increase in energy would make the technique worthwhile.
- Present the automotive industry with higher-performance, reduced-weight magnets, which
  - — reduce vehicle weight
  - — increase vehicle mileage
  - — can be used in other applications besides traction motors
  - — can be achieved without increasing the current cost of the magnets
- Provide similar benefits to other U.S. industries.
- Encourage the use of this technique at a U.S. producer.

References

1. R. M. Bozorth, *Ferromagnetism*, IEEE Press, The Institute of Electrical and Electronics Engineers, Inc., New York, 1978. Chapter 9: Materials for Permanent Magnets.

2. H. Nagata and M. Sagawa, “Toward an Ideal Process for the NdFeB Sintered Magnets,” pp. 354–359 in *Proceedings of the Seventh International Workshop on Rare Earth Magnets and Their Applications*, G. C. Hadjipanayis and M. J. Bonder, eds., Newark, Delaware, August 19–22, 2002.

3. T. M. Mulcahy, J. R. Hull, E. Rozendaal, J. H. Wise, and L. R. Turner, “Improving Sintered NdFeB Permanent Magnets by Powder Compaction in a 9 T superconducting Solenoid,” *Journal of Applied Physics*, **93**(10), 8680–8682, 2003.

4. T. M. Mulcahy, J. R. Hull, E. Rozendaal, and J. H. Wise, “NdFeB Magnets Aligned in a 9-T Superconducting Solenoid,” pp. 600–607 in *Proceedings of the Seventh International Workshop on Rare Earth Magnets and Their Applications*, Newark, Delaware, August 18–22, 2002.

5. T. M. Mulcahy and J. R. Hull, “A Superconducting Solenoid and Press for Permanent Magnet Fabrication,” *IEEE Trans. on Applied Superconductivity*, **13**(2), 1668–1671 (June 2003).

6. R. Wolf, *An Economic Study Of The Manufacture of High Energy Permanent Magnets For Traction Motors In Hybrid Electric Vehicles*, prepared by Data Decisions (1069A Mill Pond Road, Valparaiso, Indiana 46385) for Argonne National Laboratory, issued by the Thermal and Electromechanics Section, Energy Technology Division, Argonne National Laboratory, December, 2005.

Appendix B

Diesel Particulate Filter Development Project

Final Report

ORNL/Sub/4000000723

DIESEL PARTICULATE FILTER DEVELOPMENT PROJECT

MICROWAVE-REGENERATED HEATING PERFORMANCE and ROUND PLEATED FILTER CARTRIDGE DEVELOPMENT

FINAL REPORT

FY 1999–2005 Program

February 10, 2006

Prepared by

Richard D. Nixdorf
Industrial Ceramic Solutions, LLC
1010 Commerce Park Drive, Suite I
Oak Ridge, Tennessee 37830

Telephone: (865) 482-7552
FAX: (865) 482-7505
e-mail: nixdorfr@indcermicsolns.com

Prepared under
Subcontract No. 4000000723
for
Oak Ridge National Laboratory
Oak Ridge, Tennessee 37831
Managed By
UT- Battelle, LLC

CONTENTS

Abstract

The U.S. Department of Energy's (DOE's) Partnership for a New Generation of Vehicles and FreedomCAR Programs both supported new technology to control particulate emissions from diesel engine exhaust. Industrial Ceramic Solutions, LLC (ICS) invented a low thermal-mass ceramic fiber filter capable of reducing particulate matter by more than 95% at low backpressure. An optional microwave device capable of cleaning the filter cartridge during diesel vehicle operation was also developed. This report recounts the development activities, their results and conclusions, and work that occurred between FYs 1999 and 2005. The work is divided into two sections, based upon the two distinct foci of the funded objectives. The first section addresses the development of a microwave-sensitive ceramic fiber filter medium and a microwave system capable of cleaning the diesel soot from the filter. Data are presented to show the performance of the filter and the adjoining microwave-cleaning system. These data include filtration efficiency in the diesel exhaust and microwave-cleaning efficiency for a soot-laden filter. After the FY 2003 funding, DOE and its diesel engine industrial partners elected to move away from the microwave system project in order to concentrate specifically on developing a round pleated filter cartridge that would be suitable for any type of regeneration system. The development process for the round pleated filter is discussed in the second section. The ceramic fiber filter medium for the pleated filter was improved to provide better customer performance on a diesel engine by increasing the filter strength and the diesel soot loading capacity. This advancement also reduced the size of the round pleated filter package. The design and fabrication of a round pleated filter suitable for a 7.3-L Ford diesel pickup is discussed.

1. Introduction

DOE's Partnership for the New Generation Vehicle Program (PNGV) and its member automobile manufacturers established an initiative to develop a small diesel engine to improve fuel efficiency compared with large gasoline-powered vehicles. This diesel engine technology implementation would also reduce greenhouse gas emissions to the atmosphere. Public concern over particulate emissions from diesel engine exhaust currently impedes efforts to replace gasoline engines with small diesels. A positive control technology for diesel particulate pollution would free the diesel engine industry and auto and truck manufacturers to expand the use of fuel-efficient diesel engines in small trucks and passenger vehicles. To facilitate that change, Industrial Ceramic Solutions, LLC (ICS) invented a low-mass ceramic fiber filter capable of greater than 95% particulate matter (PM) reduction at low backpressure. An optional microwave device capable of cleaning the filter cartridge during diesel vehicle operation was also developed. The patented silicon carbide (SiC) fiber component makes efficient microwave heating of the filter cartridge possible.

This filter concept was presented to the PNGV committee consisting of representatives from DOE, the Environmental Protection Agency, Chrysler, Ford, and General Motors in early 1999. The initial concern of the automobile manufacturer members was the microwave filter system's ability to achieve carbon combustion temperatures at any level of engine exhaust flow through the filter. A firm requirement for exhaust control is that it be a simple system that does not require moving parts in the exhaust piping, such as valves, dampers, or multiple filter rotation. Past experience in the auto industry has shown that life-cycle failure is almost certain when mechanically moving parts are in an exhaust stream. The PNGV members requested a testing program to investigate the ability of the microwave-regenerated ceramic filter to reach carbon ignition temperatures (> 550°C) without a catalyst under dynamic exhaust flow conditions.

After an early bench-top experiment conducted in FY 1999 proved that the microwave-regeneration system was capable of reaching carbon combustion temperatures, Ford volunteered a test cell at its Dearborn, MI, Scientific Research Laboratory for an engine test. The microwave-regenerated ceramic filter was tested on the experimental Ford DIATA 1.2-L diesel engine. Mechanical durability, filtration efficiency, and microwave regeneration efficiency were investigated. The experimental results from this test showed that the filter could remove diesel particulate with 80–90% efficiency in operating conditions ranging from idle to

cruising speed. The ceramic cartridge, regenerated by microwave energy at engine idle speed, was cleaned in place to its original filter condition. The test cell results showed that the pressure drop across the ceramic paper filter cartridge was significantly less than that experienced by existing extruded cordierite wall-flow filters.

Engine and Vehicle Testing

In FY 2001, a second stationary engine test was conducted on a Volkswagen 1.9-L turbo direct injection (TDI) engine at Oak Ridge National Laboratory (ORNL), using microwave energy to clean a ceramic fiber corrugated wall-flow filter. A filter efficiency of greater than 95% was demonstrated. Prior to this Volkswagen engine test, the strength of the filter medium was increased from 1 to 6 $lb/in.^2$ burst strength using improved ceramic processing. In addition, finite element modeling of the microwave field was applied to improve the uniformity of the microwave cartridge heating.

In the first vehicle test., the filter cartridge (without a microwave unit) was mounted on a Ford F250 7.3-L diesel pickup truck for approximately 6,000 miles and nine months of road testing. Filter cleaning was accomplished off-line in a laboratory furnace. This Ford truck was used as the test vehicle for diesel particulate filter (DPF) prototypes through the end of the program.

The next vehicle test was to be conducted using a 1998 Volkswagen Jetta with a 1.9-L TDI engine. A filter and a microwave regeneration system were installed on the Volkswagen and tested for 200 miles and six microwave regenerations; however, the test was cancelled owing to irreparable damage to the exhaust gas recirculation (EGR) system that occurred before ICS received the vehicle. Also in FY 2002, the first pleated ceramic fiber filter was fabricated and tested on the Ford truck. This pleated filter design exhibited a tenth of the backpressure experienced with a standard wall-flow honeycomb DPF. The pleated filter was then tested for particulate removal efficiency at ORNL on a 1.7-L Mercedes engine in FY 2003. The efficiency was measured at greater than 96%. A microwave-regeneration system was designed and fabricated to test a pleated, rectangular filter cartridge on the 7.3-L Ford truck. This system was road-tested through a full range of engine operating conditions with limited success in achieving full regeneration as a result of non-uniformity of the microwave heating.

Round Pleated Filter Cartridge

The pleated ceramic fiber diesel particulate cartridge used before FY 2004 was rectangular in shape, but most automotive applications required a round shape. All FY 2004 and FY 2005 work was directed toward designing, developing, and fabricating a round pleated filter. The microwave regeneration work was put on hold, and a filter was designed to accommodate the exhaust of the Ford 7.3-L diesel truck. A ceramic injection molding process was investigated to apply a frame to the fiber filter medium. Furthermore, mechanical stress loading and size constraints required some improvements in the ICS ceramic fiber medium. The burst strength of the medium was increased from approximately 150 to 415 in. of water, and the soot-holding capacity was increased from 0.86 to 1.4 $grams/ft^2$. With these improvements, a joint development agreement was entered between ICS and a major Tier I automotive parts supplier with the objective of taking the pleated ceramic fiber filter cartridge into the commercial marketplace.

The backpressure and soot-holding capacity of a fiber filter has advantages over the ceramic wall-flow filter, as seen in Figure 1. Particles are trapped by “depth filtration” rather than the mechanical membrane filtration of the wall-flow filter. Depth filtration allows the pore size of the fiber filter to be many times greater than the diameter of the particles being removed. Particles are trapped by adhering to the individual fibers, rather than being stopped by very fine holes in the ceramic wall. The net result is filtration efficiency equivalent to the ceramic wall-flow filter with approximately one-fifth of the backpressure increase. Another advantage is the ability of the fiber filter to trap any size of particle down to less than 10 nanometers in diameter.

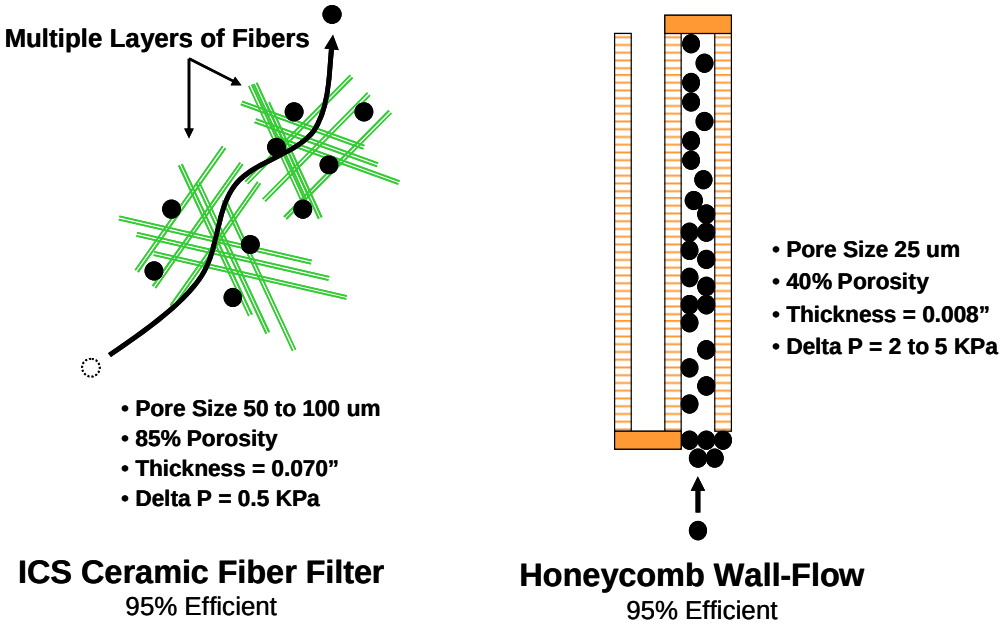

Figure 1. Fiber filter compared with wall-flow filter.

2. FY 1999 Experimental Procedure and Results

Microwave regeneration of the ICS fiber filter is potentially the most efficient method to remove the soot from a loaded DPF. The patented ICS SiC fiber demonstrates unique properties in a microwave field. The fiber is neither reflective nor transparent to microwaves. Rather, the microwaves are absorbed by the fibers and converted to thermal energy that quickly raises the temperature of the filter cartridge. Typically, only 3 minutes is required to microwave-heat the cartridge to above 600°C. This is particularly advantageous when a catalyst-coated filter is used. With normal heating methods, efficiency is lost as heat is transferred from a source to the exhaust gas, the filter cartridge, and finally the catalyst. The microwave heating of the SiC fibers provides a shortcut. The microwaves directly heat the fibers on which the catalyst particles are located, significantly improving heating efficiency.

For the initial benchtop proof-of-concept tests conducted in 1999, a 2-in.-diam SiC filter cartridge was wrapped with a 0.5-inch-thick, high-temperature, fiber-wool insulation material. The 3-in.-diam cartridge/insulation package was inserted in the 2-in.-thick rigid oxide fiber insulation cylinder in a microwave cavity. This created a 3-in. insulation wall between the SiC fiber cartridge and the steel microwave cavity wall.

Each cartridge test was run with airflows through the cartridge of 5, 8.5, 10, and 15 ft^3/min. The microwave power inputs tested at each airflow setting were 500, 800 and 1,000 W. During each experimental run, room temperature–compressed air flow was brought to equilibrium through the filter cartridge at the designated flow rate. Microwave power at the designated setting was initiated. Temperature readings on the filter cartridge were recorded at 5, 10, 15, 20, 30, 40, 50, 60, 75, 90, and 120 seconds. The temperature of the filter cartridge was measured by a Mikron M90 series portable infrared thermometer. The hot filter, as viewed through the pyrometer, is shown in Figure 2; the microwave oven is shown in Figure 3.

Heat from the microwave field coupling to the SiC fibers increases the temperature of the filter until the heat produced in the fibers equals the heat removed from the filter medium by the exhaust stream, plus the stored heat. The equilibrium zone is reached when the heat exchanger values stop increasing or begin to level. It is assumed that the filter temperature will stop increasing near the end of this equilibrium zone. This is verified by observing the actual filter cartridge temperature performance readings shown in the graph in Figure 4.

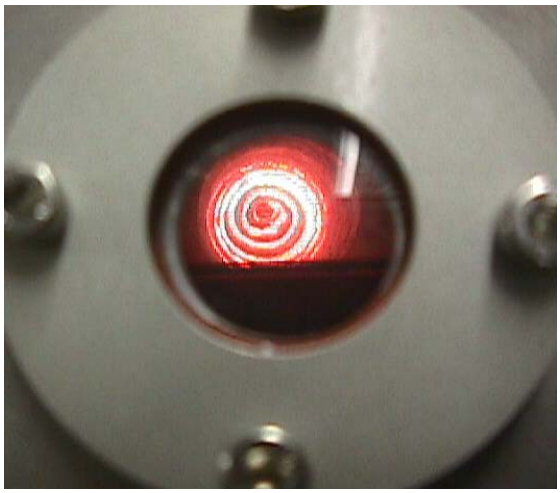

Figure 2. Microwave-heated cartridge at 15 cfm air flow

Figure 3. Microwave oven

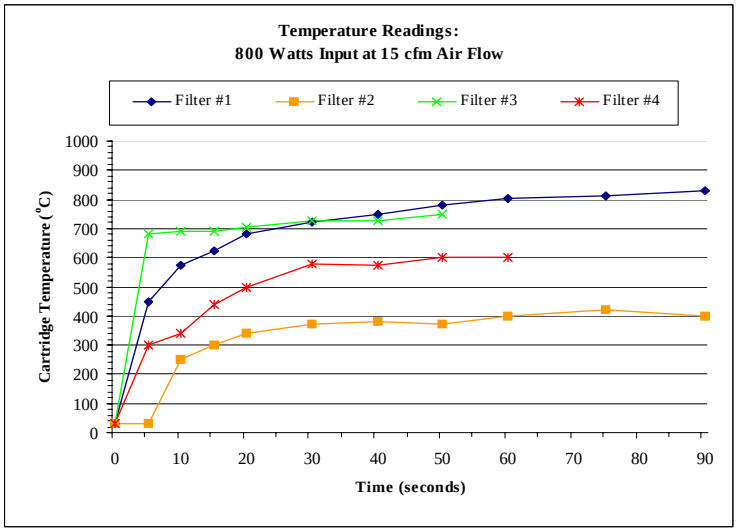

Figure 4. Microwave heating rate of filter cartridge

Three different SiC fiber content levels in filters reached the goal of greater than 550°C in less than 30 seconds at 800 W of microwave input and 15 ft^3/min exhaust flow. It is therefore possible for the ICS filter to trap soot at a high efficiency and to be regenerated by microwave energy at some exhaust flow condition (idle).

3. FY 2000 Experimental Procedure and Results

The first engine testing of the ceramic fiber filter was conducted on a 1.2-L DIATA diesel engine at the Ford Scientific Research Laboratory. The filters and test setup are shown in Figure 5 after the filters were loaded with soot at levels ranging from 0.5 to 2.5 KPa. Figure 6 shows the filter can/microwave applicator installed in the DIATA engine exhaust system.

The microwave filter system was installed in the DIATA engine exhaust approximately 3 m from the exhaust manifold, as shown in Figure 6. The microwave power supply was connected to the filter by 3 m of

Exhaust exit **Exhaust entry**

Figure 5. ICS fiber filter cartridges in can.

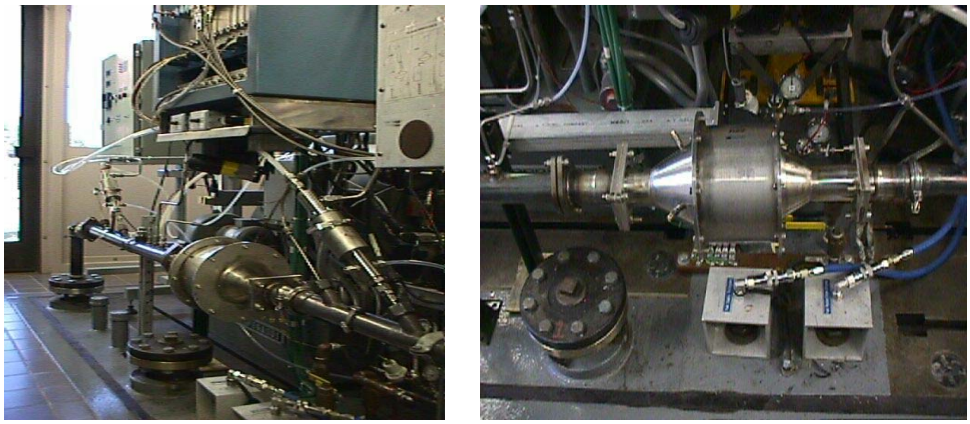

Figure 6. Microwave filter system installed in DIATA test cell.

rectangular aluminum waveguide tubing. The engine was operated at several steady-state speeds to load the filter. A typical regeneration event is shown in Figure 7.

The filtration efficiency for diesel particulate removal was 86%, and the microwave cleaning returned the filter cartridge to within 97% of its fresh filter condition.

4. FY 2001 and 2002 Experimental Procedure and Results

The microwave filter technology is unique because of the discovery and use of a special SiC fiber that efficiently converts microwave energy to heat energy. These fibers can achieve the unusually high temperature of 1200°C in 9 seconds in a standard household microwave oven. The resolution of several diesel vehicle exhaust problems was anticipated through the application of this phenomenon.

Two vehicles were selected for on-road testing of the microwave filter system. Instrumentation was designed, fabricated, and tested to continuously monitor the backpressure resulting from carbon particulate accumulation on the filter, the exhaust flow, and the temperature of the exhaust during vehicle operation. The instrumented exhaust filter systems were installed on a Ford F-250 7.3-L diesel pickup (Figure 8) and a Volkswagen Jetta 1.9-L diesel car provided by DOE (Figure 9). The Ford truck was tested under routine highway driving conditions for approximately 6,000 miles. The filter was removed and microwave-regenerated in the laboratory to show the effects of microwave heating on the particulate-loaded cartridge. The Volkswagen Jetta was equipped with an on-board microwave regeneration system. This vehicle was to be driven for 7,000 miles under controlled test track conditions by the Transportation Research Center near Columbus, OH; however, the testing was cancelled after only 200 miles because of an irreparably damaged EGR system that could not be controlled. This damage was found during testing and was determined to have been present before delivery of the vehicle to ICS.

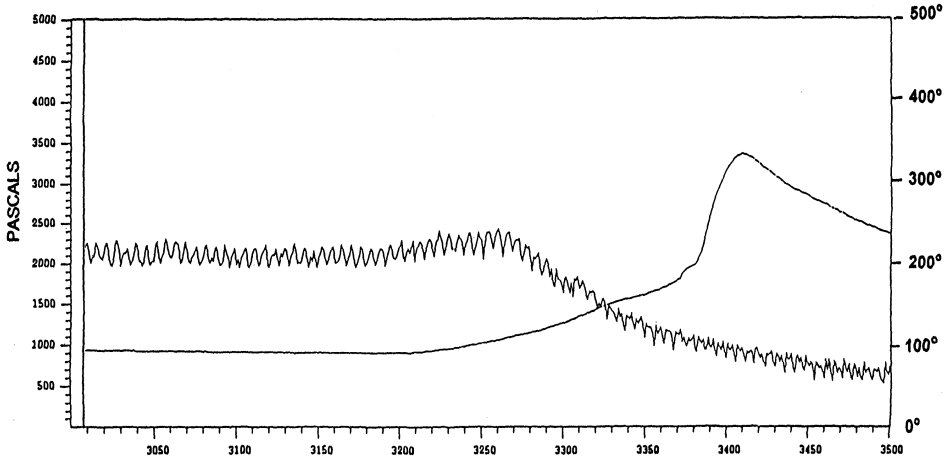

Figure 7. Regeneration at 1,000-RPM high-idle speed after 1 hour of operation at 2600 RPM.

Figure 8. Ford 7.3-L test truck.

Figure 9. Volkswagen 1.9-L microwave-cleaned DPF vehicle.

The Volkswagen DPF system was moved to a stationary test cell at ORNL, where it recorded more than 97% particulate removal efficiency over a spectrum of steady-state operating conditions. The ICS filter on the 7.3-L truck was subjected to the full engine load of exhaust rate of 1,000 ft^3/min without any apparent damage.

5. FY 2003 Experimental Procedure and Results

The development of a pleated ceramic fiber filter cartridge occurred early in FY 2003. Many experiments were conducted to determine the optimum geometry of the filter and the best means to fabricate this geometry in the laboratory. A pleating process, using an ICS proprietary ceramic binder, was developed. A number of structural designs to enclose and support the pleated fiber medium in the exhaust were investigated; the finished product is shown in Figure 10. Because the pleated cartridge was a significant change from the wall-flow design that had been used over the previous several years, verification of the PM removal efficiency was needed. Pleated filter cartridges were canned and tested by ORNL on a 1.7-L Mercedes stationary test cell.

Figure 10. ICS rectangular pleated ceramic fiber filter.

The particulate removal efficiency from those tests measured 98% for carbon mass and 96% for nanoparticulate soot in a particle size distribution measurement.

A microwave-regenerated DPF system was designed and fabricated for the Ford F-250 7.3-L diesel truck. The system was installed on the truck bed as shown in Figure 11. This arrangement accommodated placement of the temperature and pressure sensors and facilitated disassembly of the can during periodic filter cartridge examinations. All microwave equipment, system controls, monitoring sensors, and computer data acquisition equipment were installed on the truck for the road and track testing. As testing began, a noticeable deficiency in microwave heating of the cartridges was observed. Further investigation revealed a need to reduce the thermal mass of the filter cartridges, to include more insulation around the filter can, and to improve the microwave field concentration on the filters. The microwave DPF system was then put on hold to concentrate on the development of the pleated filter cartridge.

Figure 11. Microwave-regenerated DPF system installed in the Ford 7.3-L diesel truck.

6. FY 2004 and 2005 Experimental Procedures and Results

In experiments conducted by ICS and others under the FY 2003 program, much less exhaust backpressure was experienced by the diesel engine with the pleated ceramic fiber DPF. This backpressure reduction will improve engine performance and reduce the fuel penalty imposed by the PM control device. The pleated ceramic fiber DPF, which weighs significantly less than the extruded wall-flow filter, exhibits a lower thermal mass to achieve faster soot combustion temperatures and adds less weight to the vehicle.

The transition from the flat pleated filter to the round pleated filter cartridge was necessary because of the demands of automotive exhaust system manufacturers for a round DPF shape to fit their established canning processes. ICS designed a round pleated filter cartridge based upon the diesel engine testing data from the rectangular pleated filter cartridge. Extensive road testing on the Ford F250 diesel truck had shown that the 8 ft^2 of medium in the rectangular pleated filters is approximately 20% less than that required for optimum filter operation. ICS approached the project with an initial round pleated filter that was approximately 7 in. in diameter and 12 in. long. This configuration yielded the 10 ft^2 of effective filter medium surface area to accommodate a full spectrum of diesel exhaust flow rates on the 7.3-L test truck. ICS employed a mechanical engineer to design a computer modeling program that could determine the optimum pleat geometry and cartridge size needed to accommodate the Ford truck's exhaust flow. ICS worked with an experienced ceramic injection molding company to develop structural support for the pleated filter media. The efforts of the filter cartridge design engineer and the injection-molding company were coordinated to produce a robust round filter cartridge structure suitable for the first round diesel exhaust prototype test cartridge, as shown in Figure 12.

ICS fabricated a can assembly for testing the pleated filters on the Ford F250 truck. The exhaust is directed through the bed of the truck to facilitate installation and removal of filter cartridges for evaluation (Figure 13). ICS can test both round and flat pleated filters in this test device. It has been valuable in investigating the durability of support structures and the soot loading capacity of the pleated filter cartridges.

FY 2005 funding was used to design and fabricate a full-scale prototype test filter for the Ford truck, as shown in Figure 14. Significant work was done on materials improvements to allow the fabrication and testing of this larger round pleated filter. Experiments were conducted in the ICS laboratory with a number of commercial binders and commercially available ceramic fibers, and the binder-fiber mix was subsequently optimized to improve filter durability. The improved mix was then used in commercial papermaking equipment to produce continuous rolls of filter medium that would be pleated and incorporated into test cartridges.

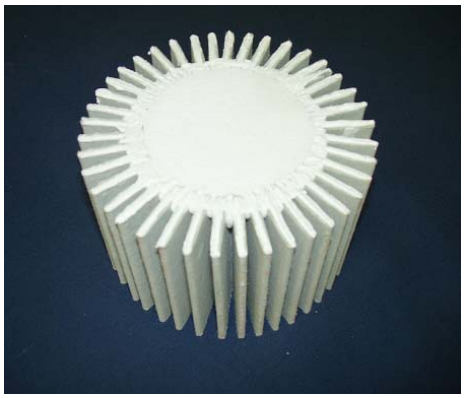

Figure 12. First fabricated round pleated prototype.

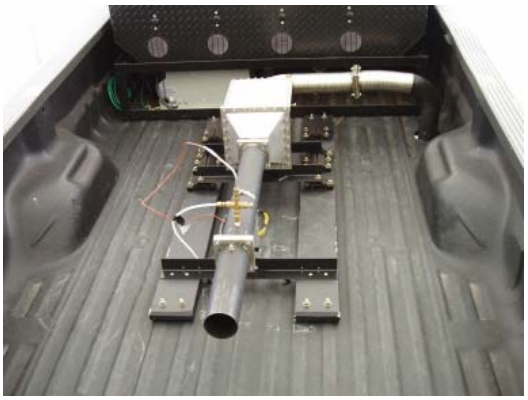

Figure 13. Round pleated filter test setup for 7.3-L truck.

The filter media burst strength was improved from 185 in. of water at the end of 2004 to 415 in. of water in 2005. Burst strength improvements over the life of the program are shown in Figure 15. The soot-loading capacity was increased from the 0.86 grams/ft^2 recorded in 2004 to 1.4 grams/ ft^2 in 2005. The improved filter medium, converted to continuous paper and then to filter cartridges, was road-tested on the Ford 7.3-L truck. Twenty road tests on a pair of rectangular pleated filters were completed, loading the filter to over 80 in. of water backpressure during each test. The filter was regenerated at 700°C after each road test, and there was no damage to the filter cartridge during the testing or the regeneration procedures.

7. Final Program Conclusions

In 1999, this program began with the concept of using a special SiC fiber that was very efficient at converting microwave energy to thermal energy as a new type of diesel exhaust particulate filter. The ceramic fiber filter cartridge, regenerated by microwave energy, was a unique invention in a field dominated by extruded ceramic honeycomb wall-flow DPFs. This new concept was foreign to the automotive industry and was only able to proceed through the support of DOE as a new and unique technology.

Commercialized products are often quite different from the original concepts or discoveries that inspired their development. In this case, the microwave regeneration of a DPF led to the invention of a novel pleated ceramic fiber DPF cartridge that can be regenerated by all commercial methods. Continued DOE support of the cartridge development, even after the microwave-regeneration system became marginal, allowed ICS to make significant improvements in the filter cartridge design, materials, and manufacturing process.

Figure 14. Full-scale 6-in.-diam × 12-in-long long round pleated filter ready for canning and truck testing (first prototype shown at bottom of figure).

The pleated ceramic fiber filter cartridge demonstrates lower backpressure and thermal mass than those of conventional wall-flow DPFs. These two advantages make it a viable option for all types of diesel PM control systems. ICS is currently working with a major international filter manufacturer to license the use of the technology and to supply the large volume of filter cartridges required to supply the worldwide diesel industry. ICS is also collaborating with several vehicle manufacturers to develop improved commercial exhaust control systems for the 2010 market. The gasoline engine catalytic converter was introduced in 1975; however, it did not reach a stage of optimum efficiency until 2005. The

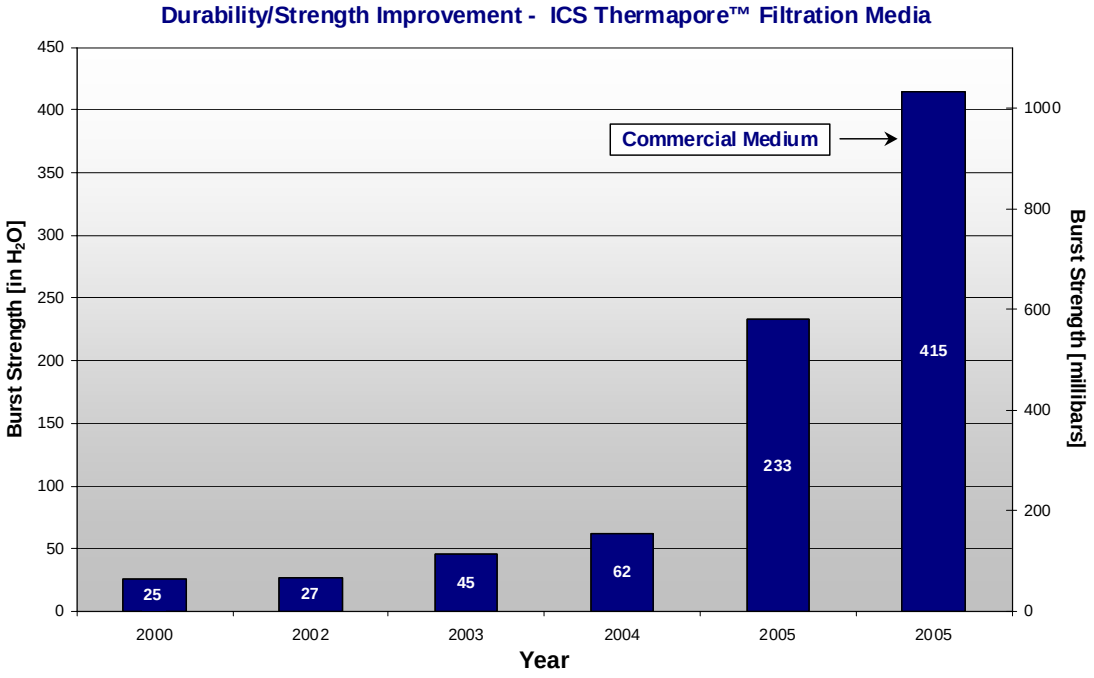

Figure 15. Program progress for improving filter media strength and durability.

current diesel engine DPF control systems will be installed on diesel vehicles in 2007. Since these systems do not yet have a proven operating record or customer acceptance in volume vehicle applications, there are still opportunities for new technologies, such as the ICS pleated filter cartridge, to be introduced into the commercial marketplace. Advantages offered by the ICS DPF technology will contribute to the optimization of existing and future diesel emission control systems.

8. Future Work

A pilot production line is being assembled for semi-continuous volume production of ICS round pleated filter cartridges. Many diesel-industry companies are interested in product testing for 2010 exhaust system applications, and ICS has a number of programs in progress to further improve the performance characteristics of the filter cartridge. Customer prototypes will be available in 2006.

The microwave-regeneration concept, which DOE ceased to fund in FY 2003, is still of interest to a number of automotive and off-road diesel engine customers. ICS has joined with a major microwave systems company to advance this technology. Microwave-regeneration is ideal for use in diesel hybrids, and DOE should again consider funding related projects if interest in the production of diesel hybrids in the United States grows.

Publications

J. Green, R. Nixdorf, J. Story, and R. Wagner, “Microwave-Regenerated Diesel Exhaust Particulate Filter,” SAE Paper 2001-01-0903, Society of Automotive Engineers, Warrendale, Pennsylvania, 2001.

R. Nixdorf, “Microwave-Regenerated Diesel Particulate Filter,”presented at the Society of Automotive Engineers World Congress, Detroit, March 5–8, 2001.

R. Nixdorf, “Microwave-Cleaned Ceramic Filter Using Silicon Carbide Fibers,” presented at the American Filtration Society National Technical Conference, Tampa, florida, May 1–4, 2001.

J. Wainwright and R. Nixdorf, “Microwave-Regenerated Diesel Particulate Filter,” presented at The University of Wisconsin Exhaust Aftertreatment Symposium, Madison, Wisconsin, June 12–13, 2001.

R. Nixdorf, “In-situ Microwave Cleaning of Silicon Carbide Fiber Filtration Media,” TechTextile Symposium North America, Atlanta, April 2002.

R. Nixdorf, “Microwave-Regenerated Particulate Filter,” DOE National Laboratory Advanced Combustion Engine R&D Merit Review and Peer Evaluation, Argonne National Laboratory, May 13–15, 2003.

R. Nixdorf, “Microwave-Regenerated Particulate Filter,” American Filtration Society Diesel and Gasoline Engine Emission Solutions Conference, Ann Arbor, Michigan, October 2003.

R. Nixdorf, “Advances in Filter Media Development for Diesel Exhaust Systems, Ceramic Bonded Ceramic Fiber Pleated DPF Cartridge,” American Filtration and Separation Society Diesel and Gas Engine Emissions Solutions Conference, Ann Arbor, MI, September 2005.

Patents

Richard D. Nixdorf, “Ceramic and Fiber-Based Filter Web and Method,” U.S. Patent no. 6,913.059, July 2005.

Richard D. Nixdorf, “Filter System Employing Microwave Regeneration,” U.S. Patent no.6,855,250, February 2005.